Development of a Wide Field Diffuse Reflectance Spectral Imaging System for Breast Tumor Margin Assessment

by

Justin Ying-Sung Lo

Department of Biomedical Engineering
Duke University

Date:_____
Approved:

_____
Nimmi Ramanujam, Supervisor

_____
Nan M. Jokerst

_____
Gregory M. Palmer

_____
Kathryn R. Nightingale

_____
Robert A. Malkin

Dissertation submitted in partial fulfillment of
the requirements for the degree of
Doctor of Philosophy in the Department of
Biomedical Engineering in the Graduate School
of Duke University

2012

ABSTRACT

Development of a Wide Field Diffuse Reflectance Spectral Imaging System for

Breast Tumor Margin Assessment

by

Justin Ying-Sung Lo

Department of Biomedical Engineering
Duke University

Date:_____
Approved:

_____
Nimmi Ramanujam, Supervisor

_____
Nan M. Jokerst

_____
Gregory M. Palmer

_____
Kathryn R. Nightingale

_____
Robert A. Malkin

An abstract of a dissertation submitted in partial
fulfillment of the requirements for the degree of
Doctor of Philosophy in the Department of
Biomedical Engineering in the Graduate School of
Duke University

2012

Abstract

Breast conserving surgery (BCS) is a common treatment option for breast cancer patients. The goal of BCS is to remove the entire tumor from the breast while preserving as much normal tissue as possible for a better cosmetic outcome after surgery. Specifically, the excised specimen must have at least 2 mm of normal tissue surrounding the diseased mass. Unfortunately, a staggering 20-70% of patients undergoing BCS require repeated surgeries due to the incomplete removal of the tumor diagnosed post-operatively. Due to these high re-excision rates as well as limited post-operative histopathological sampling of the tumor specimen, there is an unmet clinical need for margin assessment. Quantitative diffuse reflectance spectral imaging has previously been explored as a promising, method for providing real-time visual maps of tissue composition to help surgeons determine breast tumor margins to ensure the complete removal of the disease during breast conserving surgery. We have leveraged the underlying sources of contrast in breast tissue, specifically total hemoglobin content, β-carotene content, and tissue scattering, and developed various fiber optics based spectral imaging systems for this clinical application. Combined with a fast inverse Monte Carlo model of reflectance, previous studies have shown that this technology may be able to decrease re-excision rates for BCS. However, these systems, which all consist of a high power broadband xenon source, fiber optics probes, an imaging spectrograph and a

CCD, have severe limitations in system footprint, tumor area coverage, and speed for acquisition and analysis. The fiber based spectral imaging systems are not scalable to smaller designs that cover a large surveillance area at a very fast speed, which ultimately makes them impractical for use in the clinical environment. The objective of this dissertation was to design, develop, test, and show clinical feasibility of a novel wide field spectral imaging system that utilizes the same scientific principles of previously developed fiber optics based imaging systems, but improves upon the technical issues, such as size, complexity, and speed,to meet the demands of the intra-operative setting.

First, our simple re-design of the system completely eliminated the need for an imaging spectrograph and CCD by replacing them with an array of custom annular photodiodes. The geometry of the photodiodes were designed with the goal of minimizing optical crosstalk, maximizing SNR, and achieving the appropriate tissue sensing depth of up to 2 mm for tumor margin assessment. To further decrease the footprint and improve the portability of the system, discrete wavelengths of light were explored to replace the broadband source. A wavelength selection method that combines an inverse Monte Carlo model and a genetic algorithm was developed in order to optimize the wavelength choices specifically for the underlying breast tissue optical contrast. With the goal of eventually implementing laser diodes and/or light emitting diodes as the source, an intermediary proof of principle system was built and consisted of a broadband source with an 8-slot filter wheel containing the optimized set

of wavelength choices, an optical light guide and quartz light delivery tube to send the 8 wavelengths of light in free space through the back apertures of each annular photodiode in the imaging array, an 8-channel integrating transimpedance amplifier circuit with a switch box and data acquisition card to collect the reflectance signal, and a laptop computer that controls all the components and analyzes the data.

This wide field spectral imaging system was tested in tissue-mimicking liquid phantoms and achieved comparable performance to previous clinically-validated fiber optics based systems in its ability to extract optical properties with high accuracy. The system was also tested in various biological samples, including a murine tumor model, porcine tissue, and human breast tissue, for the direct comparison with its fiber optics based counterparts. The photodiode based imaging system achieved comparable or better SNR, comparable extractions of optical properties extractions for all tissue types, and feasible improvements in speed and coverage for future iterations. We show proof of concept in performing fast, wide field spectral imaging with a simple, inexpensive design. With a reduction in size, cost, number of wavelengths used, and overall complexity, the system described by this dissertation allows for a more seamless scaling to higher pixel number and density in future iterations of the technology, which will help make this a clinically translatable tool for breast tumor margin assessment.

Dedication

To my beautiful wife, Jessica, and our children, Jordan & Jackson.

Contents

List of Tables

List of Figures

Symbols/Abbreviations

1CH – single channel fiber optic clinical system

1PD – single pixel photodiode based system

16PD – 16-channel (4x4 array) photodiode based system

49CH – 49-channel (7x7 array) fiber optic clinical system

8CH – 8-channel (4x2 array) fiber optic clinical system

9PD – 9-channel (3x3 array) photodiode based system

CCD – charge coupled device

Cr – crocin

DCIS – ductal carcinoma *in situ*

DR – diffuse reflectance

DRS – diffuse reflectance spectroscopy

DUMC – Duke University Medical Center

eCDF – empirical cumulative distribution function

Hb – hemoglobin

HbH – deoxy-hemoglobin

HbO_2 – oxy-hemoglobin

IDC – invasive ductal carcinoma

MC – Monte Carlo

n – sample size

n – index of refraction

NA – numerical aperture

NIR – near-infrared

NIRS – near-infrared spectroscopy

OCT – optical coherence tomography

PAT – photoacoustic tomography

PD – photodiode

R - reflectance

SNR – signal to noise ratio

SPX – spectroscopy

THb – total hemoglobin

UV – ultra-violet

VIS – visible

2-NBDG - 2-[N-(7-nitrobenz-2-oxa-1,3-diazol-4-yl)amino]-2-deoxy-D-glucose

βc – β-carotene

λ - wavelength

μ_a – absorption coefficient

μ_s – scattering coefficient

μ_s' – reduced scattering coefficient

$\langle\mu_a\rangle$ - wavelength averaged absorption coefficient

$\langle\mu_s'\rangle$ - wavelength averaged reduced scattering coefficient

[ ] - concentration

Acknowledgements

I would like to acknowledge all of the people who have offered scientific and personal support over the course of my graduate studies at Duke. In particular, I would like to thank my advisor, Nimmi Ramanujam, for her guidance and scientific contributions. It has been a privilege to have worked with such a motivated, driven, and distinguished researcher in the field. She has constantly reminded me to conduct research with a purpose and to understand the big picture. In addition to my advisor, I acknowledge that some of the most important mentors in my development as a scientist were the former postdoctoral researchers and scientists, Bing Yu and Quincy Brown, who have helped train me to be an effective, independent researcher. I would also like to acknowledge some of the current and former members of the Tissue Optical Spectroscopy Laboratory at Duke: Melissa Skala, Janelle Phelps, Lisa Richards, Vivide Chang, Stacy Millon, Karthik Vishwanath, Naras Rajaram, Christine Mulvey, Andy Liu, Torre Bydlon, Stephanie Kennedy, Henry Fu, Amy Frees, Jenna Mueller, Fangyao Hu, Brandon Nichols, Jennifer Gallagher, and Marlee Junker. They have made these years an enjoyable experience. I truly appreciate all of the support that they have given me, both as colleagues and as good friends.

This work would not have been possible without my excellent project collaborators, Nan Jokerst, Martin Brooke, Greg Palmer, and Sulochana Dhar at Duke

University and Tom Kuech and Leon McCaughan at the University of Wisconsin-Madison. All of the collaborators have provided valuable insights for this work, and I am thankful for all of the hard work that they have put in. I am also grately for my committee members, Kathy Nightingale and Robert Malkin, for providing an unbiased perspective and support for this dissertation.

In addition to all of the people who contributed scientifically to my dissertation mentioned above, I recognize that my time in Durham as a graduate student was much more enjoyable because of my church families at the former Grace Missions Community Church and at the Gathering Church. I will forever be grateful for their hospitality, friendship, and spiritual support. I am also appreciative of my flag football community of friends from the city leagues around the area. They provided great camaraderie and helped balance out my academic life with the sport that I love most.

Lastly, I would also like to like to thank my family for providing encouragement the past several years. I thank my parents, Jay and Christina, for their continued support throughput my whole life; my sister and brother-in-law, Monica and Daniel, for being an inspiration to be good at what I do; my in-laws, Joseph and Irene, for being truly the best in-laws that a guy can ask for; my son, Jordan, for being the most wonderful and easiest and sweetest toddler to care for; and my beautiful, loving, and patient wife, Jessica, for doing literally *everything* during my time in graduate school. I could not have done this without you.

1. Background and significance

1.1 Breast cancer prevalence and management

Although improvements in breast cancer screening, diagnosis, and treatment have decreased the mortality rate of the disease in the past several decades, the shift towards modern lifestyles has also contributed to the increase of breast cancer cases worldwide. Globally, there are over 1 million new cases and nearly 500,000 deaths due to breast cancer annually [1]. In the United States, the American Cancer Society estimates that approximately 200,000 new invasive breast cancers and over 60,000 new *in situ* breast cancers are diagnosed annually. It is a common disease that affects every individual. The best way to manage and treat the disease is early detection followed by chemotherapy, radiotherapy, and surgical removal of a small, non-metastic tumor.

The first step in breast cancer detection is a screening mammogram, which is recommended as an annual test for women over the age of 40. A patient with a suspicious mammogram typically undergoes an image-guided needle biopsy procedure and histopathologic diagnosis of the core tissue to determine if the sample is malignant. Cancer treatment often involves chemotherapy, radiation therapy, and/or surgery. The removal of the whole breast, a mastectomy procedure, may be performed to treat the cancer. With the advancement of imaging technologies along with improvements in chemotherapy and radiation therapy, many patients have the option of preserving the breast by choosing a procedure known as breast conserving surgery (BCS), also known

as partial mastectomy or lumpectomy. Figure 1 shows a flow chart of the clinical management of breast cancer with the end goal of preserving the breast while fully eradicating the disease.

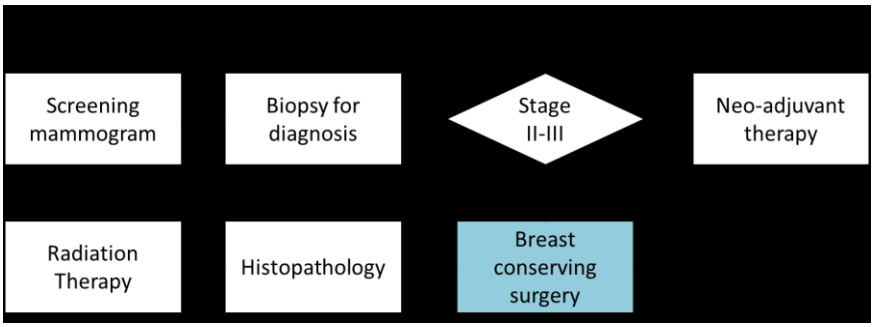

Figure 1: Flow chart for the typical clinical management of breast cancer with the goal of conserving the breast(s).

1.2 Breast conserving surgery

Women diagnosed with stage 0, I, or II breast cancer can choose to retain their breast by undergoing BCS. Patients diagnosed with stage II or III breast cancer can also undergo neo-adjuvant therapy to reduce the size of the tumor. This procedure is becoming increasingly more common and can provide a better cosmetic outcome compared to a mastectomy. Of the 260,000 women diagnosed with breast cancer in the United States annually, most are eligible for BCS. Approximately 165,000-180,000 women undergo this surgical procedure [2].

During BCS, the surgeon attempts to resect the tumor with a surrounding rim of normal tissue, as shown in Figure 2. After the surgery is completed, the specimen is submitted to pathology within a week of the surgery. The excised tissue is evaluated to determine if the margin is clear or negative (>2 mm from the tumor margin, shown in Figure 2(b), or if it is positive or close (<2 mm from the tumor margin). To further clarify the concept of breast tumor margin assessment, we can think of the excised specimen as an orange. If the orange is the tumor with the unwanted cancer cells, the rind is the surrounding rim of normal tissue that surgeons are to also remove. This rind must be greater than 2 mm for the margin to be considered clear or negative. If this margin is positive or close, then the patient is advised to undergo re-exicison surgery to achieve a negative margin. Obviously, this can have a variety of additional negative physical, emotional, and financial impact in the patient's life.

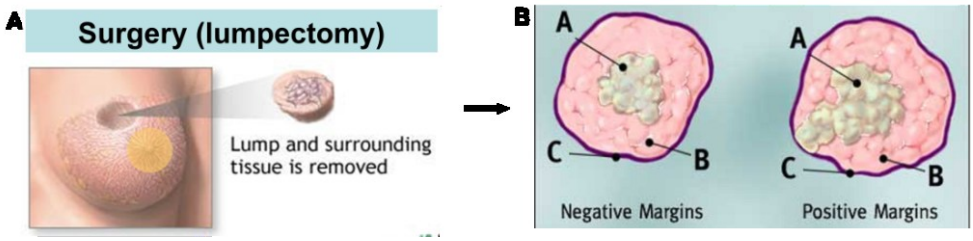

Figure 2: Illustrations of the goal of BCS in (A) removal of only the tumor while preserving as much of the breast as possible and in (B) achieving negative margins (c) in which a rim of normal tissue (b) is excised with the core tumor (a).

Following BCS, the patients typically also undergo radiation therapy to clean up any residual cancer cells that remain and that can potentially cause local tumor recurrence [3, 4]. Recently, meta-analyses by the Early Breast Cancer Trialists group showed that one death is averted for every four women in which a local recurrence is avoided. The pathologic margin status is an important predictor of local recurrence of an invasive or *in situ* cancer after BCS [5, 6]. Thus, complete tumor excision is essential to reduce the risk of recurrence [7].

Another critical aspect of BCS is to orient the specimen accurately so that the surgeon knows where to re-excise if needed. For specimen orientation, the lumpectomy specimen is often viewed as a cube. The surgeon orients the specimen by putting sutures and surgical clips at the center of four of the six margins: anterior, posterior, inferior, superior, medial, and lateral. The orientation is maintained in the pathology lab by differential inking of the six surfaces. If tumor cells are found microscopically between 0-2 mm from the margin, the specific margin is identified by the ink color of the sections submitted so the surgeon knows which portion of the lumpectomy cavity needs re-excision. This approach is effective to ensure complete excision of the residual disease in the second surgery [8]. However, an important goal is to avoid this second surgery completely. Depending on the quality of treatment centers and experience of surgeons, a staggering 20-70% of women are called back for re-excision surgery due to

the incomplete removal of the tumor, i.e. the post-excision pathological determination of a positive or a close margin [9-18].

1.2.1 Current practices for breast tumor margin assessment

There is no widely accepted tool for intra-operative breast tumor margin assessment to date. The inability to ensure that the cancer has been completely removed during the first surgery represents a very significant unmet clinical need for the patients, the surgeons, Medicare and Medicaid, third party payers, and public health. Less than 5% of all hospitals that perform BCS actually utilize intra-operative techniques to analyze such as touch preparation cytology and frozen section analysis.

Touch preparation cytology is a technique in which cells of the tissue surface are transferred to a glass slide by simply touching the specimen to the glass. The glass slide is stained for pathologic observations. Pathologists are able to evaluate the surfaces of the entire tumor specimen, though with a wide range of sensitivities (38%-100%) and specificities (83%-100%) [19-26]. This technique is time consuming and requires a pathologist present in the operating room at the time of the surgery. More importantly, the technique only surveys the surface layer of the lumpectomy specimen. As mentioned previously, the lumpectomy specimen must have >2 mm of surrounding normal tissue; thus, touch preparation cytology is unable to diagnose close margins (only 0-2 mm of normal tissue).

Frozen section analysis is a technique in which the tissue is frozen and sliced into microscopically thin sections for pathologic observation. This technique is a very challenging procedure, especially for tissues with high adipose content, such as in the breast. The sensitivity ranges from 59-91%, and the specificity ranges from 86-100% [22, 27-33]. Furthermore, pathologists will typically only sample a few select slices of the frozen sections; thus, the entire specimen is not evaluated. Table 1 shows a list of reported sensitivities and specificities in the literature for frozen section and touch preparation cytology. Ultimately, both techniques can be time and labor-intensive and are not widely used by hospitals performing BCS.

Table 1: Sensitivity and specificity for frozen section analysis and touch prepartion cytology.

	Frozen Section (%)		Touch Preparation (%)	
Author	**Sensitivity**	**Specificity**	**Sensitivity**	**Specificity**
Olson [28]	73.1	99.6		
Cendan [27]	59	100		
Sauter [23]	90	97		
Weber [30]	91	100		
Noguchi [31]	83	86		
Pleijhuis [32]	65-78	98-100		
Cabioglu [33]	78	92		
Komenaka [34]	74	100		
Fukamachi [35]	78.6	100		
Cox [36]			100	96.6
Creager [19]			80	85
Valdes [24]			75	82.8
Klimberg [25]			100	100
Johnson [26]			96.4	100
Saarela [23]			37.5	85.1
Komenaka [34]			61-79	100

1.2.2 Characteristics of an ideal intra-operative margin assessment tool

Through research study collaborations with breast surgeons and pathologists at Duke as well as helpful feedback from an external advisory board of a Bioengineering Research Partnership grant (NIH BRP – 1R01EB011574-01), we have generated a list of characteristics of an ideal intra-operative margin assessment tool to help surgeons ensure the complete removal of the tumor and thus reduce the risk of local recurrence. They are listed in the following:

(1) The device needs to be capable of surveying multiple margins and provide diagnostic information within 20 minutes.

(2) The device needs to have a sensing depth of 0-2 mm, which is the most widely accepted criterion for clear margins [37-41].

(3) The device needs have a 10-20 cm^2 surveillance area, which are the typical sizes of lumpectomy specimens at the Duke University Medical Center.

(4) The device needs to image with a spatial resolution on the order of millimeters, which is comparable to the thickness of slices evaluated by pathologists.

(5) The device needs to effectively detect differences between benign and malignant tissues and to do this without the need for immediate pathologic evaluation, or tissue processing.

An ideal intra-operative tool would not necessarily replace pathologist as the gold standard for determining margin status after surgery. Since the entire tumor specimen is never entirely examined by pathology, the tool would also be able to serve as an aid by guiding pathologists to the most suspicious areas on the tumor margin.

There is significant interest in both the academic and private sectors to develop a margin assessment tool. Arguably the most developed technology clinically is the MarginProbe built by Dune Medical in Israel. The MarginProbe uses radio waves to measure the electromagnetic properties of breast tissue over a 7 mm diameter area and 1 mm volume. Dune Medical has reported a 71% sensitivity and 68% specificity in a prospective trial with the MarginProbe [42, 43]. However, the probe is likely unable to survey the entire tumor specimen 7 mm at a time, and the 1 mm sensing depth means that it is unable to detect close margins. Dune Medical has not published any information regarding the breast tissue sources of contrast that the MarginProbe sees.

1.3 Biophotonics

Biophotonics broadly refers to all techniques that deal with the interaction between biology and light. These include the emission, detection, absorption, reflection, modification, and creation of radiation from molecules, cells, tissues, organisms, and biomaterials. Biophotonics applications have been applied to life sciences, medicine, agriculture, among others. There is high interest in optical imaging of tissue because it

is relatively fast and the non-ionizing photons are non-destructive to the tissue. Optical techniques leverage the absorption and scattering properties of tissue and do not always require expensive and/or potentially toxic contrast agents.

1.3.1 Behavior of photons in tissue: principles and definitions

When photons are launched into tissue, three events can happen: (1) scattering, (2) absorption, and (3) fluorescence. The extent to which these events happen is dependent upon the wavelength of the photon and the optical properties of the tissue. In this dissertation, the focus is on the optical technique known as diffuse reflectance spectroscopy (DRS), which typically involves a light source coupled to optical fibers. From the fibers, light is launched into and interacts with tissue. These interactions are indirectly measured when photons are scattered back to the tissue surface and collected by detection fibers or fiber bundles, which serve as a conduit of light to a charge-coupled device (CCD) or photomultiplier tube (PMT). The diffuse reflectance spectra collected by the CCD or PMT contains information about the wavelength-dependent tissue absorption and scattering propertiese. For the sake of brevity, the following descriptions of the light-tissue interaction are mostly in the context of DRS.

Scattering

Electromagnetic waves can undergo elastic or inelastic scattering. For an elastic scattering interaction in tissue, the direction of light travel is changed, but the light

intensity remains the same. Scattering properties can be quantified using the scattering coefficient, μ_s, which is the average number of scattering interactions occurring over a given pathlength. Tissue is predominantly a forward scattering medium, i.e. it does not scatter light in all directions with equal probability. The anisotropy factor, g, which equals the average cosine of the scattering angle, is used to quantify the probability of the directionality of a scattering event. When $g = 1$, the medium is completely forward scattering; when $g = 0$, the medium is isotropic (except for in the instance of Rayleigh scattering in which scattered particles are much smaller than the wavelengths of light). Throughout the remainder of this thesis, we will refer to the reduced scattering coefficient, μ_s', to quantify tissue scattering. μ_s' is defined as $\mu_s * (1 - g)$. This gives a measure of the effective scattering properties that takes into account both μ_s and g.

For an inelastic scattering interaction, the kinetic energy of the incident photons is <u>not</u> conserved, which results in the photons having a different frequency than at incidence. When photons interact with a scatterer, most of the photons are elastically scattered as described above, but a very small proportion of the incident photons (apprxomiately 1 in 10 million) are inelastically scattered. A main type of inelastic scattering for tissue is Raman scattering. The Raman effect refers to the absorption and emission of a photon with either lower energy (Stokes scattering) or higher energy (anti-Stokes scattering) than the incident photon. The number of inelastically scattered

photons are much lower than the elastically scattered photons, thus Raman scattering signals are generally very weak.

Absorption

An absorption interaction reduces the intensity of the light as photon energy is transferred to the absorbing molecule in tissue, such as hemoglobin (Hb). Like scattering properties, the absorption properties of turbid media can be described by the absorption coefficient, μ_a, which can be calculated using the Beer-Lambert Law given by $\mu_a(\lambda) = 2.303*\varepsilon(\lambda)*A*l$, where ε is the molar extinction coefficient (a measurement of how strongly a chemical species absorbs light at a given wavelength), A is the absorbance (or optical density), and l is the path length. Another term that is often used in optical spectroscopy is albedo, which is defined by μ_s / (μ_s + μ_a). Albedo describes the probability that a photon will be scattered as opposed to absorbed in the medium.

Fluorescence

Another light-tissue interaction that can occur is fluorescence, which is a component of the broader scope of optical spectroscopy. Fluorescence can occur following absorption of a photon by a fluorophore. A fluorophore first absorbs a photon, which promotes an electron from the ground state to the excited state. Once the excited state is reached, some energy is lost as the electron relaxes to the lowest

vibrational energy level within the excited state. Then, the electron may fall back to the ground state by emitting energy in the form of a fluorescent photon, typically at a longer wavelength than the original exciting photon.

1.3.2 Existing optical technologies

Numerous optical technologies that exploits the tissue-light interactions have been developed, and a few examples are listed in Table 2. These technologies can be broadly categorized into the following: photoacoustic tomography (PAT), spectroscopy, optical coherence tomography (OCT), and optical microscopy.

Briefly, PAT is a hybrid imaging modality, which involves delivering non-ionizing photons into tissue, which returns ultrasonic waves from the transient thermoelastic expansion. The ultrasonic waves are detected by transducers to form images associated with optical absorption of tissue. Optical spectroscopy may include near-infrared spectroscopy (NIRS), Raman spectroscopy, diffuse reflectance and fluorescence spectroscopy. These spectroscopic techniques vary fundamentally in the types of light-tissue interaction measured, i.e. fluorescence and elastic and inelastic scattering, as well as in the wavelength ranges of the light source. Optical coherence tomography (OCT) is a low coherence interferometic technique that usually utilizes near-infrared (NIR) light. Optical microscopy involves detecting visible light that is transmitted through or reflected from the sample. There are several techniques used to

quantify and improve spatial and axial resolution and contrast in microscopy. All of these optical technologies have potential to be useful in a variety of clinical applications for different organ sites.

Table 2: Comparison of existing optical technologies and their primary contrast, penetration depth, and spatial resolution in biomedical applications.

Optical Technique	Primary contrast	Depth (mm)	Resolution (μm)
photoacoustic tomography	absorption	3-50	45-700
near-infrared spectroscopy	absorption and elastic scattering	1-5	500-2000
Raman spectroscopy	inelastic scattering	1-3	500-2000
diffuse reflectance spectroscopy	absorption and elastic scattering	0.5-2	500-2000
Fluorescence spectrscopy	fluorescence and elastic scattering	0.5-2	500-2000
optical coherence tomography	elastic scattering	1-2	1-10
optical microscopy	fluorescence and elastic scattering	0.2	0.3-3

Table 2 shows that there is generally an inverse relationship between resolution and penetration depth for these various optical technologies. For example, cellular structure, which are on the order of sub-microns, can be examined using electron microscopy, where shallow penetration depths are acceptable and high resolution is needed. For applications involving whole organ imaging, optical technologies sacrifice resolution to obtain deeper penetration depths and wider fields of view. Because breast

margin assessment requires a technology that can probe up to 2 mm in depth and have a spatial resolution on the order of a few millimeters, optical spectroscopy is well-positioned to fill this clinical need.

1.4 Intrinsic sources of optical contrast in breast

The major endogenous absorbers in the visible spectrum in breast tissue are oxygenated and deoxygenated hemoglobin (HbO_2 and HbH) and β-carotene (βc), which are indicative of blood content, oxygenation, and adipocytes. These absorbers show very distinctive and wavelength-dependent spectral characteristics depending on its concentration and oxygenation. On the other hand, tissue scattering is sensitive to the size and density of cells as well as collagen, which provides structure and support for the tissue.

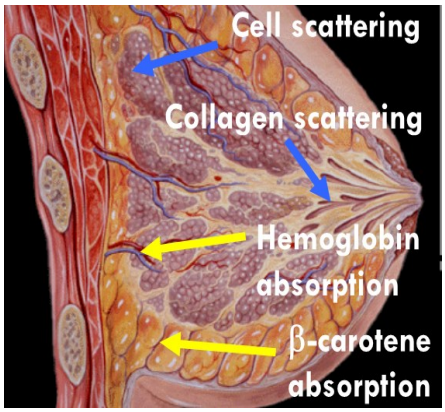

Figure 3: Sources of optical contrast in the human breast.

Figure 3 is a cartoon of the human breast with arrows pointing to the major sources of optical contrast due to absorption and scattering. Cellular structures and collagen in the breast cause light to scatter. Within the blood vessels, HbO_2 and HbH absorb light. β-carotene (βc), often stored in adipocytes (fat cells), is another primary absorber in breast tissue. Certain molecules, such as NADH and FAD, will fluoresce when illuminated with specific wavelengths of light.

Table 3: Optical sources of contrast in breast tissue.

Optical Technique	Tissue Interrogated	Source of Contrast	Disease Progression
Diffuse reflectance & elastic scattering spectroscopy [44-52]	adipocytes cells & collagen blood	βc scattering HbO_2 HbH	decrease increase decrease increase
Near-infrared spectral imaging [53-57]	water cells & collagen adipocytes blood	water scattering Lipids HbO_2 HbH	increase increase decrease decrease increase
Fluorescence spectroscopy [44, 48, 50, 52, 58, 59]	collagen fibers cells	collagen NADH, FAD, retinol, tryptophan	increase
Raman spectroscopy [60-63]	blood adipocytes variety of cells	heme lipids carotenoids tryptophan cholesterol	increase decrease decrease
optical coherence tomography [64, 65]	cells sub-cellular organelles	scattering	increase

The various optical tools that have been used to measure breast composition are listed in Table 3. All of these previous studies suggest that the main sources of optical contrast for differentiating benign from malignant tissues are related to breast vasculature (Hb), fat (by measuring βc content) , collagen, and cells.

1.5 Emerging optical tools for margin assessment

A number of academic and commercial groups have worked on or are currently developing tools for intra-operative breast tumor margin assessment. For the sake of brevity, the following sections includes only those for which some clinical validation is reported.

1.5.1 Optical contrast through single-point measurements

In 2000, Irving Bigio of Boston University conducted a pioneering study using diffuse reflectance spectroscopy to look at *in vivo* sites on the tumor bed in 24 patients (13 cancer and 59 normal sites). They showed that malignant and benign sites could be separated with a sensitivity of 67% and a specificity of 79% [66]. Although the study only utilized single-point sampling of a fiber optic probe and did not involve any margin assessment, it paved the way for many other research groups to investigate optical imaging, specifically for the application of breast tumor margin assessment.

In 2009, Michael Feld conducted a prospective study at MIT using Raman spectroscopy to examine freshly excised lumpectomy specimens, which were sliced to

expose tumor sites in 21 patients (123 benign and 6 malignant tissue sites) and reported a sensitivity of 83% and a specificity of 93% [61]. A previous retrospective study showed 94% sensitivity and 96% specificity for *ex vivo* measurements of frozen samples [67]. His group also demonstrated the ability of using DRS and fluorescence spectroscopy to differentiate various benign and malignant tissues in breast biopsies from 17 patients (95 benign and 9 malignant sites), resulting in a sensitivity of 100% and a specificity of 96% [50].

In 2010, Anita Mahadevan-Jansen at Vanderbilt University also published on using diffuse reflectance and fluorescence spectroscopy to detect cancerous sites on breast tumor margins in 32 patients (145 normal and 34 individual tumor sites). The group reported a sensitivity and specificity of 85% and 96%, respectively, for classifying individual sites [46]. In 2011, TJ Ruers from the Netherlands Cancer Institute also used DRS to acquire spectra from 102 *ex vivo* samples that consisted of adipose, glandular, fibroadenoma, invasive carcinoma, and ductal carcinoma *in situ* (DCIS). They were able to separate malignant and benign samples with a sensitivity of 94±4% and a specificity of 98±2% [68]. All of these recent studies show the great potential of using optical tools for breast tumor margin assessment. However, these studies also reveal that the respective optical techniques cannot be practically used in a clinical setting to survey the entire tumor margin rapidly because these optical probes all use single-point sampling.

Finding malignancies in a very large specimen with a single-channel probe is like looking for a needle in a haystack.

1.5.2 Toward wide field imaging of breast tumor margins

As of 2012, only two groups have published clinical data to show feasibility of performing full tumor margin optical imaging. Stephen Boppart at the University of Illinois showed that OCT can potentially be used for breast tumor margin imaging. In 20 patients (9 positive and 11 negative margins), they used OCT imaging to diagnose tumor margins with a sensitivity and specificity of 100% and 82%, respectively [69].

Over the past decade, my group at Duke University has developed several iterations of margin assessment tools based on the principle of diffuse reflectance spectroscopy. Initially, we showed proof of principle in differentiating between normal and malignant breast tissue with a single-channel (1CH) benchtop system similar some of the work described previously [51, 70]. To cover the area of a large tumor margin and to make the system more clinically translatable, the most logical next step was to multiplex the single-channel probe. We then developed a coarse, 8-channel (8CH) first generation spectral imaging system for true margin assessment, shown in Figure 4(a) [45, 71, 72].

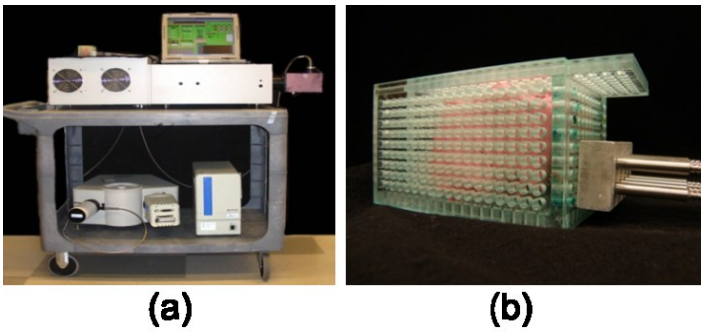

Figure 4: Photographs of (a) 8CH clinical instrument and (b) imaging probe interfaced with specimen box.

The engine of this benchtop spectral imaging system is a broadband source that emits at visible wavelengths, an 8-channel fiber optic imaging probe, an imaging spectrograph, and a charge coupled device (CCD) camera. Light is relayed between the clinical instrument and each discrete site on the tumor margin within a specimen box, shown in Figure 4(b), via the imaging probe, which consists of 8 channels of illumination and collection optical fibers. The probe is manually translated horizontally and vertically by 5 mm to sample inter-leaving holes between a channel-to-channel spacing of 10 mm. In this manner, 4 successive placements of the probe can sample an area of 2x4 cm with 5 mm resolution and a sensing depth of 0.5-2.2 mm for 450-600 nm. The diffuse reflectance spectra per site were analyzed with a feature extraction algorithm based on a fast, scalable Monte Carlo model of reflectance to quantitatively determine absorption and scattering contrast in the breast [49, 73].

A clinical study involving 120 patients undergoing BCS from 2007 to 2009 was completed using this first generation 8CH optical device [45, 47, 71, 72]. With this system, we were able to detect margin positivity with a sensitivity of 79.4% and a specificity of 66.7%. The study showed that the 8CH fiber optics system has comparable sensitivity to currently available tools, such as frozen section shown in Table 1, but it has the benefits of not requiring any type of tissue cutting, preparation, or a pathologist in the operating room. This technique can also potentially be more advantageous than touch preparation cytology in that it can survey deeper into the tissue for studying close margins up to 2 mm into the tissue specimen. Throughout the study, the clinicians also provided important feedback to help future iterations of system design.

1.5.3 Challenges and limitations of optical imaging

Table 4: Comparison of reported margin assessment technologies with respect to surgeon needs

Method	Quantitative / diagnostic	1-2mm depth	Covers margin	Non-destructive	< 20 min
Touch prep	✔			✔	
Frozen section	✔				
Raman SPX [62]	✔	✔		✔	
DRS [74]	✔	✔		✔	
OCT [75]				✔	
DRS imaging [72]	✔	✔		✔	

All of the previously mentioned technologies, both single-point sampling and imaging, fall short of the the ideal intra-operative margin assessment requirements

shown in Table 4. The table reveals the gaps that exist in each of the technologies, including our DRS coarse imaging system.

Although the 8CH system is a good tool for proof-of-concept studies, it is not practical for an intra-operative setting where time, cost, and space are limited. Figure 5 shows the sizes of the 125 tumor margins observed in our previous clinical study. Because the 8CH imaging probe only covers a 4 cm x 2 cm area at 10 mm spatial resolution for one placement, it would take up to 4 placements of this probe to achieve a 5 mm spatial resolution for a typical 10-20 cm^2 area per margin. Since each specimen has 6 total margins, it is not possible to survey the entire tumor and provide adequate margin diagnosis in the limited amount of time in the operating room. Thus far, none of the available tools can cover all margins and provide diagnostic information in under 20 minutes in the operating room.

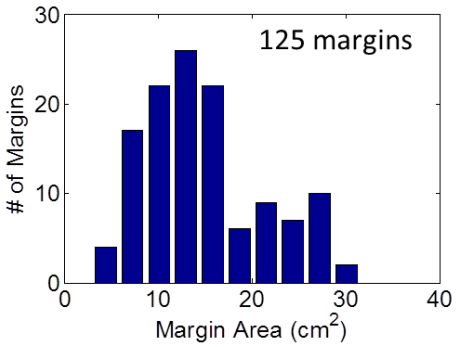

Figure 5: Areas observed across 125 lumpectomy specimen margins at Duke University Medical Center.

1.6 Objective and major outcomes

The goal of my dissertation is to design, engineering, and test a novel quantitative miniature spectral imaging system that utilizes the same scientific principles of our fiber optics based imaging systems described in this chapter, but improves upon technical issues, such as size, complexity, and speed, to meet the stringent demands of the intra-operative setting. The design is based on using a broadband source with a bandpass filters as the light source (with the potential of using LEDs in the future) and using an array of custom annular photodiodes as the detector, replacing the CCD and spectrograph. The rationale is that photodiode arrays are inexpensive and more easily scalable to cover the surveillance area necessary for the application of breast tumor margin assessment. Additionally, by discretizing the light sources with individual bandpass filters, I show proof of concept for the implantation of LEDs in the future, which allows for a much more portable, compact, and cost effective spectral imaging device without the high power consumption of the expensive and heavy broadband source. The major outcomes of my dissertation are as follows:

(1) I have demonstrated the feasibility of replacing sophisticated CCD and imaging spectrograph of the 8CH clinical system with simple, inexpensive silicon photodiodes (PD) for collecting diffuse reflectance spectra. This idea is described in Chapter 2.

(2) I have provided a strategy for quantitative spectral imaging of tissue absorption and scattering using photodiodes and LEDs by designing and builing a single-channel version of a fiber-illumination, PD-detection hybrid system and simulating reduced-wavelength, increased bandpass spectra for LED sources. The probe geometry that maximized SNR and had the appropriate sensing depth for margin assessment was determined to be an annular PD with central illuminator. The single channel PD-based probe was comparable in performance to the 1CH clinical benchtop system. This work is shown in Chapter 3.

(3) Through collaborations with Nan Jokerst and Martin Brooke, I have designed and tested a fiber-less imaging system based on a customized 4x4 thin PD array with free space illumination through the PD apertures built in-house. I was able to improve system SNR, extract optical properties from tissue phantoms with 8-15% accuracy for μ_a and μ_s'. In addition, I compared the extracted tissue parameters in a mouse tumor model from the imaging system and a commercial spectrofluorometer and found that the extracted parameters of both systems are within 10% of each other, further providing evidence that the PD-based array with 8 discrete wavelengths can replace the much more complex fiber imaging systems. The details of this major outcome are described in Chapter 4.

(4) I have developed a wavelength optimization strategy for designing a spectral imaging system for breast tumor margin assessment by combining the inverse Monte Carlo model of reflectance with a genetic algorithm. To design a more compact and cost-effective spectral imaging system, it is important to have as few wavelengths as possible while maintaining a high accuracy for extracting quantitative endpoints. The method can be used for a variety of system design processes in clinical applications beyond breast tumor margin assessment. This is described in Chapter 5.

(5) I have made the necessary modifications based on the previous bullet points and validated a 16-channel PD-based imaging system that is capable of extracting tissue phantom optical properties with comparable or improved accuracy to both the 8CH and a new 49-channel (49CH) fiber optic clinical systems. Side-by-side comparisons between the 49CH system and PD-based imaging system were made for SNR, speed, size, and extraction of composition maps in porcine tissue and human breast tissues. This important contribution is presented in Chapter 6.

2. Modification of diffuse reflectance spectroscopy detection components: a proof-of-principle study

In Chapter 2, the very first conceptual re-design of a diffuse reflectance spectral imaging system for margin assessment is discussed. I introduce the principle components of the fiber optics based clinical systems in greater detail and discuss the modifications to the detection components made in this iteration of system design and development.

2.1 Introduction

As defined in Chapter 1, ultraviolet-visible diffuse reflectance spectroscopy (UV-VIS DRS) is sensitive to the absorption and scattering properties of biological molecules in tissue and thus has great potential to be used as a tool for quantitative tissue biology. A major absorber of light in tissue in the visible range is hemoglobin (Hb), which shows distinctive, wavelength-dependent absorbance characteristics depending on its concentration and oxygenation. Tissue scattering is sensitive to the size and density of cellular structures such as nuclei and mitochondria. Thus, DRS of tissues can be used to quantify changes in oxygenation, blood volume and alterations in cellular density and morphology. Potential clinical applications of UV-VIS DRS include monitoring of tissue oxygenation [76] and blood loss [77], pre-cancer and cancer detection [78, 79], assessing

tumor response to cancer therapy [76], and intra-operative tumor margin assessment [72], which is the focus of this dissertation.

2.1.1 DRS instrumentation – 1CH clinical system

Over the past decade, our group has developed several iterations of margin assessment tools based on diffuse reflectance spectroscopy. Prior to performing margin assessment studies with spectral imaging systems, we showed proof of principle in differentiating between normal and malignant breast tissue with a single-channel (1CH) benchtop system [51, 70].

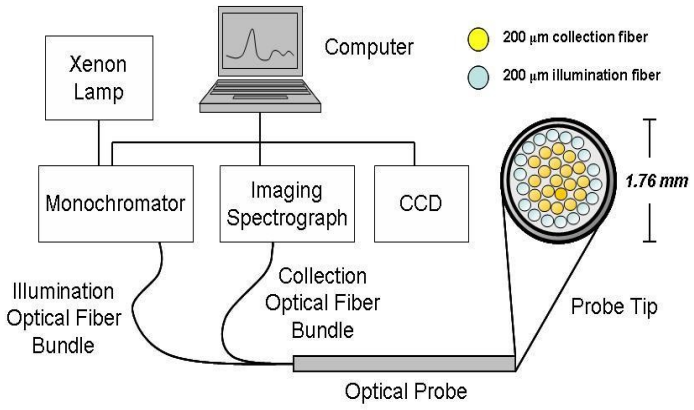

Figure 6: Schematics of the CH1 clinical system and probe tip

A schematic representation of our initial benchtop 1CH system is shown in Figure 6. The system consists of a 450 W Xenon arc lamp (JY Horiba, Edison, NJ) and a scanning monochromator (Gemini 180, JY Horiba) as the source. A fiber optic probe

with a core of 19 illumination fibers surrounded by a ring of 18 detection fibers is used for illumination and collection. The individual illumination and collection fibers had a diameter of 200 μm and a numerical aperture (NA) of 0.22. The effective illumination diameter of the probe is 1 mm. The remitted light is collected by the outer ring of detection fibers and coupled through an imaging spectrograph (Triax 320, JY Horiba) and detected by a CCD (Symphony, JY Horiba). Previously published studies by our group show that this technology is capable of quantifying breast and oral tissue physiological and morphological properties and that these quantities can be used to discern between malignant and non-malignant tissues with sensitivities and specificities exceeding 80% [49, 51, 80].

2.1.2 Monte Carlo model of reflectance

Central to the spectral analysis in our work is a Monte Carlo (MC) model of reflectance that is able to reliably and quantitatively determine the underlying sources of optical contrast in the breast, specifically the absorption and scattering [73]. As previously defined, the absorption coefficient, μ_a, is a linear combination of the product of the extinction coefficients and concentrations of constituent absorbers in tissue, such as β-carotene and hemoglobin, while the scattering coefficient, μ_s, reflects the size and density fo the cells and sub-cellular organelles in the tissue. The MC model extracts and quantifies these properties from tissue, and these extracted sources of contrast are then used to create molecular tissue composition maps, which are then applied to a

predictive model to classify positive, close, and negative tumor margins. Developed by Gregory Palmer in our group, this model is used extensively in all studies described in this dissertation. It consists of two parts, the forward and inverse models, which are described briefly here.

Forward model:

The forward model refers to the model that relates the tissue physiological and structural properties to its modeled diffuse reflectance. Figure 7(a) shows a flow chart of the forward MC model of diffuse reflectance. The model has two sets of inputs, which are used to determine the absorption and scattering coefficients. The variable parameters in the model are the concentrations (C_i) of each chromophore assumed in the specific tissue, such as Hb and βc in the breast. The corresponding wavelength-dependent extinction coefficients for each chromophore $\varepsilon_i(\lambda)$, a fixed parameter, are used to determine the wavelength-dependent absorption coefficient, $\mu_a(\lambda)$, according to the relationship, $\mu_a(\lambda) = \Sigma\, ln(10)\, \varepsilon_i(\lambda)\,(C_i)$. For scattering estimation, the variable parameters are the scatterer size and density. The fixed parameter is the refractive index, n, according to known values for tissue phantoms. Mie theory for spherical particles is used to model scattering. The wavelength-dependent scattering coefficient, $\mu_s(\lambda)$, and the anisotropy factor, $g(\lambda)$, are then calculated. With a MC model of light transport, a

diffuse reflectance spectrum can be obtained using the input optical properties, $\mu_a(\lambda)$, $\mu_s(\lambda)$, and $g(\lambda)$.

Typically a Monte Carlo simulation would be required for each unique set of optical properties, thus making model impractical to use in a clinical setting. To make this model efficient and clinically useful, a scaling approach described by Graaff et al. [81], a simplified anisotropy factor estimation relating to μ_s', a convolution over the probe geometry to determine the photon collection probability, and a lookup table of reflectance values for a given range of relevant tissue optical properties were all incorporated into the algorithm.

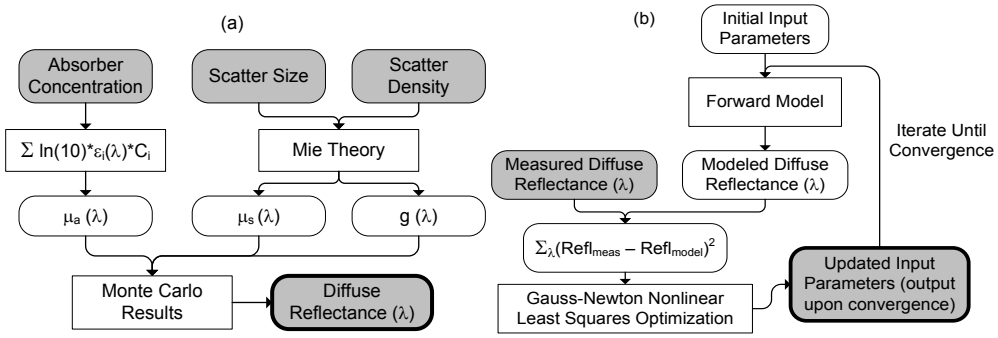

Figure 7: (a) forward and (b) inverse Monte Carlo models of diffuse reflectance. Input boxes are shaded, and output boxes are shaded with a bold outline.

Inverse model:

To extract tissue parameters from the acquired diffuse reflectance, we use the inverse MC model, shown in Figure 7(b). First, an initial set of free parameters (absorber

concentration and scatterer size and density) are input into the forward model. The fixed parameters are the wavelength-dependent extinction coefficients of the absorber and the refractive index of the scatterer and the surrounding medium. These input parameters are used in the forward model to generate the Monte Carlo modeled reflectance as a function of wavelength. Next, the sum of squares error between the modeled and measured reflectance is computed. The free parameters are then iteratively updated until the sum of squares error is minimized. A Gauss-Newton nonlinear least squares algorithm is used for optimization. To ensure convergence to a global minimum, the procedure is iterated many times for a tissue sample, with a different, randomly chosen set of starting parameters.

2.1.3 Design considerations

Although the 1CH clinical system coupled with the MC model is a robust toolbox for non-destructively and rapidly quantifying tissue optical properties, this system suffers from several drawbacks. First, optical fibers generally collect only a very small portion of the remitted signal thus requiring high quantum efficiency, low noise detectors, particularly in the UV-blue spectral region. Secondly, optical fiber-based detection, while reasonable for single-point sampling, is also unwieldy and expensive when expanded for use in imaging applications, which is important for margin assessment. Thus, a simpler, low-cost, more portable reflectance spectrometer, capable

of making fast measurements at multiple sites is desired in a clinical setting, including other applications unrelated to breast tumor margin assessment [82]. In addition, the conventional spectrometers that require a CCD and an imaging spectrograph for detection have a relatively large footprint and are not portable. Previous studies have attempted to develop portable DRS systems for cancer detection. Cerussi et al. developed a handheld (5x8x10 cm) laser breast scanner based on frequency-domain near-infrared spectroscopy for breast cancer detection [83]. Feather et al. reported a portable diffuse reflectometer that uses nine LEDs at three visible wavelengths to illuminate skin and a photodiode to collect diffusely reflected light through a 7 mm aperture [82]. The laser breast scanner has a sensing depth over 1 cm, thus is not appropriate for tumor margin assessment, and is difficult to multiplex into a spectral imaging device because of the size of the device. The LED-photodiode based reflectometer is extendable to imaging, but measurements based on this device does not provide quantitative endpoints such as absorption and scattering, which relate to the underlying biology of the tissue.

Our ultimate goal is to develop a cost-effective, portable, wide field spectral imaging device for quantifying tumor physiology and morphology, specifically the features that differentiate between malignant and non-malignant breast tissues with performance comparable to its benchtop counterpart. The conceptual design of this portable device is an optical probe with the integration of several light emitting diodes

(LEDs) and photodiodes covering the wavelength range of 400-600 nm. In addition to its compactness and low cost, the device would have several advantages over the fiber optics based clinical systems. First, LEDs have much high power density and longer lifetime than traditional lamps and bringing the light source in direct contact with tissue significantly improves light delivery efficiency. Secondly, replacing the detection fiber or fiber bundle with a photodiode remarkably increases the light collection efficiency because photodiodes usually have a larger detection area and a much higher numerical aperture (NA) than any optical fibers. Furthermore, the probe can be used as a reliable way of measuring intensity spectra while a fiber optic probe is subject to light fluctuation due to fiber bending in clinical environments. Finally, such a device offers great potential for multiplexing diagnostics and imaging. The major cost for this DRS system redesign is the reduced number of wavelength and the finite bandwidth (FWHM) of LEDs. Details about wavelength reduction and bandwidth effects is reported in Chapter 5.

In this chapter, we describe the development and testing of a single-point hybrid optical probe which consists of a multimode illumination fiber and a silicon photodiode as a first step towards the long-term goal of developing a compact imaging device that can survey multiple points simultaneously. We demonstrate that diffuse reflectance spectra measured with the hybrid system coupled with our inverse MC model of

reflectance provides quantitative measures of tissue absorption and scattering with accuracy that is comparable to that of the 1CH clinical system [73].

2.2 Materials and methods

2.2.1 Schematic of single-point hybrid optical device

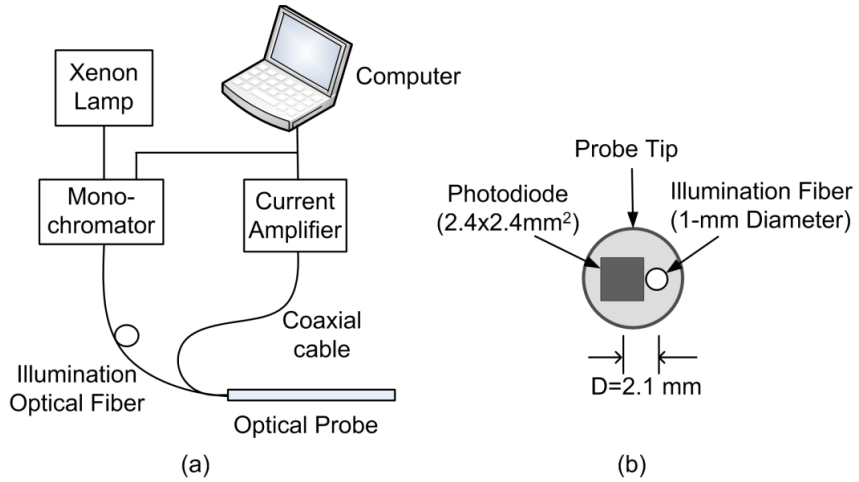

Figure 8: Schematic of (a) modified spectrometer and (b) probe tip.

The hybrid optical system, shown in Figure 8(a), consists of a 450-W xenon lamp and monochromator (JY Horiba, NJ), a 1-mm illumination optical fiber (NA=0.22), a 2.4×2.4 mm silicon photodiode (S1226, Hamamatsu, Japan) with a low noise current amplifier (PDA-750, Terahertz Technologies Inc., NY), and a laptop computer. The hybrid system uses the same light source and monochromator and an illumination fiber with similar diameter and NA as the original 1CH clinical system. The primary

difference between the two systems is that the photodiode and current amplifier in the new system replace the collection fibers, spectrograph and CCD camera in the 1CH system. At the distal end of the probe, shown in Figure 8(b), the edge of the photodiode was trimmed to the active area and transparent epoxy was used to bond the cleaved fiber adjacent to the photodiode, such that the center-to-center distance between the illumination fiber and the photodiode is 2.1 mm. The overall diameter of the probe tip is 6 mm.

2.2.2 Optical measurements in tissue phantoms

To evaluate the capability of the modified hybrid system for measuring tissue optical properties, a series of experiments were conducted on homogeneous liquid tissue-mimicking phantoms with absorption coefficient (μ_a) and reduced scattering coefficient (μ_s') representative of human breast tissues in the 400-600 nm wavelength range [73]. Phantoms were created with 1-μm diameter polystyrene spheres (07310-15, Polysciences, Inc., PA) as the scatterer and variable concentrations of the absorber, hemoglobin (Hb) (H0267, Sigma Co., MO). Two sets of liquid phantoms were created by titrating absorber at two scattering levels, and all diffuse reflectance measurements were made the day the phantoms were prepared. The first set of phantoms (1A-1E) consisted of five low scattering phantoms (wavelength-averaged μ_s'=12.5 cm^{-1}) with wavelength-averaged μ_a of 0.5, 0.9, 1.3, 1.6, and 2.0 cm^{-1} over the 400-600 nm range. The second set (2A-2E) consisted of five high scattering phantoms (wavelength-averaged μ_s'=21.7 cm^{-1})

with the same absorption properties as the first set. This produced a total of 10 phantoms with an overall μ_a range (0.035-10 cm^{-1}) and μ_s' range (9.2-22.2 cm^{-1}). The optical properties of the phantoms can be found in Table 5.

Diffuse reflectance measurements were made for each liquid phantom. The entrance, side, and exit slit widths of the monochromator were optimized so that the power was maximized while the bandpass was fixed at 4.5 nm. The maximum power out of the illumination fiber was 130 μW at 470 nm, and the minimum power was 65 μW at 590 nm at the output of the illumination fiber. A complete diffuse reflectance spectrum was collected from each phantom by scanning the bandpass of the monochromator from 400-600 nm at increments of 5 nm. Three scans were taken for each phantom. Then, a diffuse reflectance spectrum was also obtained from a Spectralon 99% diffuse reflectance puck (SRS-99-010, Labsphere, Inc., North Sutton, NH) with the probe in contact with the puck immediately after the phantom measurements with the same instrument settings.

2.2.3 Phantom data analysis

The inverse MC model was used to extract μ_a and μ_s' from the liquid phantoms. An attribute of the scalable MC model of reflectance is that it accounts for the specific probe geometry used for diffuse reflectance measurements. At the time of the experiment, the model was only set up to simulate circular sources and detectors because optical fibers were so widely used in this field. To be able to use the MC model

for the probe geometry shown in Figure 8(b), we imaged the square detector under a microscope, generated a circular detector with active area equivalent to that of the square detector as an estimation. The method for modeling probe geometry was improved in subsequent iterations, beginning in Chapter 3.

To experimentally compare measured phantom spectra to MC simulated phantom spectra for the fitting process in the inverse model, the "calibrated" diffuse reflectance spectrum of the target phantom for which the optical properties are to be quantified was divided point by point by the "calibrated" diffuse reflectance spectrum of a reference phantom with known optical properties. The term, "calibrated," in both cases refers to the normalization of the diffuse reflectance spectrum to that measured from the Spectralon puck for correction of the wavelength-dependent response of the instrument. In this phantom study, one phantom (1C: μ_a = 1.28 cm^{-1}, μ_s'=10.6 cm^{-1}) was selected as a reference phantom and the remaining nine phantoms were used as target phantoms. Then, the inversions were repeated for all target-reference phantom combinations. The extracted μ_a and μ_s' for each target phantom were averaged at each wavelength over all the 9 reference phantoms. Bender et al. previously provided guidelines for the selection of a reference phantom [84].

2.3 Results and discussion

2.3.1 System drift and SNR estimation

Prior to the phantom experiments, the long-term drift and signal-to-noise ratio (SNR) of the system were characterized. With the lamp on and the probe tip in contact with the surface of a liquid phantom, we determined that the long-term drift of the system was less than 1 nA over two hours. The typical signal range was between 0.5-5.0 μA. By taking three consecutive diffuse reflectance spectra from 400-600 nm in phantom 2E, the darkest among the ten phantoms for our worst case scenario, we calculated an average SNR of 42.9 dB over all wavelengths, where SNR is defined as 20*log(mean intensity/standard deviation). The a minimum SNR, however, was only 24.6 dB at 410 nm, which is close to the Soret band absorption of oxyhemoglobin.

The low SNR at the shorter wavelengths can be attributed to both the lower responsivity of silicon photodiodes in the UV-blue range, as well as the un-optimized probe geometry of this hybrid system. Figure 9 shown the MC simulation results of percent diffuse reflectance as a function of distance for phantom 2E. The diffusely reflected photons drop off drastically as distance from the source increases. Because the geometry of this design iteration is such that the illumination fiber sits adjacent to a 2.4x2.4 mm^2 photodiode, much of the detector active area is actually wasted space. The photons launched from the 1 mm fiber will have a low probability of being collected by

almost half of the detector area. A new probe geometry that resulted in a higher SNR is presented in Chapter 3.

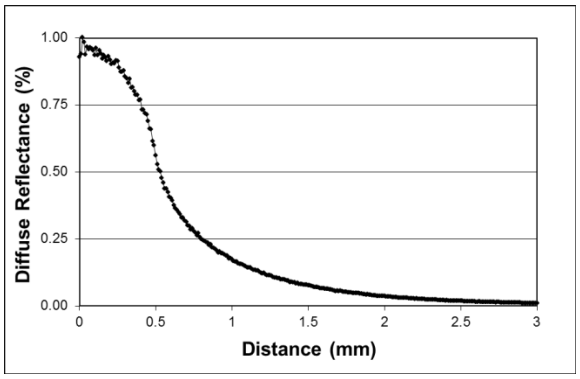

Figure 9: Simulated diffuse reflectance as a function of distance for μ_a=2.0 cm^{-1}, μ_s'=20.4 cm^{-1} (phantom 2E).

2.3.2 Extraction of phantom optical properties

Figure 10 shows the Spectralon puck-calibrated reflectance spectra for two phantoms 1A and 1E and the corresponding fits to the inverse MC model. The three valleys at 415, 540 and 575 nm on the spectra for both phantoms are the Soret band (400–450 nm), beta band (540 nm) and alpha band (569 nm) of oxygenated hemoglobin, respectively. There is excellent agreement between the measured spectra and the MC fits. Figure 11(a) and (b) show the extracted versus expected μ_a and μ_s' for all wavelengths over the 400-600 nm range quantified with the modified and original systems. The correlation coefficient for μ_a and μ_s' are 0.9956 and 0.9277, respectively for optical properties quantified with the modified hybrid system. An overall error of 8.0±6.2% was calculated for μ_a and 8.9±6.5% for μ_s' for the modified system. For the purposes of comparison, the original

1CH system had an overall error 9.2±12.4% and 4.4±3.4% for extracting μ_a and μ_s', respectively [84].

Table 5 provides a summary of the optical properties of the 10 phantoms and the respective extraction errors.

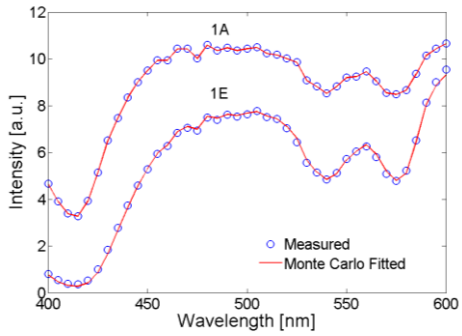

Figure 10: Calibrated measured and Monte Carlo fitted tissue phantom spectra.

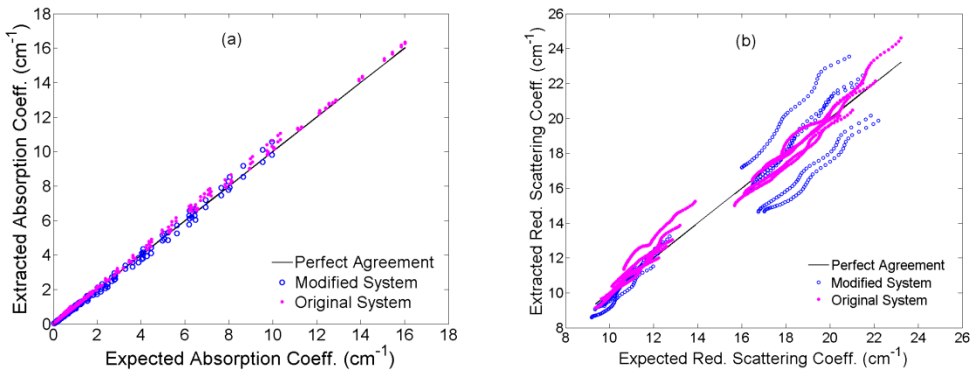

Figure 11: Extracted vs. expected (a) absorption coefficient and (b) reduced scattering coefficient.

Table 5: Summary of the phantom optical properties and percent error in extracted optical properties.

Phantom	Optical Properties over 400-600 nm				Extraction Errors	
	Avg μ_a (cm^{-1})	μ_a range (cm^{-1})	Avg μ_s' (cm^{-1})	μ_s' range (cm^{-1})	μ_a (%)	μ_s' (%)
1A	0.5	0.035-2.5	12.5	9.8-12.7	10.1	8.8
1B	0.9	0.063-4.5	12.3	9.6-12.5	6.4	7.9
1C	1.3	0.091-6.5	12.1	9.5-12.3	5.6	7.0
1D	1.6	0.11-8.0	11.9	9.3-12.2	5.2	6.3
1E	2.0	0.14-10	11.7	9.2-12.0	6.7	7.8
2A	0.5	0.035-2.5	21.7	17.0-22.2	14.8	15.5
2B	0.9	0.063-4.5	21.4	16.7-21.8	10.0	12.7
2C	1.3	0.091-6.5	21.0	16.5-21.5	9.2	5.1
2D	1.6	0.11-8.0	20.8	16.3-21.2	6.7	5.3
2E	2.0	0.14-10	20.4	16.0-20.9	5.2	12.4
Overall	0.035-10		9.2-22.2		8.0±6.2	8.9±6.5

2.4 Conclusions

The modified hybrid system can quantify absorption coefficients from phantoms with only modest absorption coefficients (up to 10 cm^{-1} with an average μ_a of 2.0 over 400-600 nm). This is sufficient for optical properties seen in cervical tissue [85]; however, our previous breast margin assessment studies have observed a average μ_a range of 2-8 cm^{-1}, which makes this particular probe geometry unsuitable for breast tumor margin assessment even if multiplexed for imaging. Compared to the original 1CH system, the modified system has higher errors in extraction of scattering coefficient due to its 10-15 dB lower SNR for high scattering. We eventually improved the dynamic range of the

system by decreasing the center-to-center distance between the source and detector as well as by increasing the area of the photodiode, which is discussed in Chapter 3.

This modified hybrid system, which employs both an illumination fiber and a photodiode, has significantly lower cost and better collection efficiency than the original 1CH system because of the larger effective NA of the silicon photodiode (NA≈0.96) and its direct contact with the sample. The modified system, in its current form with fiber illumination, can be easily multiplexed into a spectral imaging device. This can be achieved by interfacing a bundle of optical fibers to the exit slit of the monochromator. The individual fibers can be separated at the distal end (at the sample) such that each fiber is coupled to a discrete photodiode on the sample surface.

Through this initial iteration of system design, we determined that this single-point hybrid system combined with the inverse MC model can be extended into an optical spectral imaging system to map out the concentrations of absorbers, and the bulk tissue scattering properties of sub-surface tissue volumes (that are on the length scale of a couple of millimeters). In addition to breast tumor margin assessment, there are a number of applications for which this technology would be ideally suited including, epithelial pre-cancer and cancer detection (such as those of the skin, oral cavity and cervix) and the monitoring of tumor response to therapy. There are a number of previous publications that report on optical spectral imaging technologies for sub-surface tissue evaluation [86, 87], which relay the light to and from the tissue via non-

contact optics. The illumination and collection geometries are designed to maximize throughput and are not necessarily optimized to provide a well-defined sensing depth, which is important for tumor margin assessment. The spectral information obtained with these systems is generally displayed as intensity maps at a few discrete wavelengths and thus, do not fully exploit the information content in the data and also, do not provide any direct functional or structural information. For our goal of tumor margin assessment, we need to design a system that provides quantitative information on tissue composition via measurements of absorption and scattering. The illumination and collection geometry can be designed to have a well-defined sensing depth. An important modification to this DRS system re-design is the implementation of photodiodes at the tissue surface in place of the imaging spectrograph and CCD at the distal end of fibers. This potentially improves the collection efficiency as well as reduces the cost and larger system footprint associated with sophicated CCDs and imaging spectrographs.

3. Toward quantitative tumor margin assessment using photodiodes and LEDs

This chapter discusses a strategy for performing quantitative spectral imaging of tissue absorption and scattering using photodiodes and discrete sources, such as LEDs. Building upon the detector modification discussed in Chapter 2, we identified the probe geometry for a fiber-illumination, PD-detection hybrid system to achieve high SNR and proper sensing depth for margin assessment. Initial simulations were made to assess the feasibility of using LEDs by reducing the number of wavelengths and increasing the full-width half-maximum (FWHM). We also evaluated optical crosstalk between individual PDs and took steps towards multiplexing the detectors for spectral imaging.

3.1 Introduction

The ability to quantify tissue physiological and morphological properties can have tremendous impact in many clinical situations, potentially improving the clinical management and care of patients [88, 89]. Because diffuse reflectance spectroscopy in the UV-visible spectral range is sensitive to the absorption and scattering properties of biological molecules, such as hemoglobin, cell nuclei, and mitochondria, several groups have investigated the technology as a tool for monitoring tissue oxygenation [90], pre-cancer and cancer detection [74, 79, 91-93], tumor margin assessment [94], assessing tumor response to therapy [95-97], and in other biomedical applications [76, 77, 98]. As

discussed in Chapter 1 and Chapter 2, we have previously developed a fiber-optic based diffuse reflectance spectroscopy system (1CH) that consists of a xenon lamp, a monochromator, a fiber optic probe, a CCD camera, and an imaging spectrograph. Together with a fast inverse Monte Carlo model of reflectance to quantify tissue absorption and scattering of tissues, we have applied this powerful toolbox in a variety of pre-clinical and clinical applications [49, 51, 52, 73].

Although this toolbox is capable of effectively quantifying tissue absorption and scattering [49, 51, 52, 80], like other diffuse reflectance spectrometers, the system has drawbacks in cost, collection efficiency, and clinical relevance and utility, which is of utmost importance to physicians and patients. First, the 1CH clinical system is a single-point sampling system in nature and is not ideal for applications where there is a need to cover large sampling areas, such as for tumor margin assessment. While single-point fiber-optic based detection is reasonable for a few and very small regions of interest [91, 99], it can be very cumbersome and expensive when expanded for use in quantitative spectral imaging. Furthermore, optical fibers generally collect only a small portion of the remitted signal, thus requiring the costly high quantum efficiency, ultra-low noise CCDs, particularly in the UV-VIS region. Thus, obviating the need for optical fibers in detection could potentially improve throughput.

In this chapter, I present the simple design and validation of a new probe to quantify absorption and scattering based on an inexpensive, robust silicon photodiode

integrated with a single illumination fiber coupled to a broadband source, similar to the hybrid system discussed in Chapter 2, but with improved performance. The probe was tested in liquid tissue phantoms, and optical properties were extracted with the inverse Monte Carlo reflectance model. The performance of the new probe was compared with that of the original 1CH fiber optics benchtop system. Wavelength reduction simulations were also performed to assess the feasibility of replacing the tunable light source with several miniature LEDs, further reducing the size, cost, and energy consumption of the benchtop system. In addition, a preliminary crosstalk analysis was done to show the potential for multiplexing the system into an imaging device, which could ultimately quantify tissue physiological and morphological properties over a large field of view.

(*It should be noted that at the time of the work presented in this chapter, our group had been developing and testing, in parallel, the 8CH fiber optics based clinical system in a breast tumor margin assessment study at Duke University Medical Center.*)

3.2 Materials and methods

3.2.1 System modification and probe geometry

In this iteration of system modification, the imaging spectrograph and CCD of the 1CH clinical system were replaced with a 5.8 x 5.8 mm silicone photodiode (S1227-66BR, Hamamatsu USA). To minimize the separation between illumination and

detection areas and to maximize the collection efficiency, a hole (D=1.3 mm) was drilled in the center of the photodiode. The careful drilling of the photodiode minimized damage and ensured similar detection performance. The only difference between the drilled and un-drilled photodiode was the total area of detection, which is 32.51 mm^2 for the drilled vs. 33.64 mm^2 for the un-drilled detector (the ratio of the areas is 0.97). The ratio of the signals detected by the drilled and un-drilled detectors when exposed to an incandescent bulb was 0.96, which is proportional to the loss in detection area of the un-drilled detector. An optical fiber (D=1 mm, NA=0.22) was fitted through the hole to illuminate the sample. Schematics of the system and probe tip are shown in Figure 12. This illumination and collection geometry is similar to that of the fiber optic probe geometry of the 1CH clinical system shown in Figure 6. The photodiode was connected to an amplifier (PDA-750, Terahertz Technologies Inc.) via a coaxial cable for reflectance measurements.

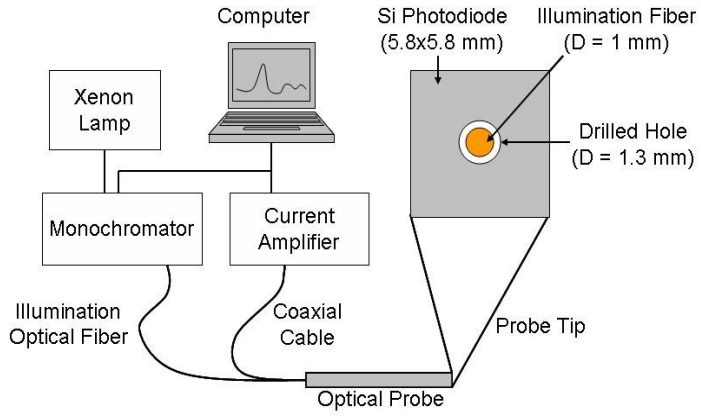

Figure 12: Schematic of modified diffuse reflectance system and probe tip.

3.2.2 Optical measurements of synthetic tissue phantoms

To assess the performance of the modified diffuse reflectance spectroscopy system for measuring tissue optical properties, a series of experiments were performed on homogeneous liquid phantoms with absorption and reduced scattering coefficients (μ_a and μ_s') similar to those of human breast tissue in the 400-600 nm wavelength range [100]. Water soluble hemoglobin (H0267, Sigma Co., St. Louis, MO) and 1-μm diameter polystyrene spheres (07310-15, Polysciences, Inc., Warrington, PA) were used as the absorber and scatterer, respectively. The phantoms were made in a 3.5 cm diameter container and filled up to a height of at least 4 cm. A spectrophotometer (Cary 300, Varian, Palo Alto, CA) was used to measure the wavelength-dependent absorption coefficients of the stock hemoglobin solution used to create the phantoms. Prahl's Mie scattering program was used to determine the reduced scattering coefficient [101].

Two sets of liquid phantoms were created and measured. The first set (S1) consisted of seven phantoms of different concentrations (3.7-34.9 μM) of the absorber and a fixed low number for scattering. The second set (S2) consisted of another seven phantoms of the same variable concentrations of Hb as S1, but with a fixed high number for scattering. The low and high scattering phantoms had a wavelength averaged μ_s' of 10-14 cm^{-1} and 16-23 cm^{-1} over 400-600 nm, respectively. A summary of the optical properties of the phantom sets are provided in Table 6.

Table 6: Average optical properties over 400-600 nm for 2 sets of phantoms (μ_a and μ_s' in cm^{-1}, Hb in μM)

Average Optical Properties over 400-600 nm					
	S1		S2		S1 & S2
Phantom	μ_a	μ_s'	μ_a	μ_s'	Hb (μM)
A	0.8	13.6	0.8	23.1	3.7
B	1.7	13.1	1.7	22.2	7.9
C	2.5	12.6	2.5	21.4	11.6
D	3.8	11.9	3.8	20.1	17.5
E	5.0	11.2	5.0	18.9	23.3
F	6.3	10.4	6.3	17.7	29.1
G	7.5	9.7	7.5	16.4	34.9

LabVIEW (National Instruments, Austin, TX) was used to control the monochromator, tuning the light source from 400-600 nm, and to digitally record diffuse reflectance measurements from the current amplifier. Prior to making optical measurements, the slit widths of the monochromator were optimized such that the output power from the illuminating fiber is maximized while the full-width at half-maximum (FWHM) of the lamp spectrum is 4.5 nm (to resolve the structure of the hemoglobin absorption bands). In the 400-600 nm range, the maximum power was 150 μW at 465 nm, and the minimum power was 50 μW at 600 nm. After a warm up time of 25 minutes, diffuse reflectance spectra were measured over the 400-600 nm wavelength range at increments of 5 nm. The measurements were repeated three times for each phantom to ensure good repeatability. The measurements were made with the room light off and the probe tip in contact with the surface of the liquid phantom. A

measurement was also taken from a Spectralon 99% diffuse reflectance standard (SRS-99-010, Labsphere, Inc., North Sutton, NH) with the probe tip in contact with the puck at the end of each phantom study. This spectrum was used to correct for the wavelength-dependent response of the system and throughput of the instrument. For the most absorbing phantom (S2-G) measured in these experiments, the calculated average signal to noise ratio (SNR) over all wavelengths was 60±10 dB, with a minimum SNR of 41 dB at 400 nm and a maximum SNR of 84 dB at 480 nm. SNR_λ is defined as $20*\log(I_{avg,\lambda} / \sigma_\lambda)$, where I is the intensity and σ is the standard deviation at the intensity, obtained from the three repeated measurements.

Using the inverse Monte Carlo reflectance model described in previous chapters [73], absorption and reduced scattering coefficients were extracted from the phantoms. To calibrate for system throughput and wavelength dependence, the experimentally measured and modeled spectra of the target phantom were normalized to that of a reference phantom with predefined optical properties at each wavelength. Phantom B in phantom set 2 (a low-absorbing phantom with $\mu_a = 1.7$ cm^{-1} and $\mu_s' = 22.2$ cm^{-1}) was used as the reference phantom to calibrate every other phantom as targets within each phantom set. The reference phantoms were chosen based on the suggestion proposed by a comprehensive study on the robustness of the inverse MC model in extracting a wide range of optical properties [84]. Bender et al. suggested using reference phantoms with mid to high reduced scattering coefficients (μ_s' = 15-25 cm^{-1} over 400-600 nm) and low to

mid absorption coefficients (μ_a = 0.5-2.5 cm^{-1} over 400-600 nm). Optical properties at each wavelength were extracted for each target phantom, and the inversion errors were averaged over all wavelengths and phantoms. The inversion errors were evaluated based on the following criteria. Extracted errors of less than 10% are considered excellent while errors of 10~20% are fair. Errors above 20% in phantoms are considered high and may or may not accurately extract physiological parameters in tissue.

3.2.3 Improvements to inverse Monte Carlo reflectance model

Because the model had only been set up to simulate circular sources and detectors, we modeled a circular detector with the active area equivalent to that of a square detector for the hybrid system described in Chapter 2. It was a rough estimation that could not easily be done in this iteration because we now had a circular illuminator in the center of a square detector with irregularly shaped edges due to the mechanical drilling.

In this study, the probe geometry of this system was modeled by taking a microscopic image of the probe tip and digitally tracing the illumination fiber and the photodiode edges. The image was converted to a binary image that clearly delineates the illumination and detection areas of the probe. Our scalable inverse Monte Carlo model was changed to able to account for very specific probe geometries by convolving the photon collection probability over each source-detector point on the probe.

One of the important parameters of probe geometry that the model takes into account is the NA of the illumination and detection fibers. Since the detection fiber has been replaced by a silicon photodiode, which has no nominal NA, we experimentally obtained the photodiode NA to feed into the MC model as the collection fiber NA. We collimated a laser diode to excite the active area of the photodiode, which is mounted on a rotation stage. With no ambient light in the room, we used the current amplifier to monitor the signal due to the laser while rotating the photodiode to determine the maximum acceptance angle. A measured acceptance angle of 75° in air gave us an NA of 0.965 for the photodiode.

3.2.4 Determination of probe sensing depth

One important aspect of the tumor margin assessment problem is the sensing depth of the probe. If the photons travel far beyond 2 mm and are also back-scattered and detected at the tissue surface, the device is not appropriate for margin assessment. Recall that during breast conserving surgery, the goal is to have a surrounding rim of normal tissue that is >2 mm. An intra-operative tool needs to correctly identify the positive and close (0-2 mm) tumor margins.

A range of probe sensing depths for the system were estimated using a weighted photon Monte Carlo light transport method developed by Quan Liu [102]. This modified Monte Carlo method employs the photon trajectory information generated from a single baseline Monte Carlo simulation of a homogeneous medium to scale the

exit distance and exit weight of photons for various given optical properties. The model records the visiting history, exit weight, and maximum depth of each photon that is detected at the surface. Although the probe geometry is unlike other fiber probes and is a square detector with an illuminator in the center, we are able to estimate the sensing depth with just half of the probe because the photon light path is the same for both halves of the probe. The simulated homogeneous medium had a thickness of 3 cm, radius of 3 cm, and was divided into grids of 0.01 cm (r), x 0.01 cm (z). Weighted visiting frequency as a function of depth was used to determine the theoretical sensing depth of the probe for the wavelengths of 450 and 600 nm. Visiting frequency is defined as the number of times a photon visits a grid divided by the total attenuation coefficient at that grid. To get the weighted visiting frequency, the visiting frequency was multiplied by the survival weight of the photon. Weight visiting frequency was further normalized by the peak and sensing depth was defined as the depth at which 90% of the photons visit before being collected by the detector.

3.2.5 Simulation of wavelength reduction

To further decrease the cost and size of our benchtop systems in the future, we investigated the potential of replacing the xenon lamp and monochromator by using several inexpensive LEDs in the 400-600 nm range. This feasibility study consisted of performing simulations of wavelength reduction on the measured liquid phantom data

obtained with our modified hybrid system. 5 commercially available LED wavelengths in the 400-600 nm spectral range were chosen: 405, 450, 470, 530, and 590 nm.

The key assumption in the simulation was that each wavelength has a bandwidth of 20 nm with a Gaussian distribution. This was an approximation made based on the commercially available LED specifications. The collected spectra from the phantom studies were processed such that data points from all wavelengths were excluded, except for those of the LED wavelengths enumerated previously. Each originally measured phantom spectrum, which consisted of 41 wavelengths over the 400-600 nm range in 5 nm increments, was first convolved with each of the 5 Gaussian-distributed LED emission spectra separately. This generated 5 individual new spectra. Then the new spectra were integrated over 100 nm, an arbitrarily large value that spans much wider than the LED bandwidth of 20 nm, to account for all potential signals from the LEDs. The integration was necessary because with a single photodiode, one can only measure the integrated intensity of the new spectrum. The resulting 5 intensities are the signals that would be measured using those specific LEDs. The final wavelength-reduced spectrum for each of the phantoms was composed of only these 5 data points. These newly generated LED spectra were used to extract optical properties.

3.2.6 Simulation of crosstalk

A primary goal in the later iterations of device design involves multiplexing the single-pixel hybrid device presented in this chapter into a quantitative spectral imaging

device for margin assessment. This can be done by arranging multiple optical fiber-photodiode pairs in a matrix formation. An important new parameter that must be characterized is the crosstalk. In an ideal situation, a fiber-photodiode pair is to be treated as a single pixel; however, the issue of a detector collecting stray light from an adjacent pixel, or even from multiple adjacent pixels, is unavoidable. High levels of crosstalk can significantly affect the measurement accuracy from tissue directly below the pixel.

To demonstrate feasibility of implementing a quantitative spectral imaging device, a Monte Carlo forward model of reflectance as described in the previous section was used to simulate a design where the nine Hamamatsu S1227-66BR photodiodes, each with 1.3 mm holes drilled in the center, were packed as closely together in a 3x3 matrix as shown in Figure 13. Each fiber is 1 mm in diameter and has an NA of 0.22. The silicon photodiode NA is 0.965. The separation of adjacent fibers is 8.48 mm. A forward model based on this geometry was used to generate the diffuse reflectance spectrum including both signal and cross-talk for each pixel. The simulated spectrum from each pixel was then inverted independently to determine the effect of cross-talk on the extracted optical properties.

The extracted errors due to the presence cross-talk were estimated by simulating phantom measurements with hemoglobin as the absorber and polystyrene spheres as the scatterer. Measurements were simulated for five phantoms with a wide range of

average absorption coefficients over 400-600 nm (μ_a = 0.4, 0.9, 1.3, 1.6, 2.0 cm^{-1}) and a fixed reduced scattering coefficient (μ_s' = 10). The inversion accuracy in the presence of crosstalk not only provides feasibility of creating such a device, but also useful information for future design parameters, such as fiber size, detector size, and pixel spacing.

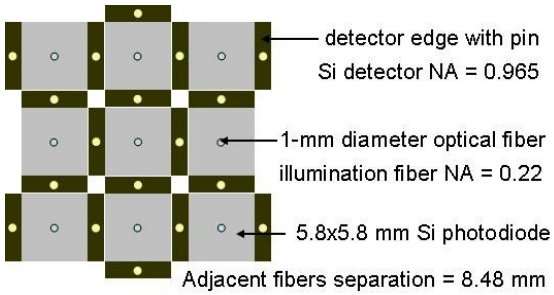

Figure 13: A 3x3 imaging array used for simulating crosstalk.

3.3 Results and discussion

3.3.1 Comparison of throughput-related parameters of benchtop system and modified system

The purpose of this study was to modify the 1CH benchtop system to decrease its size and cost of while still achieving comparable performance in extracting tissue optical properties. The modification of the 1CH benchtop system not only impacts size and cost but also the ability to seamlessly multiplex the device into a quantitative spectral imaging system. Comparisons of the throughput-related parameters and system characteristics of the benchtop and modified systems are presented in Table 7.

Table 7: Comparison of throughput-related parameters of original and modified systems

	1CH Benchtop System	Modified Hybrid System
Illumination Sources	Xenon lamp and Monochromator (Reflectance and Fluorescence)	Xenon lamp and Monochromator (Reflectance only)
Effective Illumination Diameter	1.00 mm	1.04 mm
Illumination NA	0.22	0.22
Detection Areas	2.26 mm^2	32.31 mm^2
Detection NA	0.22	0.96
Sensing depth (over 400-600 nm)	0.6 – 1.4 mm (μ_a = 0.5~2.5 cm^{-1}, μ_s' = 10~20 cm^{-1})	0.4 – 1.7 mm (μ_a = 0.5~2.5 cm^{-1}, μ_s' = 10~20 cm^{-1})
Detector QE	35% (400~600 nm) Min: 26% @ 450 nm Max: 45% @ 600 nm	73% (400~600 nm) Min: 62% @ 400 nm Max: 79% @ 600 nm
Dark Noise	6.4 x 10^{-7} pA	20 pA
Readout Noise	4.2 x 10^{-9} A	1 x 10^{-12} A
SNR (400~600 nm) (μ_a=7.5 cm^{-1}, μ_s'=16 cm^{-1})	Average: 45 ± 5 dB Min: 32 dB @ 405 nm Max: 60 dB @ 550 nm	Average: 60 ± 10 dB Min: 41 dB @ 400 nm Max: 84 dB @ 480 nm
Cost of Detection System	> $20,000	$1,000

Because the benchtop system is capable of also acquiring fluorescence information while the modified system can only be used for reflectance in its current

form, we recognize the inherent limitations of the side-by-side comparisons of various parameters of the benchtop and the modified system. In its current form, the modified hybrid system uses a monochromator to tune the light from the Xenon lamp from 400-600 nm, which is directly illuminated onto the sample. On the other hand, the 1CH benchtop system uses only white light to illuminate the sample, and the collected light is then split by the spectrograph. The monochromator was used in this particular instance because it was readily available. Because the monochromator is relatively slow in scanning a range of wavelengths, taking over a minute for a measurement, a filter wheel can be implemented in the place of the monochromator to speed up data acquisition if the next iteration of system design requires a tunable source.

Since the effective illumination diameter and source detector separation are similar for both systems, the sensing depth is also similar over the same range of wavelengths for a given set of optical properties. Monte Carlo simulations were performed to assess sensing depth for both probes over 400-600 nm for the optical properties, μ_a = 0.5-2.5 cm^{-1} and μ_s' = 10-20 cm^{-1}. The sensing depth is defined as the depth at which 90% of the probable visited photons in the sample will exit and reach the detector to be collected. The modified system has a slightly deeper sensing depth because the detection area is bigger and can collect photons that have traveled deeper into the medium although these exit photons farther away from the illumination fiber have much less weight than those that are closer to the illumination fiber. The sensing

depth can be easily changed by adjusting various source-detector separations and is an important parameter to consider in future probe designs, depending on the clinical application for which the technology will be used.

While some parameters, such as sensing depth and effective illumination area, are comparable for both systems, the modified hybrid system has several parameters that are superior to those of the 1CH benchtop system, which ultimately translate to high signal-to-noise (SNR), and lower cost. Based on the commercial specification sheets, the CCD of the benchtop system has an average quantum efficiency of 35% from 400-600 nm. On the other hand, the photodiode in the modified system has an average quantum efficiency of 73% in the same range. Furthermore, the detector is directly in contact with the sample in the modified design, collecting most of the remitted light, whereas the detector of the benchtop system is at the distal end of the collection fiber bundle where significant light is inherently lost. The average SNR in a dark, highly absorbing phantom (μ_a = 7.5 cm^{-1} and μ_s' = 16 cm^{-1}) measured using benchtop system is 45±5 dB over 400-600 nm, which is lower than the 60±10 dB measured with the modified system. In addition, the cost of the detection portion of the modified system is significantly cheaper compared to its benchtop counterpart.

3.3.2 Extraction accuracy in liquid phantoms

Monte Carlo inversions were performed to extract optical properties on both sets of phantoms. Figure 14 shows the extraction performance using the modified system

alongside the original benchtop system. For the modified system, the correlation coefficients for expected and extracted μ_a and μ_s' are 0.9992 and 0.9478, respectively. Using phantom S2-B (μ_a = 1.7 cm^{-1} and μ_s' = 22.2 cm^{-1}) as the reference, the overall extracted μ_a error was 9.8±5.0%, and the overall μ_s' error was 7.6±4.2%. For this similarly wide range of optical properties and using a similar reference phantom (μ_a=1.4 cm^{-1}, μ_s'=19.3 cm^{-1}), the original benchtop system had overall errors of 9.8±8.2% and 7.7±6.3% for μ_a and μ_s', respectively. All percent error values given are mean RMS percent errors averaged across all wavelengths for all target phantoms for the extraction of optical properties. The modified system and the benchtop system seem to have very comparable performance in extracting optical properties in tissue phantoms over a wide range of optical properties. Compared to the previous version of the single-point hybrid system described in Chapter 2, this system is capable of extracting optical properties in a more clinically relevant range.

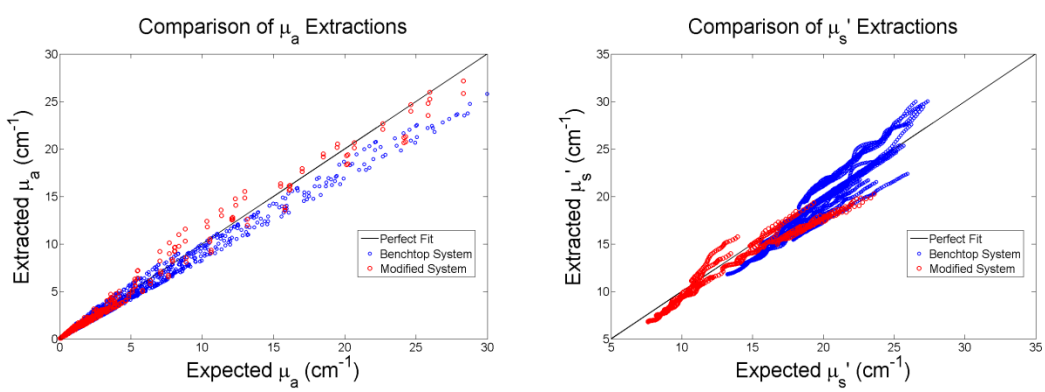

Figure 14: Comparison of absorption and scattering extractions by the 1CH clinical system and the modified hybrid systems.

3.3.3 Feasibility of wavelength reduction

Figure 15 shows the measured reflectance spectra of the lowest and highest absorbing phantoms for all wavelengths and the generated data points from the wavelength reduction simulation used for additional MC inversions, both calibrated by the puck spectrum. It is important to note that the simulated wavelength-reduced spectra are composed on only 5 data points each. These 5 data points are the signal that would be read by the photodiode current amplifier.

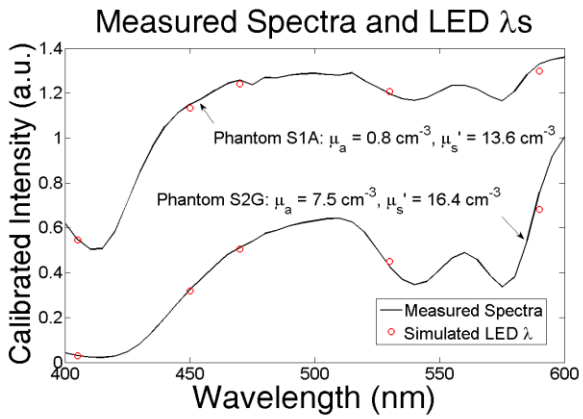

Figure 15: Experimental reflectance spectra from the least absorbing and the most absorbing phantoms with the 5 wavelengths chosen for MC inversions.

Figure 16 illustrates the theoretical extraction performance of the modified system after wavelength reduction simulations. For the same large range of optical properties and using the same reference phantom as before (S1-B: μ_a = 1.7 cm^{-1} and μ_s' =

22.2 cm^{-1}), the overall μ_a extraction error was 9.6±5.8%, and the overall μ_s' error was 14.3±7.3%. The correlation coefficients for expected and extracted μ_a and μ_s' are 0.9972 and 0.8628, respectively, in the inversion of wavelength-reduced phantom data. The increase in the extraction errors can be attributed to not only the reduction of wavelengths, but also the loss of spectral information with a wider FWHM (20 nm) of the simulated wavelength reduction.

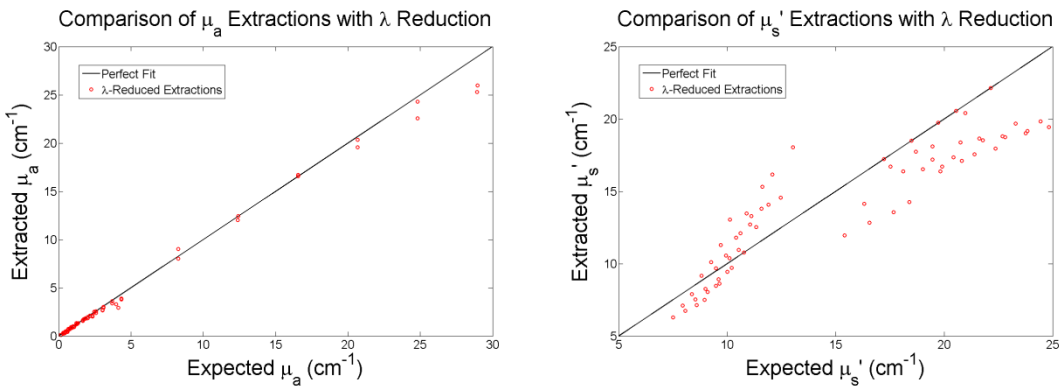

Figure 16: Extractions of absorption and reduced scattering coefficients after wavelength reduction simulation.

Using only 5 wavelengths from the collected phantom data to perform the Monte Carlo inversion, the hemoglobin spectra can be reconstructed with the extracted absorption coefficients and the molar extinction coefficient for hemoglobin measured with the spectrophotometer on the day of the phantom study. Figure 17(a) shows the reconstructed hemoglobin spectra averaged over all phantoms. Figure 17(b) shows

relatively good extraction accuracy for hemoglobin concentrations for all phantoms. There is a slight underestimation of hemoglobin at very high concentrations, which is consistent with previous studies using the 1CH benchtop system [84].

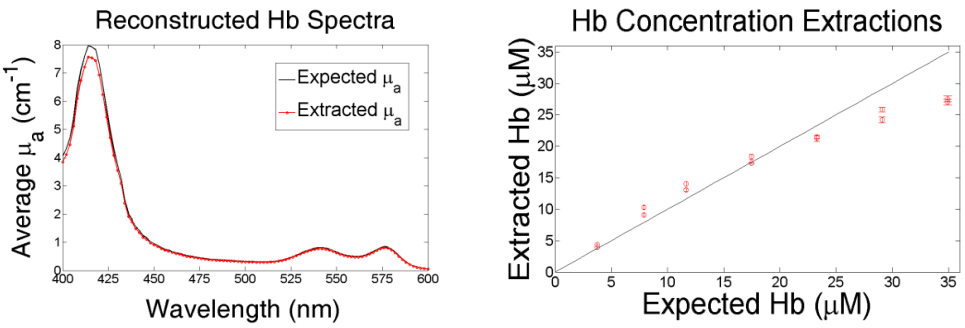

Figure 17: Reconstructed Hb spectra averaged over all phantoms using extracted absorption values at the 5 chosen wavelengths; (b) extractions of Hb concentration by inverting wavelength-reduced spectra

These wavelength reduction results show the feasibility of replacing the Xenon Arc lamp and the monochromator in our modified system with just 5 LEDs in the next generation of system design. Not only is there an abundance of high-powered LEDs in the 400-600 nm range, these potential light sources are also very inexpensive. Furthermore, the use of LEDs can potentially obviate the need for optical fibers and is well-suited for miniaturized optical spectral imaging systems. With LEDs as the illumination source and tiny photodiodes as the detector, the device would then be truly miniaturized compared to the current benchtop system while still achieving comparable performance in the extraction of optical properties in tissue. It is reasonable to believe

that an LED-photodiode device would have not only the benefits of having the superior collection efficiency of the detector, but also higher throughput with high-powered LEDs. In addition to LEDs as an alternative source, a combination of a lamp and a series of band-pass filters may also be implemented. The use of band-pass filters in conjunction with an optical fiber can also provide high throughput similar to LEDs and is relatively simple to integrate into the existing benchtop system. However, the down side of using the latter approach is the increased cost and size of a lamp-filter wheel based system. The enumerated errors of the extraction of optical properties shown in Table 8 indicate that it is unnecessary to use the full 400-600 spectrum to extract optical properties with good accuracy.

Table 8: A table of comparison for the original benchtop system and modified system with its wavelength-reduced inversion errors, averaged for all reference-target phantom combinations.

Summary of Optical Properties and Inversion Errors					
(400-600 nm)	Avg μ_a range	Avg μ_s' range	Hb range	μ_a error	μ_s' error
1CH Clinical	0.2~8.2 cm^{-1}	16.9~24.1 cm^{-1}	1.0~35.2 μM	9.8±8.2%	7.7±6.3%
Modified Hybrid	0.8~7.5 cm^{-1}	9.7~23.1 cm^{-1}	3.7~34.9 μM	9.8±5.0%	7.6±4.2%
λ-Reduced	0.8~7.5 cm^{-1}	9.7~23.1 cm^{-1}	3.7~34.9 μM	9.6±5.8%	14.3±7.3%

We recognize the importance of wavelength choice when the system is to be used in clinical situations in the future. The phantoms presented in this study are very simplified compared to the composition of real human breast tissue. However, we

know from numerous studies that hemoglobin is the dominant absorber in tissue. We can extract its concentration with good accuracy with a few wavelengths. The current wavelength choices presented in this study sufficiently encompass the distinct features of hemoglobin: the Soret, α-, and β-bands. Oxy- and deoxy-hemoglobin and thus hemoglobin saturation can be extracted because of the clear shifts in spectral peaks. These are important parameters to delineate normal from malignant tissues, which is an important goal. Other physiological parameters may also be quantified using just a few wavelengths, analogous to other systems currently in clinical studies, such as those using frequency domain photon-migration techniques [103]. If more than 5 wavelengths are needed to accurately extract other important physiological parameters, a system with a lamp and filter wheel can be designed to accommodate as many as 10 wavelengths. The addition of a few extra LEDs can also be implemented. More details about the wavelength optimization and validation of wavelength selection will be discussed in Chapter 5.

3.3.4 Analysis of simulated crosstalk

Crosstalk was simulated as a preliminary effort to create an imaging device. We hypothesized that the center pixel in the 3x3 matrix, shown previously in Figure 13, would receive the most amount of crosstalk and thus is presented as the worst case scenario. As expected, the inversion showed that center detector had the worst

extraction errors for μ_a and μ_s'. Table 9 enumerates the inversion errors in the presence of crosstalk at the center, the side, and the corner detectors, respectively.

Table 9: μ_a and μ_s' extraction errors (%) for each detector in the presence of crosstalk in phantoms ranging from low to high absorption coefficients (μ_a = 0.4 - 2.0 cm^{-1}) and mid reduced scattering coefficients (μ_s' = 10 cm^{-1}), averaged for all reference-target phantom combinations.

Inversion errors with crosstalk						
	Center Detector		Side Detectors		Corner Detectors	
Phantoms	μ_a error	μ_s' error	μ_a error	μ_s' error	μ_a error	μ_s' error
A	2.2	7.8	1.6	5.7	1.0	2.9
B	2.2	5.1	1.6	3.6	0.9	1.8
C	2.4	5.0	1.6	3.3	0.9	1.8
D	3.6	6.5	1.8	3.8	1.3	2.3
E	4.3	8.1	2.4	4.8	1.7	3.1

The errors were averaged over all reference-target phantom combinations. With μ_a and μ_s' extraction errors of less than 2% and 5%, respectively, the simulation shows that crosstalk has little effect on the side and corner detectors. The center detector received the most crosstalk, and its extraction errors are nearly doubled compared to those of the non-center detectors. Simulation shows that the overall errors due to crosstalk are relatively small and that constructing an imaging device will be feasible based on this particular geometry. Other factors that could reduce crosstalk errors in the multi-pixel device prototype are fiber size, detector size, and detector spacing. It is important to note that crosstalk was only generated to evaluate its effect on inversion errors in this study. It should also be noted that crosstalk was not taken into account by

our current Monte Carlo model. Work is currently being done on creating a fast multi-region Monte Carlo model that is capable of including the effects of cross-talk.

The 3x3 matrix simulated in this study was strategically created partially based on the probability of exiting photons hitting adjacent detectors being very small. The drawback of this design is that the detectors themselves as well as the pixel spacing have to be large. While such a device is able to show a proof of concept in creating an imaging device, it may not be useful clinically to have a matrix of large detectors spaced far apart from each other. Once crosstalk is modeled effectively, the imaging prototype can be designed with smaller detectors and pixel spacing with better resolution for clinical applications.

3.3 Conclusions

This multi-faceted study shows that the modified system along with our Monte Carlo model can be miniaturized and extended into an optical spectral imaging system. In its current, single-pixel state, the system is capable of extracting optical properties in tissue phantoms with good accuracy in the 400-600 nm range comparable to the clinical benchtop system. By placing the detector directly in contact with the sample, the collection efficiency is improved. Furthermore, the results from the wavelength reduction simulations from the measured phantom data show great potential in replacing the lamp and monochromator with several high powered LEDs in the 400-600

nm range for higher throughput, smaller size, and much lower cost. By strategically choosing high powered LEDs with a 20-30 nm bandwidth while covering most of the 400-600 nm range, an LED-photodiode device can be created and used to extract a similar range of tissue optical properties within a well-defined sensing depth. The new semiconductor device would not only undoubtedly have higher throughput than the lamp-monochromator model, but also be truly miniaturized and made at a fraction of the cost of the original system. Lastly, the crosstalk analysis shows the potential for either the fiber-photodiode system or the miniaturized LED-photodiode system to be multiplexed into an imaging device. With a low probability of exiting photons reaching adjacent detectors, the effect of crosstalk on inversion accuracy is low for a matrix of 5.8x5.8 mm silicon photodiodes. By accurately accounting for crosstalk with our Monte Carlo model, an imaging prototype can be made with much smaller detectors spaced closer to one another. The use of smaller, more sensitive detectors along with sources with superior throughput would ultimately result in a system with high clinical utility.

The eventual goal of creating a miniaturized spectral imaging device based on inexpensive photodiodes and LEDs can have a remarkable impact in not only basic biomedical research, but also in clinical situations worldwide. While a single-pixel probe is certainly useful for small regions of tissue, the information that can be unraveled by an imaging device is unmatched for larger samples, such as those in tumor margin assessment, assessing tumor response to therapy, epithelial pre-cancer and

cancer detection, among other applications. A miniaturized imaging device based on the LED-photodiode design would be able to spectrally map out quantitative biological information for tissue composition just below the surface. Furthermore, the device would be portable and inexpensive, allowing it to be accessible for not only the standard research laboratory or clinic, but also potentially for use in rural clinics in the developing world.

4. Modification of illumination components and multiplexing for spectral imaging

In Chapters 2 and 3, two hybrid fiber-illumination and PD-detection single-pixel diffuse reflectance spectroscopy systems with different probe geometries were built and characterized to show the feasibility of replacing the CCD and imaging spectrograph in the single-point and 8-channel clinical benchtop systems (1CH and 8CH) to quantify tissue optical properties. This chapter presents the additional modification of the light source of the benchtop clinical systems and the multiplexing of the individual PDs into an imaging array.

4.1 Introduction

As shown previously, we have leveraged the underlying sources of contrast using diffuse reflectance spectroscopy in the visible wavelength range for the detection of breast malignancies. We first showed proof of principle by testing a single-channel (1CH) benchtop system and conducted clinical studies to show its capability of differentiating between normal and malignant breast tissues. To cover the area of a large tumor margin and to make a DRS system more practical for clinical use, we multiplexed the single-channel probe in to an 8-channel probe while keeping all other components essentially the same.

4.1.1 DRS instrumentation – 8CH clinical system

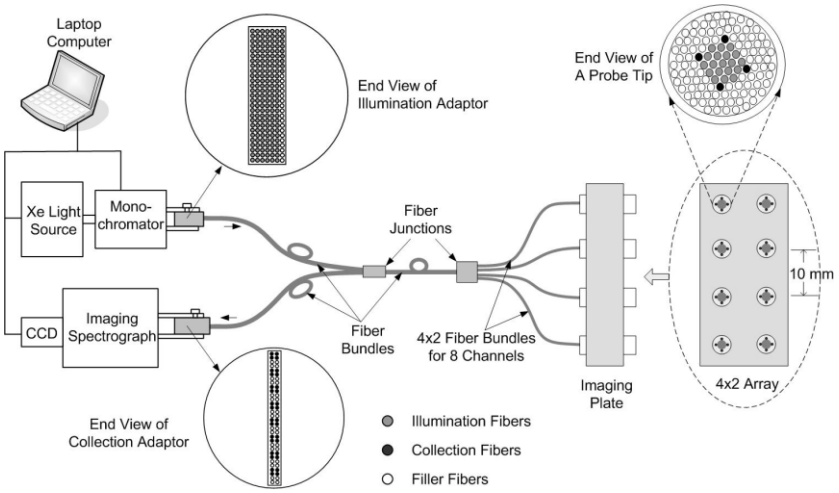

Figure 18: System schematic of the clinical instrument and the fiber arrangement of the multi-channel probe.

The system schematic of the 8CH clinical instrument is shown in Figure 18. [104]. It consists of a 450W Xenon arc lamp coupled to a monochromator (Gemini 180, JY Horiba) set for zero-order diffraction, a custom-built 8-channel fiber optic imaging probe (RoMack, Inc.), an imaging spectrograph (iHR 320, JY Horiba), and a cooled CCD camera (Synapse, JY Horiba). Each channel of the imaging probe has a core of nineteen 200-μm illumination fibers (NA=0.22) surrounded by four 200-μm collection fibers (NA=0.22) with source-detector separations spanning 0.23-1.10 mm. The typical power output at the probe tips is 3 μW at 450 nm and 25 μW at 600 nm within a 10 nm bandpass. The configuration of the fiber geometry of each channel was designed so that

the optical sensing depth is appropriate for tumor margin assessment. Recall from previous discussion that in BCS, the surgeon is attempting to resect a tumor with a surrounding margin of greater than 2 mm of normal tissue while trying to conserve as much normal tissue as possible. It is also important to identify close margins between 0-2 mm. Therefore, the sensing depth of each channels needs to be approximately 0-2 mm. Using a weighted photon tracking Monte Carlo reflectance model [102] to simulate photon paths in typical normal and malignant breast tissues, we designed each channel of this imaging probe to have a sensing depth of 0.5-2.2 mm for 450-600 nm. The 8 channels are arranged in a 4x2 array with a 10-mm spacing (center to center) between each channel.

Broadband light from the Xenon arc lamp is launched via illumination fibers of each channel of the imaging probe into each discrete tissue site on the tumor margin. The scattered photons in tissue for each discrete site are remitted and collected by fibers of each channel. With a single placement of the imaging probe, eight discrete sites are imaged on the tumor margin. The imaging spectrograph and CCD convert the remitted photons to spectrally resolve diffuse reflectance spectra for each site. The spectra are then analyzed with inverse Monte Carlo model of reflectance presented in the previous chapters [49, 73]. The system showed promise as an intra-operative tool, but can be improved in footprint, speed, resolution, and coverage.

4.1.2 Multiplexing with optical fibers into imaging array

To address the issue of footprint and cost of the 8CH clinical system, we expanded the photodiode detection concept and developed a compact and low cost system (9PD) using a broadband light source with an 8-slot filter wheel for illumination and commercial silicon photodiodes arranged in a 3x3 array for detection.

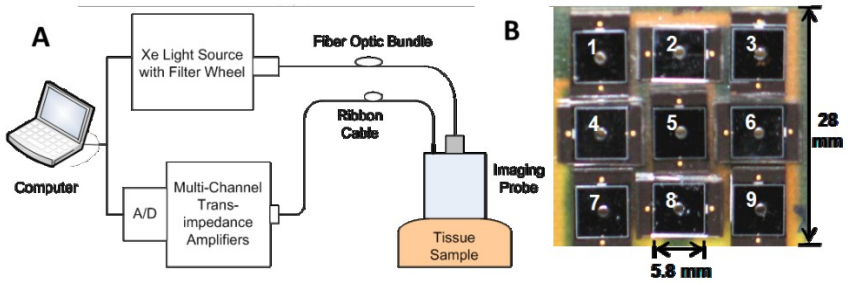

Figure 19: (a) System schematic of the compact optical spectral imaging system which details the illumination and collection setup and (b) photograph of the 3x3 photodiode array with central apertures mechanically drilled for each optical fiber.

Figure 22(a) shows the system schematic of the hybrid spectral imaging system that utilizes both fiber illumination and photodiode detection. Briefly, this design involved replacing the spectrograph in the 8CH clinical system with a simple 8-slot filter wheel on the illumination end. Instead of a 2D CCD, silicon photodiodes were used for detection by multiplexing the previous single-pixel design (described in Chapter 3) into a 9 pixel 3x3 matrix. The light source for this system is a broadband 350W xenon arc lamp (MAX-302, Asahi Spectra). Light from the xenon arc lamp passes through one of

eight bandpass filters with 10 nm FWHM selected using an 8-slot filter wheel. The resulting monochromatic light is launched into a bundle of 9 optical fibers, each 0.6 mm in diameter (FVP600660710, Polymicro), which deliver the light to the tissue through the centered aperture of each of the nine 5.8 x 5.8 mm silicon photodiodes (S1227-66BR, Hamamatsu) at the distal end of the imaging probe shown in Figure 22(b).

The spectral imaging system was tested on a set of tissue mimicking liquid phantoms and yielded an optical property extraction accuracy of accuracy of 6.40±7.78% for the absorption coefficient and 11.37±19.62% for the wavelength-averaged reduced scattering coefficient [105]. For the first time, we show the ability to extract optical properties with good accuracy utilizing photodiodes and only 8 discrete, semi-evenly spaced wavelengths (400, 420, 440, 470, 500, 530, 570, and 600 nm), which potentially moves us closer to the realization of a compact spectral imaging system based on LEDs for illumination and photodiodes for detection. In previous iterations, we had collected some combination of wavelengths in 2.5 nm increments or 5 nm increments between 400-600 nm and 450-600 nm to use in the inverse Monte Carlo reflectance model. In simplified liquid phantoms, we were able to show that it is feasible to reduce the number of wavelengths from 81 or 61 down to just 8 for quantifying optical properties.

4.1.3 Limitations of using optical fibers

Although the 8CH clinical system has shown potential to be an intra-operative breast tumor margin assessment tool, capable of diagnosing margin status with a

sensitivity of 79.4% and a speficity of 66.7% [72], it is not easily scalable to cover larger areas with sufficient spatial resolution in the limited amount of time allowed in the operating room. In that particular design, the surveillance area per probe placement is limited by number of collection channels (fiber bundles) that can be imaged onto the CCD, or essentially by the CCD chip size.

In Section 4.1.2, We showed that we can potentially hurdle this technical problem by utilizing discrete photodiodes placed at the surface of the sample because photodiodes are more much easily scalable to larger arrays and very inexpensive compared to CCD cameras. However, in the process of building this system, we found that coupling optical fibers from the broadband source and bandpass filters to efficiently guide the light into the central photodiode apertures can also be a tedious, imperfect process. Because an important part of our DRS imaging toolbox is the inverse Monte Carlo reflectance model and the proper modeling of probe geometry, it was impractical to continue fitting fibers through mechanically drilled detector apertures as this method results in a different probe geometry for every single channel. Furthermore, we found that these thick optical fibers epoxied to photodiodes are not robust enough to withstand the clinical environment. Once epoxied to the photodiode apertures, we are no longer able to polish the fiber tips if it ever becomes damaged. We took a stepwise iteration approach by changing one component at a time throughout this dissertation. This chapter describes the next system design iteration in which we eliminate the

illumination fibers in a 4x4 custom photodiode array and test the system in phantoms, animals, and human tissue.

4.2 Methods

4.2.1 System components

As described in previous publications on the system design, this design iteration of the diffuse reflectance spectral imaging system included a 350W xenon arc lamp (MAX-302, Asahi Spectra) with an 8-slot filter wheel, which had bandpass filters with center wavelengths at 400, 420, 440, 470, 500, 530, 570, and 600 nm, each having a 10-nm FWHM (XBPA, Asahi Spectra) [105, 106]. An optical light guide with a numerical aperture (NA) of 0.57 was used to divergently illuminate the backside of a custom annular photodiode array, through the apertures of each photodiode, and onto the tissue sample. Fabricated in-house at the Shared Materials Instrumentation Facility at Duke University through collaborations with Nan Jokerst, the detector array consisted of sixteen annular silicon *pn* junction photodiodes, which were used to detect diffuse reflectance from the tissue sample. For each photodiode, the outer and inner diameters were 2.5 and 0.75 mm, respectively, and the center-to-center distance of the diodes was 4.5 mm. The total coverage was 3.8 cm^2. The fabrication process and initial testing of the photodiode array were explained in detail by Sulochana Dhar et al. in a previous report [107]. The diffuse reflectance photocurrent was measured for all 16 photodiodes by an

eight-channel source-measure unit (Keithley SMU-4200) with an added mechanical switch.

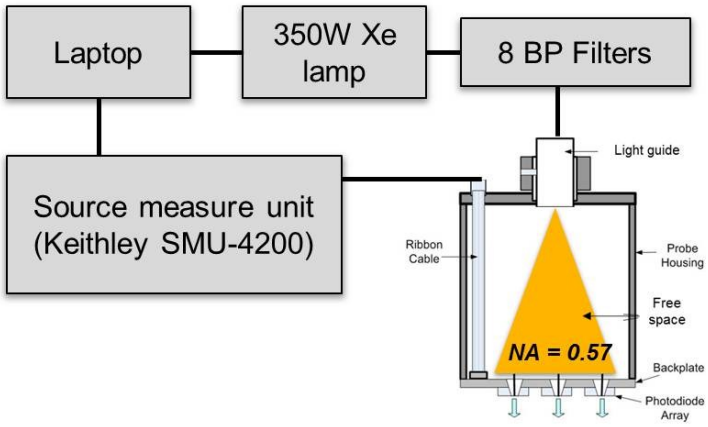

Figure 20: General schematic of wide field spectral imaging system prototype, detailing the free-space illumination strategy through detector apertures.

The incorporation of the custom annular photodiode array in this work was an improvement from our previous proof-of-concept work, which utilized commercially available photodiodes (S1227-33BR, Hamamatsu). The annular photodiodes had customized geometry for appropriate sensing depth for the application of breast tumor margin assessment, and the array spacing was designed to minimize optical cross-talk. The fabricated photodiodes were also thinner and unpackaged at 610 microns compared to the S1227-33BR diodes (2.1 mm) and provided better uniformity for modeling of probe geometries as well as higher throughput and SNR than the previous design. Most importantly for our clinical application, the custom array offered higher spatial

resolution than the previously reported systems [71, 106]. A general schematic of this simple design is shown in Figure 20.

4.2.2 System validation in liquid phantoms

To assess the performance of the spectral imaging system, we created 10 liquid phantoms, which consisted of human methemoglobin (M7516, Sigma Co.) and 1-micron polystyrene spheres (07310-15, Polysciences, Inc.), and spanned a range of optical properties similar to those of breast tissue (μ_a = 3.9–10.8 cm^{-1}, μ_s' = 6.5–9.5 cm^{-1}, averaged over 400-600 nm). For each phantom, 20 scans of diffuse reflectance measurements were recorded and averaged at each of the 8 wavelengths. The diffuse reflectance spectra were corrected for the wavelength-dependent system response and the day-to-day variation of the instrument by normalizing to a Spectralon 99% reflectance standard (SRS-99-010, Labsphere, Inc.). Palmer's fast, scalable inverse Monte Carlo model of reflectance was used to extract the absorption and reduced scattering coefficients [73].

4.2.3 Optical measurements in a murine tumor model

A murine tumor model was used to determine whether the system had sufficient signal in a biological sample and to compare the extracted tissue constituents with those extracted using another well-tested, research-grade system. 3 mice were injected with 4T1 murine mammary tumor cells in the left flank. The tumors were grown for 2 weeks to 200 mm^3 in volume. Diffuse reflectance measurements were collected from the tumor on the left flank as well as the normal tissue on the right flank. 20 repeated

measurements were made at each wavelength for each site. Because the size of the 4x4 photodiode imaging array is larger than the size of the murine tumor, only the central 4 pixels were evaluated for reflectance measurements. Additional diffuse reflectance measurements were made with another commercial spectrofluorometer (SkinSkan, JY Horiba) on both the normal and tumor flanks. The commercial spectrofluorometer consisted of a broadband source and PMT with a single-channel, fiber-optic probe.

The inverse Monte Carlo model of reflectance was used to extract the absorption and reduced scattering coefficients from the animal measurements. Because the 4T1 murine tumor cells are grown homogeneously relative to human breast tissues, which are very heterogeneous, we compared the extracted parameters of tumor and normal sites using the wide-field spectral imaging system and the single-channel spectrofluorometer without any co-registration of measurements.

4.2.4 Initial human breast tissue study

An *ex-vivo* clinical study using diffuse reflectance spectral imaging to evaluate lumpectomy specimens in patients undergoing surgery for breast tumors was approved by the IRB at Duke University. The surgeon removed the lumpectomy specimen, and clips and sutures were placed to orient the specimen for pathological assessment. The optical study was performed after the excision and thus did not change the standard operating procedures. In this initial case, we collected diffuse reflectance from only one margin to assess the SNR of the system in human tissue. 10 reflectance measurements

were made for each wavelength, and the study was limited to the typical 15 minutes in the operating room so that the patient did not have to remain under general anesthesia for longer than the standard surgical time.

After data collection, the inverse Monte Carlo model of reflectance was used to extract absorption and reduced scattering coefficients. Hemoglobin concentrations and β-carotene concentrations for each site were calculated from the molar extinction coefficients of the chromophores. We then checked the values of the extracted hemoglobin and β-carotene concentrations with those extracted in our previous study to see whether or not the numbers are reasonable for breast tissue.

4.3 Results and discussion

4.3.1 System throughput and SNR

With the divergent light guide illuminating the backside of the annular photodiodes, we expected the throughput to be relatively non-uniform. However, because each channel is read separately, we hypothesized that if the SNR is sufficiently high (>40 dB) in breast tissue, the corner channels with lower throughput can still be used to extract tissue parameters [108, 109]. Figure 21 shows the power measured at 440 nm through the 0.75 mm diameter apertures of each photodiode on the imaging array. The channel numbers are also labeled for referencing the remainder of this chapter.

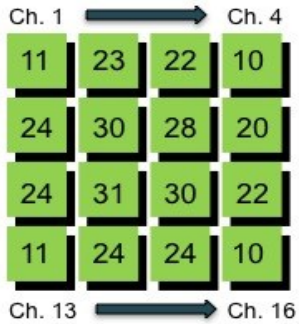

Figure 21: Power (μW) at 440 nm measured through aperture of each PD on imaging array; channel numbering (1-16) are also noted from left to right and top to bottom referred in this chapter.

We calculated the system SNR of each wavelength from each channel in the liquid phantom study, the mouse study, and the lumpectomy study. SNR_λ was defined as $20*\log(I_{avg,\lambda} / \sigma_\lambda)$, where I is the intensity (or photocurrent generated by collected diffuse reflectance) and σ is the standard deviation of the intensity obtained for 10 repeated measures. During the liquid phantom study, we found some significant drifting of reflectance signal in channels 3, 10, 12, and 14. We investigated the cause of this drift and hypothesize that the epoxy used to insulate the conductive interconnections on the circuit board cracked over time and liquid from the phantoms entering these fissures affected our measurements. This also affected our SNR measurements in phantoms, which ranged from as low as 20 dB at 400 nm for a channel that exhibited drift when exposed to liquids, to as high as 55 dB at 600 nm for a channel without drift. For the channels that did not drift, the SNR typically ranged from 40-50 dB.

In the animal study, the measurements were made on solid tumors on the left flank and the normal right flank. Since there were no liquids affecting the measurements, none of the channels exhibited signal drift, and the SNR ranged from 39-53 dB for all channels and all wavelengths. Similarly, measurements in the lumpectomy specimen were also consistent for all channels. We found the SNR to be lowest at 400 and 420 nm and highest at the longer wavelengths, 570 and 600 nm. Figure 22 shows the averaged SNR of all 16 channels for all 8 wavelengths. Based on previous systems used in various studies in the human breast, head-and-neck, and cervix, we had a target SNR of ~40 dB. This shows that despite the non-uniform illumination and throughput of each channel, we are able to achieve sufficient SNR for clinical applications.

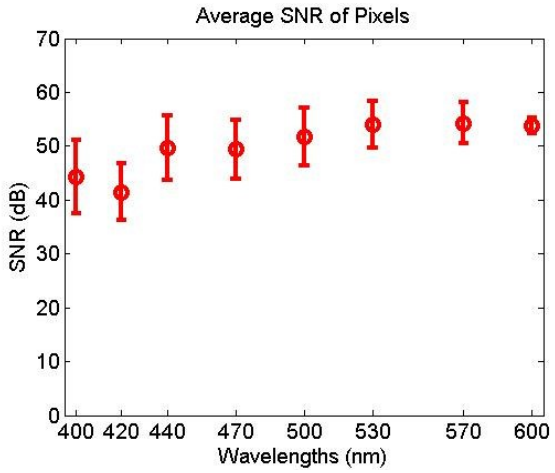

Figure 22: SNR measured from human breast as a function of the 8 wavelengths, averaged for each channel on the 4x4 imaging array.

4.3.2 Extraction of phantom optical properties

Absorption and reduced scattering coefficients for all 10 liquid phantoms were extracted for each of the 16 channels using the inverse Monte Carlo model of reflectance. Table 10 shows the averaged RMS errors (%) for the each channel. The RMS errors were averaged for all 10 liquid phantoms, and the standard deviations are also shown. The channels that had significant drift in reflectance signal due to liquid contact are highlighted and discarded as unreliable channels for this work. Figure 23 shows the extraction accuracy for absorption and reduced scattering coefficients for the remaining 12 channels. For each channel, the errors for extracted absorption and reduced scattering coefficients were 8-15%. With the ability to extract optical properties with low errors, we can then use these as reference phantoms to extract optical properties from animal and human tissues with unknown optical properties.

Table 10: Extracted absorption and reduced scattering coefficients RMS errors averaged over 10 tissue-mimicking liquid phantoms.

Ch	1	2	3	4	5	6	7	8	9	10	11	12	13	14	15	16
μ_a	8±11	8±9	24±9	12±6	9±5	12±5	12±9	14±9	15±4	27±9	12±8	50±31	13±8	28±11	12±7	14±7
μ_s'	11±7	8±5	23±11	11±4	9±2	8±5	8±3	14±8	14±9	13±7	15±3	38±23	15±7	16±8	14±5	11±4

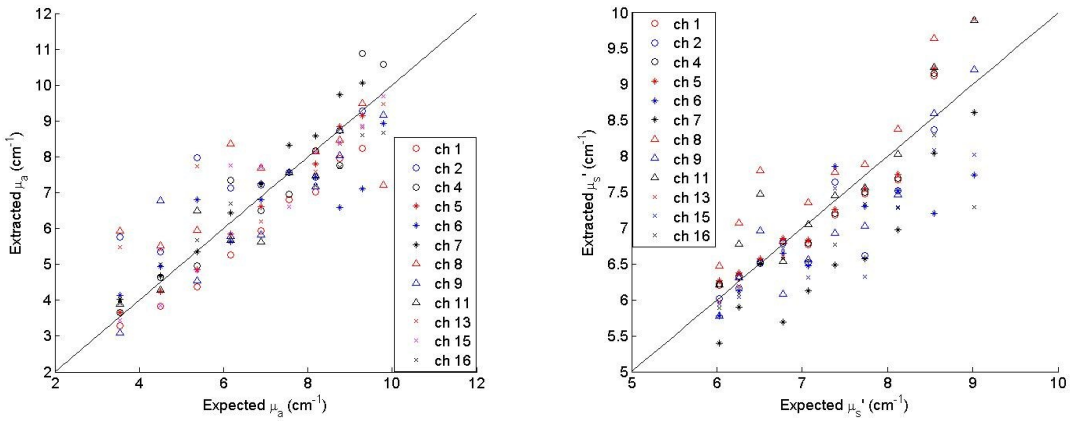

Figure 23: Absorption and reduced scattering coefficients extracted using inverse Monte Carlo model of reflectance. Channels with draft due to liquid contact on exposed tracks on circuit board during measurement are discarded.

4.3.3 Extraction of tissue parameters in murine tumor model

The goal of the mouse study was to determine whether the imaging system had sufficient SNR in a biological sample and to compare the extracted tissue parameters with that of another well-characterized commercial instrument [84]. Diffuse reflectance measurements were collected from the tumor and normal flanks for all 3 mice using both the spectral imaging system and the spectrofluorometer, SkinSkan from JY Horiba. Because the tumor size on the left flank was smaller than the 3.8 cm^2 coverage of the imaging array, only the 4 center channels (6, 7, 9, and 10) are used to measure the tumors. Unfortunately, channel 10 had significant drift in the liquid phantom study, and without a reliable reference phantom for Monte Carlo inversions, it was also discarded in data analysis. With measured reflectance from channels 6, 7, and 9 from the spectral imaging system and from the commercial spectrofluorometer, the inverse

Monte Carlo model was used to extract the total hemoglobin concentrations and reduced scattering coefficients. Table 11 shows the extracted results from the normal and tumor flanks for both systems.

Interestingly, even without co-registration of the exact measured sites, the extracted parameters using both systems are within 10% of each other. This gives us great confidence that these 3 channels on the system can be accurate in extracting tissue parameters and, with further optimization, we can use this system for quantitative tissue spectral imaging. While there was not enough statistical power to claim significance with only 3 mice, we did notice an interesting trend in a decrease of total hemoglobin content and reduced scattering coefficients in the tumor measurements. At the time of measurement, these fast-growing tumors had already exhibited signs of becoming necrotic, which explain the decrease in total hemoglobin content.

Table 11: Extracted total hemoglobin content and averaged reduced scattering coefficient for normal and tumor flanks measured by the commercial spectrofluorometer (SkinSkan) and the PD-based spectral imaging system with averaged values for channels 6, 7, and 9.

Mouse	**SkinSkan, JY Horiba (1-ch)**				**PD SPX Imaging System (Avg values)**			
	Normal		*Tumor*		*Normal*		*Tumor*	
	THb	**μ_s'**	**THb**	**μ_s'**	**THb**	**μ_s'**	**THb**	**μ_s'**
M1	4.9	3.6	3.0	4.3	5.2	3.8	3.4	4.4
M2	4.6	6.6	3.0	4.1	4.6	6.3	3.3	4.0
M3	14.3	5.5	9.6	3.3	13.9	5.5	9.8	3.9

4.3.4 Extraction of tissue parameters from lumpectomy specimen

We have shown in Section 4.3.1 that the spectral imaging system has sufficient SNR in human breast tissues, which was the goal of our initial clinical study with this PD-based imaging system. We then used the inverse Monte Carlo model to extract total hemoglobin, β-carotene, and reduced scattering from the tissue sample to compare these values with those that we have seen in previous margin assessment studies done using a research grade benchtop spectrometer with an 8-channel fiber-optic probe [47, 71, 72]. Figure 24 shows the spectral map of the 16 channels for the 3 tissue parameters that we found to be significant in previous studies. The gray circles in the images indicate the channels which drifted significantly during the liquid phantom study. Without an accurate reference phantom to use in the inverse Monte Carlo model, the extracted information for those channels cannot be used to quantify breast morphology.

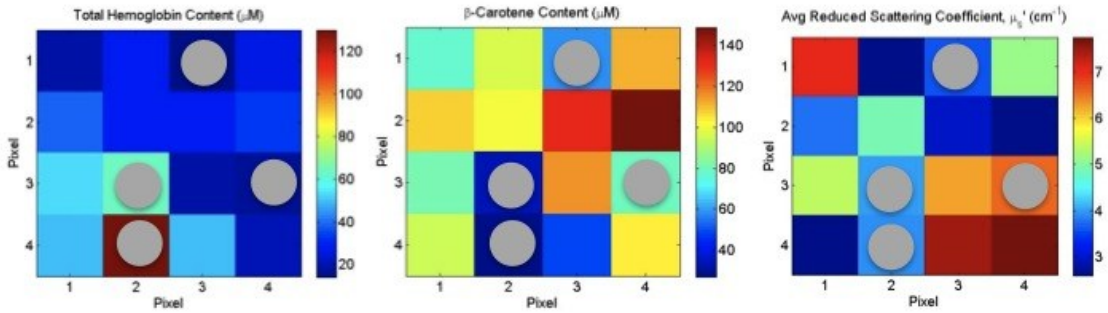

Figure 24: Extracted total hemoglobin content, β-carotene content, and average reduced scattering coefficient for lumpectomy specimen; gray circles in channels 3, 10, 12, and 14 indicate unreliable measurements due to lack of an accurate reference phantom used in Monte Carlo inversions.

From all of the existing data from our previous clinical studies, we found that the 10th - 90th percentile of the empirical cumulative distribution function of extracted total hemoglobin in breast tumor margins is 10.7 – 97.9 μM; β-carotene is 7.1 – 37.6 μM; and μ_s' is 3.7 – 11.9 cm^{-1} [47, 71, 72]. From the spectral maps shown in Figure 24, our system extracted total hemoglobin content and reduced scattering coefficients in a reasonable range, similar to what we have seen in previous studies. However, β-carotene extractions were all well above the expected range. This can be attributed to the reduced number of wavelengths in this system being unable to separate the features of hemoglobin and β-carotene absorption. Our previous 1CH and 8CH clinical systems collected spectra in the 450-600 nm range, and the data analysis included 61 total wavelengths evenly spaced in that range. The reduced wavelength imaging system only has 8 wavelengths in the 400-600 nm range with only 2 wavelengths (470 and 500 nm) collected in the 450-500 nm range, where β-carotene has a prominent spectral feature. In our previous studies, we found that β-carotene is highly significant in determining margin status; thus, there is a further need for wavelength optimization for the application of breast margin assessment.

4.4 Conclusions

In this chapter, we have shown that our spectral imaging system prototype achieves sufficient SNR in phantoms, animal tissue, and human tissue. We have made

improvements to our previous proof-of-concept work to move towards clinical translation. Previously, we had mechanically drilled the apertures in the much thicker commercial photodiodes. Each of the 16 apertures cannot be replicated and thus the probe geometry was difficult to model. With these fabricated custom thin photodiodes, the modeling (thus Monte Carlo extraction accuracy), throughput, and SNR were improved. For detector channels that had high responsivity and had no drift in measured signal, the extraction errors for optical properties were < 15%. We achieved 40-50 dB SNR in phantoms, mouse tissue, and human breast tissue. Furthermore, in the animal study, we were able to extract total hemoglobin and tissue scattering with < 10% variation between our spectral imaging prototype and another well-tested commercial spectrofluorometer. For the lumpectomy study, we found that we were able to extract total hemoglobin and tissue scattering within the expected range based on previous reports. However, the extraction of β-carotene was out of the expected range. In subsequent iterations of system development, we will utilize wavelengths that are optimized for the extraction of breast tissue parameters, such as hemoglobin, β-carotene, and μ_s'. This will be presented in Chapter 5. The work described in this chapter is an important step towards fulfilling an unmet clinical need in breast tumor margin assessment.

I would like to acknowledge the collaborative effort for the work presented in this chapter. Henry Fu built the 3x3 fiber-based spectral imaging device described in the

introductory section. Sulochana Dhar fabricated the annular silicon photodiode array. Narasimhan Rajaram provided the murine tumors for our initial testing in an animal model. Jennifer Gallagher consented the lumpectomy patient for our initial clinical study and assisted with the *ex vivo* breast tissue study.

5. Wavelength Optimization for quantitative spectral imaging of breast tumor margins

The several iterations of system design discussed in the previous chapters focused on the detection aspects of DRS imaging, making it more compact, cost effective, and easily scalable. The discrete wavelengths were not optimized for any particular clinical application. At the conclusion of Chapter 4, we found that β-carotene, an important diagnostic parameter of breast tissue, was not extracted correctly using the semi-evenly spaced wavelengths between 400-600 nm. This chapter addresses the very important issue of wavelength selection for quantitative spectral imaging of breast tumor margins.

5.1 Introduction

To quickly recapitulate the previous chapters, we have developed an fiber optics based spectral imaging system (8CH) to detect differences between benign and malignant breast tissues for the application of breast tumor margin assessment during partial mastectomy surgeries [71]. The system leveraged the principles of diffuse reflectance spectroscopy and spectral imaging in the visible spectrum, which is commonly used to non-destructively measure tissue optical properties. The propagation of multiply scattered photons is sensitive to the absorption in biological molecules and can ultimately provide contrast in adipose tissue content (β-carotene absorption), vascularity (hemoglobin absorption) and scattering (fibroglandular content). The

system consisted of a broadband illumination source, an 8-channel fiber optic conduit to direct light to and from the tissue, and an imaging spectrograph and cooled CCD for detection. Each placement of the imaging probe allowed for diffuse reflectance spectra (450-600 nm) to be measured from up to 8 sites on the margin. Multiple placements of the probe allowed for mapping the entire margin surface. Using our fast, scalable Monte Carlo reflectance model, optical properties of the specimens were extracted to create tissue composition maps, such as those shown in Figure 25(a), (c), and (e) for normal adipose, ductal carcinoma *in situ*, and invasive ductal carcinoma, respectively [49, 73].

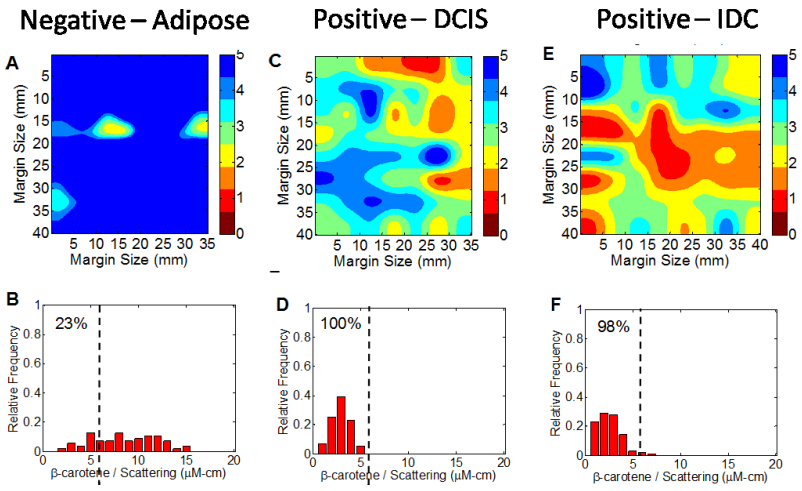

Figure 25: Example tissue composition maps of extracted ratio of [βc]/<μs'> for (a) negative margin and (b) its corresponding frequency histogram, (c) a positive ductal carcinoma *in situ* margin and (e) a positive invasive ductal carcinoma margin and their respective histograms (d) and (f).

5.1.1 Significant tissue paramters

We reported on an initial subset of patients in a clinical study (n = 48) by using a leave-one-out cross-validated tree-based model and found that the ratios of [βc]/<μ_s'> and [THb]/]/<μ_s'> can be used to detect margin positivity with a sensitivity of 79.4% and a specificity of 66.7%. We found that pathologically-confirmed positive margins showed significantly lower β-carotene/scattering ratios compared to negative margins. This finding reflects a decrease in fat content and an increase in fibroglandular content associated with margin positivity [72]. Figure 25 is an example of using [βc]/<μ_s'> = 6 as a threshold on the margin images to determine margin positivity.

The clinical adaptability of this technology will be impacted by its size, cost, and the time needed to map out the tumor margins. This motivated the design of a compact and cost-effective device based on the utilization of a few discrete wavelengths for illumination to replace a broadband source and monochromator in the original system and inexpensive photodiode arrays for detection in lieu of a spectrograph and CCD camera as discussed in great detail in Chapters 2-4 [105, 108, 109]. An important aspect of this redesigned system is the selection of wavelengths and bandpass needed to minimize complexity and acquisition time, while still achieving the same sensitivity to the relevant sources of optical contrast in the breast, specifically hemoglobin content, β-carotene content, and tissue scattering.

5.1.2 Previously reported wavelength selection methods

Several groups have reported on the optimization of wavelength combinations for different applications. Using a matrix decomposition of basis spectra and simulation of tissue data, Mazhar et al. optimized wavelength pairs to measure hemodynamic changes in the near-infrared range for breast imaging applications with diffuse optical tomography [110]. Although water content in the skin varies between 25-75% and lipid varies between 0-50%, the simulations only take into account 50% water and 2% lipids that degrade the quality of fits and extraction errors. The selected wavelength pairs (670 nm / 850 nm) ultimately helped reduce acquisition time over 30-fold and improved spatial resolution due to reducing motion artifacts. However, the accuracy of the extractions are unknown because the wavelength pair was selected based on the simulation of a tissue properties of one representative sample. Also designing their system in the near-infrared range, Umeyama and Yamada accounted for cross-talk of measured chromophores in optimizing wavelength combinations for studying the brain [111]. They studied concentration changes in oxygenated and deoxygenated hemoglobin by solving a linear equation based on the Beer-Lambert law. Without any clinical data, the study is entirely computational, varying wavelengths in increments of 20 nm from 680-820. Ferreira et al. presented a strategy for spectroscopic imaging of esophageal tissue, featuring 16 discrete wavelengths in the 350-750 nm range [112]. Instead of performing true optimization of wavelengths for their clinical application, the

selection of wavelengths was device-driven and constrained to the filter fabrication process, i.e. materials, number of layers, FWHM, etc. They selected wavelengths of filters that they are able to fabricate and performed wavelength reduction simulations on previously acquired tissue data to ensure that the extractions are similar between the full spectrum and the reduced wavelength spectrum. With a broad wavelength range between 350-750 nm (thus a large variation of tissue sensing depth), it is unclear where the tissue contrast exists and why 16 discrete wavelengths are needed for only hemoglobin concentration and tissue scattering. In our group, Phelps et al. developed a ratiometric method to rapidly estimate total hemoglobin concentration in the UV-visible range [113]. Monte Carlo simulations of 50 different tissue models were conducted to determine the best isosbestic ratios of oxygenated and deoxygenated hemoglobin that can predict total hemoglobin concentration, independent of varied tissue scattering. The results were validated in tissue phantoms and applied to an *in vivo* dysplastic cervical tissue study, showing correlations between 0.75-0.88 for tissue parameters extracted with wavelength ratios compared to the full wavelength spectrum. All of these previous studies show the importance of optimizing wavelength choices when reducing the acquisition from a full wavelength spectrum to just a few discrete wavelengths, but are somewhat limited to their own applications and not fully tested, inclusive of a broad range of tissue properties observed clinically.

In this chapter, a wavelength optimization strategy is described for quantitative optical spectral imaging for breast tumor margins. In previous discussion, we have found that total hemoglobin, β-carotene, and tissue scattering (μ_s') are significant parameters for determining breast tumor margin status. The number of necessary wavelengths to accurately characterize the tissue is dependent on the assumption of the number of different molecules and parameters in the tissue. Based on the Beer-Lambert law and Mie theory, we have used the Monte Carlo reflectance model to extract several tissue parameters, not all of which are significant for determining margin status: oxygenated hemoglobin, deoxygenated hemoglobin, β-carotene, tissue scattering, and Lymphazurin, which is a contrast agent used for the delineation of lymphatic vessels during breast conserving surgery. So, analogous to Umeyama and Yamada's optimization work in solving linear equations based on the Beer-Lambert law, we would need at least 6 wavelengths to solve for 5 unknown parameters in the tissue. Additional wavelengths would presumably improve the extraction errors; however, from a portable, cost-effective system design perspective, we would like to minimize the number of wavelengths used while still maintaining contrast in various tissue types. With a wide range of wavelength choices and no prior systematic way to evaluate the potential wavelength solution sets, we have developed an optimization method based on a search heuristic known as a genetic algorithm. The algorithm mimics the process of natural evolution and generates potential solutions of reduced wavelengths, whose

suitability for achieving high sensitivities to the sources of optical contrast in the breast are evaluated independently to result in an optimal reduced set of wavelengths that can preserve as much of the information contained in the original spectrum. Unlike the previously described wavelength optimization strategies, this method takes into account a broad range of clinically relevant data and selects wavelength sets from the entire spectrum of interest. Although the motivation for this work is based on investigating the optical contrast of only breast tissue (total hemoglobin, β-carotene, and μ_s'), this optimization method can also be extended for use in other spectral imaging applications, provided that a technique for measuring or simulating spectral data directly related to optical sources of contrast is available and a clear metric for quality of data extraction can be defined.

5.2 Wavelength optimization method

Figure 26 provides a broad overview of the steps taken to determine and test the best wavelength sets and spectral bandpass. First, existing *ex vivo* breast tissue reflectance data was used as a training set for the optimization algorithm. Our inverse Monte Carlo reflectance model [73] was used to extract the tissue optical properties from the training set using various constraints, such as the total number of wavelengths, the range of wavelengths, and the increment of each wavelength from which to select. Combined with a genetic algorithm for global optimization, the best wavelength sets are

identified by minimizing the sum of tissue property extraction errors from the reflectance spectra. The selected wavelengths are then validated with an independent pathology-confirmed *ex vivo* breast tissue data set. A tissue-mimicking phantom experiment was also performed as part of the wavelength selection validation. The text in these subsequent sections describes the methods in greater detail.

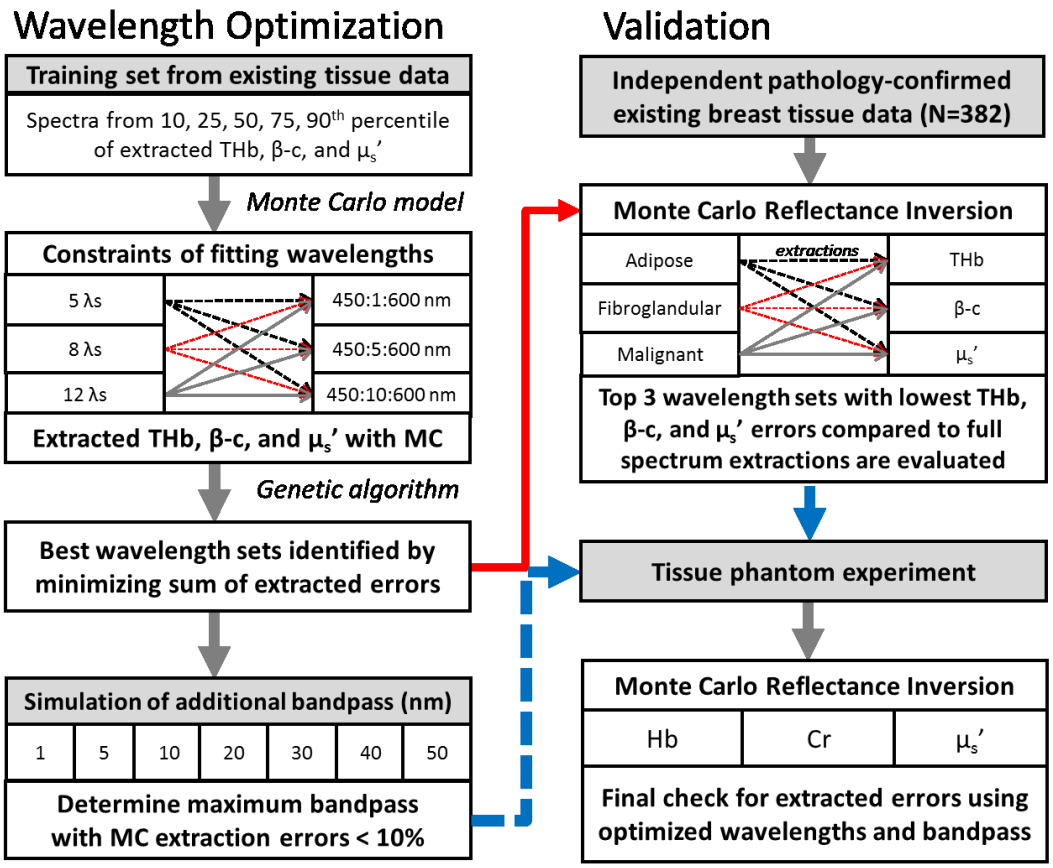

Figure 26: General flow chart illustrating the process for selecting and testing the optimal wavelength sets and spectral bandpass in clinical data obtained from breast tumor specimens and in tissue phantoms.

5.2.1 Diffuse reflectance spectra from *ex vivo* breast tissue specimens

As mentioned throughout this dissertation, the dominant absorbers in breast tissue are hemoglobin and β-carotene. Previous studies have shown that β-carotene and tissue scattering are significant parameters that can be used to differentiate between malignant and benign breast tissues [45, 47, 71]. To select the minimum set of wavelengths in the visible spectral range that are sensitive to these key tissue constituents, an existing data set of 4953 diffuse reflectance spectra measured from an *ex vivo* clinical study at Duke University Medical Center involving partial mastectomy procedures on 100 patients was used as a training set for the wavelength optimization [47, 72]. The diagnosis for the 101 margins were as follows: 44 negative (> 2 mm normal tissue), 35 close (< 2 mm normal tissue), and 22 positive. In addition, routine histopathology was performed on a subset of these measurements, and the study pathology classified 6-10 randomly selected measurement locations (or "sites" on the margins). A total of 320 normal adipose sites, 24 normal fibroglandular sites, and 38 malignant sites were used for testing the optimized wavelength sets.

Total hemoglobin [THb], β-carotene [βc], and reduced scattering coefficients $<\mu_s'>$ for each of the 4953 diffuse reflectance spectra were extracted using a previously developed inverse Monte Carlo model of reflectance [49, 73]. Reflectance spectra of samples at the 10th, 25th, 50th, 75th, and 90th percentile of the empirical cumulative distribution functions (cdf) of [THb], [βc], and average $<\mu_s'>$ were chosen resulting in a

total of 15 reflectance spectra in the training set. This method ensured that the data are sampled evenly over the distributions rather than the parameter value ranges, which could result in oversampling of samples at the periphery of the distributions.

Table 12: Breast tissue properties extracted with the inverse Monte Carlo of reflectance. The highlighted portions denote the 10th, 25th, 50th, 75th, and 90th percentiles of [THb], [βc], and average <μs'> extracted from measured ex vivo breast specimens.

Sample	[THb] (μM)	[β-carotene] (μM)	$<\mu_s'>_{450-600}$ (cm^{-1})
1	10.7	7.5	4.1
2	18.1	21.7	5.3
3	32.7	18.6	11.5
4	59.3	21.0	8.0
5	97.9	16.6	4.4
6	55.7	7.0	3.9
7	49.6	11.3	9.2
8	32.8	17.5	6.3
9	73.1	26.0	8.8
10	95.9	37.6	8.4
11	24.2	13.6	3.7
12	22.3	29.3	4.8
13	40.3	31.3	6.5
14	91.1	15.8	8.9
15	11.5	30.8	11.9

Table 12 lists the extracted breast tissue properties for each of the 15 selected reflectance spectra for the wavelength optimization training set. The shaded sections of the table indicate the 10th through 90th percentiles of each parameter. The objective in selecting reflectance spectra based on the cdfs extracted from an extensively large data set of previously measured *ex vivo* breast tumor margins was to cover a wide range of

[THb] (10.7 – 97.9 μM), [βc] (7.0 – 37.6 μM), and average <μ_s'> over 450 – 600 nm (3.7 – 11.9 cm^{-1}).

5.2.2 Combined inverse Monte Carlo reflectance model and genetic algorithm to select center wavelengths

The 15 selected reflectance spectra described from the previous section were used in a wavelength optimization technique that combines our inverse Monte Carlo model of reflectance [73] with a genetic algorithm (GA) (Global Optimization Toolbox in MATLAB, The MathWorks, Natick, MA). Briefly, the GA is based on the "survival of the fittest," a phrase originating from evolutionary theory. The algorithm has two major components: (1) the population of individuals (or possible solutions) with its own unique string of "chromosomes" and (2) a fitness function that evaluates the possible solutions. Typically, a population of solutions is randomly generated for a given range of possible solutions. The fitness function is used to evaluate each individual from that population. All of the individuals from the populations are then ranked according to their fitness values. From this existing population, a user-identified proportion is selected to breed a new generation of solutions, and those solutions with fitter values are more likely to be selected. The parent solutions reproduce new offspring solutions by genetic operators such as crossovers or mutations, which essentially results in changes of chromosomes in the offspring and maintains genetic diversity in the subsequent populations. The GA ends when a solution that satisfies the criteria is found, a

designated computational time is reached, or a specified generation number is reached. Figure 27 is a general diagram of the steps taken for wavelength optimization, combining an inverse Monte Carlo reflectance model with the GA.

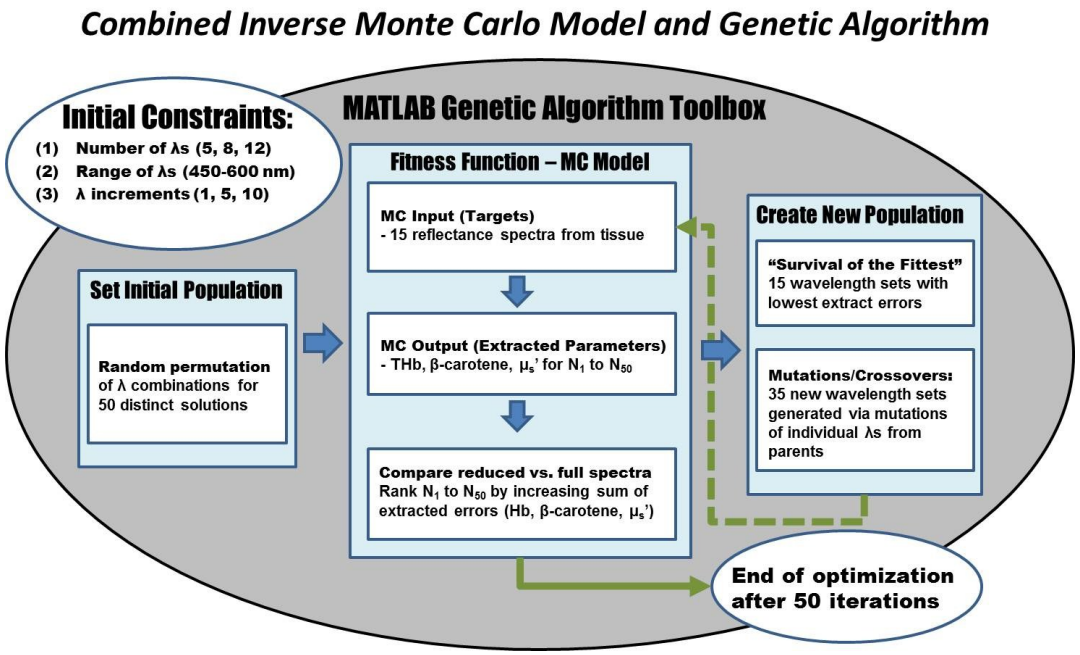

Figure 27: Diagram detailing the steps of selecting wavelengths for quantitative tissue spectroscopy using the genetic algorithm and inverse Monte Carlo model.

The algorithm begins with the initial constraints of the wavelengths to be used. To extract the 4 parameters of oxy-hemoglobin, deoxy-hemoglobin, β-carotene, and reduced scattering coefficients, at least 5 center wavelengths are needed. The initial population of wavelength sets is created by a random permutation of 50 different wavelength combinations, for 5, 8, and 12 wavelengths in 1, 5, and 10 nm increments

from 450-600 nm (151, 31, and 16 possible center wavelengths, respectively). The selection of wavelengths in 1 nm increments represents an ideal situation in system design in which the types of sources available are not limited. The selection of wavelengths in 5 and 10 nm increments represents a more realistic situation, in which the final optimized set of wavelengths will likely be commercially available in the form of bandpass filters. These different wavelength combinations serve as the initial solutions of the iterative GA. The inverse MC model serves as the GA's fitness function, which is used to evaluate the suitability of each set of wavelengths as a possible solution for extracting $<\mu_a>$, thus [THb] and [βc], and $<\mu_s'>$ from the training set.

In the 1st generation of the GA process, the output of the fitness function is 50 sets of extracted breast tissue properties, [THb], [βc], and average $<\mu_s'>$, for 15 samples using each of the 50 reduced wavelength solution sets. These extracted tissue parameters were compared to those extracted using the full 450-600 nm spectrum. The goal of the optimization is to minimize the fitness value of the function, which was defined as the sum of extracted [THb], [βc], and average $<\mu_s'>$ errors for the 15-sample training set. The 50 individual wavelength sets were ranked by increasing fitness values (sum of extracted errors) for the 15-sample training set. To create the subsequent population of the next 50 wavelength sets to be evaluated, the top 15 wavelength sets with the lowest sum of errors from the previous population were allowed to survive to the next generation. The new generation of the remaining 35 wavelength sets was then

created by means of single-point crossovers or mutations of chromosomes (or changes in individual wavelengths). For instance, 2 individuals ($A_{1,2,\ldots,8}$ and $B_{1,2,\ldots,8}$) are chosen as parents of an offspring in the new generation. In a crossover operation, a random chromosome number (or individual wavelength) serves as the point where A and B break and exchange chromosomes, making a new individual. In a mutation operation, a new chromosome (wavelength) is randomly generated from a Gaussian distribution and replaces a chromosome of the parent wavelength set, creating a new wavelength set. The selection of the parent wavelength sets from the previous generation to crossover or to mutate and pass on to the next generation is based on the simulation of a roulette wheel, in which the area of the wheel corresponding to a parent is inversely proportional to the parent's fitness value, or sum of extracted errors. In other words, the lower the wavelength set's extracted errors, the higher the probability of that wavelength set is selected, crossed over or mutated, and passed down to be part of the next 50 solutions to be evaluated. In this particular study, the crossover fraction is set at 20%, which means 7 of the 35 solutions are the result of a crossover while the remaining 28 are the result of mutations. In the cases of any resulting offspring from a crossover operation having duplicate wavelengths, one of the duplicate wavelengths is discarded, and a new wavelength is randomly generated and inserted in the wavelength set.

This process iterates until one of two stopping criteria are met. First, the algorithm can be stopped when the minimum fitness value of the generation is

unchanged for 10 generations, which indicates that the optimization has plateaued and likely minimized. The algorithm also ends after 50 generations to save time. One run of the optimization process takes approximately 21-28 hours, depending on the initial constraints tested. The highest ranked 3 solutions from the final generation produced by each GA process were further evaluated using previously described clinical data, independent from the 15 spectra used in the selection process.

5.2.3 Selection of optimal bandpass

In addition to selecting the most appropriate total number and the center wavelengths of the source, it is also important to understand the effect of increasing full-width half-maximum (FWHM) on the accuracy of the extraction of optical properties. While laser diodes can have very small FWHM, it may not be possible to obtain sources at every wavelength in the optimized solutions. On the other hand, bandpass filters are commercially available at every 10 nm center wavelength in the UV-NIR spectrum, but may come at a cost of 10 nm FWHM around the center wavelength. Light emitting diodes (LEDs) often have even larger FWHM, commonly ranging from 20-50 nm.

Forward Monte Carlo simulations were conducted to study the effect of increasing bandpass. Using the wavelength-dependent optical properties of the 15 clinically measured spectra chosen for the training set described in Section 4.2.1, diffuse reflectance spectra were generated. The wavelength-dependent absorption coefficients, μ_a, were determined using the molar extinction coefficients for oxy- and deoxy-

hemoglobin, as well as β-carotene. The reduced scattering coefficients, μ_s', at each wavelength were calculated using Prahl's Mie scattering program [101]. The simulations were scaled for the probe geometry used in the clinical measurements [73]. For each of the 15 simulated spectra, FWHM of 1, 5, 10, 20, 30, 40, and 50 nm were added. Gaussian distributions of 1, 5, 10, 20, 30, 40, or, 50 nm in width were used. Each of the 15 original clean spectra was convolved with the Gaussian distributions. The results are 15 different tissue spectra, each with 7 different FWHM.

The inverse Monte Carlo model was used to extract [THb], [βc], and average $\langle\mu_s'\rangle$ values from the 15 reflectance spectra with various FWHMs. The extractions were repeated for the top 3 solutions from the wavelength optimizations for 5, 8, and 12 total center wavelengths. The extracted parameters from the reduced wavelengths set with added FWHM were compared to those of the full, simulated spectra without added FWHM. Because these simulations did not include system and measurement artifacts that may exist in measured clinical data, a 10% error was set as the threshold for determining an acceptable FWHM in the analysis.

5.3 Wavelength validation method

5.3.1 Independent pathology-confirmed tissue data

The results from the wavelength optimization were tested against an existing breast tissue data set, independent of the 15 spectra used for the training set described in

Section 5.2.1. The inverse Monte Carlo model was used to extract [THb], [βc], and <μ_s'> from each of the 382 pathological confirmed sites (320 adipose, 24 fibroglandular, 38 malignant) obtained from breast tumor margins. The tissue extractions were performed for the full spectrum of 450-600 nm in 2.5 nm increments for a total of 61 wavelengths, and for the top 3 optimized solutions for each of the test cases: 5, 8, and 12 total wavelengths in 1, 5, and 10 nm increments. To show the differences between optimization and non-optimization, tissue extractions were also made using the semi-evenly spaced wavelengths empirically chosen from 400-600 nm used in a previously reported system [114]. Using the full spectrum [THb], [βc], and <μ_s'> extractions as the gold standard, errors in the extracted parameters resulting from the reduced wavelength sets were calculated.

5.3.2 Multi-absorber liquid phantom study shows benefit of wavelength optimization

A set of 20 phantoms was used to further assess the results from the wavelength optimization. The liquid tissue-simulating phantoms were prepared by mixing polystyrene microspheres (07310, Polysciences, Inc) as the scatterer with water soluble hemoglobin (H0267, Sigma Co.) and crocin (17304, Fluka) as the absorbers. Hemoglobin and crocin were used as the absorbers since they have been used to simulate blood and β-carotene in breast tissue [84]. Based on the optical properties of β-carotene found in previous studies, the appropriate crocin level was added by matching the mean μ_a of these two absorbers with similar spectral features [71]. The 2 scattering levels represent

the means over 450-600 nm of representative malignant (μ_s'=9 cm^{-1}) and normal (μ_s'=12 cm^{-1}) breast tissue. The optical properties of the phantoms are shown in Table 13.

Table 13: Average absorption coefficients (450-600 nm) of phantoms containing hemoglobin, crocin, and polystyrene microspheres. Each absorber level was tested for 2 scattering levels (avg μ_s' = 9 cm^{-1} and μ_s' = 12 cm^{-1}) for a total of 20 phantom.

Hb Level 1			Hb Level 2		
Mean μ_a (cm^{-1})			Mean μ_a (cm^{-1})		
Total	Hb	Cr	Total	Hb	Cr
0.51	0.51	0.00	0.91	0.91	0.00
0.99	0.51	0.48	1.72	0.90	0.82
1.23	0.51	0.72	2.12	0.89	1.23
1.47	0.51	0.96	2.53	0.89	1.64
1.70	0.50	1.20	2.93	0.88	2.05

The phantom optical measurements were obtained with a previously reported system with slight modifications as shown in Figure 28 [108]. The system consists of a 450W xenon arc lamp and a scanning monochromator (Gemini 180, JY Horiba) coupled to a 600 μm optical fiber as the source. The spectral bandpass of the illumination was fixed at 7 nm. A custom annular silicon photodiode with 2.5 mm outer diameter and 0.75 mm inner diameter was used for detection [107]. The optical fiber was fitted through and epoxied in the detector aperture to illuminate the phantoms, and the detector was connected to a photodiode amplifier (PDA-850, Terahertz Technologies, Inc.) for reflectance measurements. Diffuse reflectance measurements were taken at the discrete wavelength solutions as well as at the evenly spaced wavelengths from 400-600

nm in order to compare the optimized solution to one which samples wavelengths at regularly spaced intervals over the visible spectral range as previously described [105]. The inverse Monte Carlo model was used to extract optical properties from each phantom and root mean square (RMS) errors were compared for both sets of wavelengths.

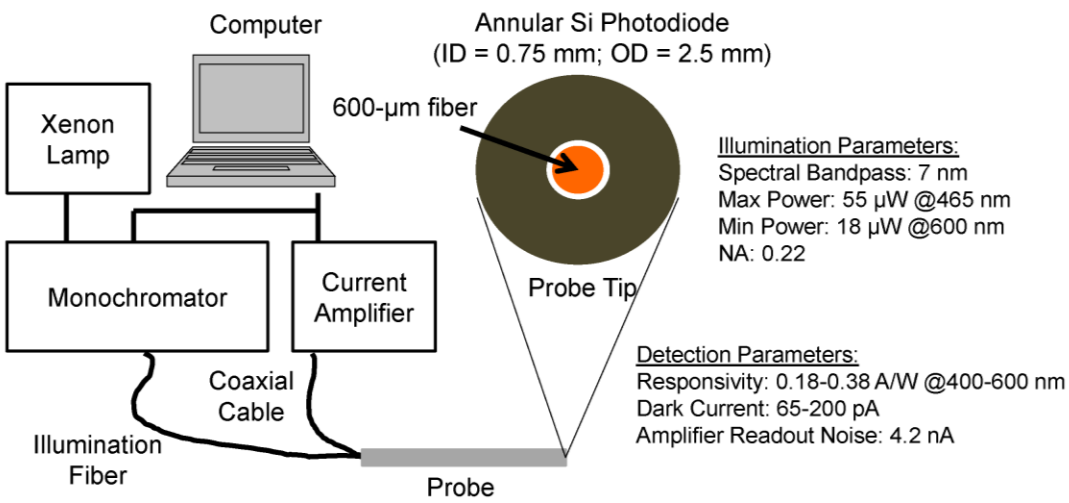

Figure 28: Schematic of instrument and probe geometry used to obtain phantom optical measurements.

5.4 Results and discussion

5.4.1 Eight wavelengths can be used to accurately extract [THb], [βc], and <μ_s'>

Table 14 enumerates the top 3 solutions for each of the constraints in the optimization, including wavelength range, increment, and total number of wavelengths.

Table 14: Top solutions for each optimization. The score indicates the minimized average errors of the extracted parameters from the 15 representative reflectance spectra chosen from the breast tissue data set .

λ range	# of λs	Optimized Wavelengths	Score
450:1:600	12	451 460 474 483 487 502 511 560 579 584 585 596	11.7
		451 460 474 483 502 509 511 560 573 584 585 596	11.8
		466 479 491 500 516 527 532 560 566 574 590 597	12.0
	8	489 492 503 522 537 558 583 592	12.2
		474 481 498 509 555 573 593 596	12.3
		485 492 503 510 537 544 560 593	12.5
	5	485 496 512 547 589	18.1
		478 499 513 582 596	19.5
		482 496 527 576 597	19.7
450:5:600	12	460 470 485 490 505 525 530 535 550 570 575 600	11.9
		460 470 475 480 485 500 515 525 530 555 585 595	12.2
		455 465 470 490 505 510 515 530 550 560 590 595	12.4
	8	480 485 500 505 535 550 580 595	12.4
		460 485 500 510 555 560 580 600	12.7
		450 480 500 505 545 555 585 600	13.2
	5	485 495 510 540 590	18.5
		490 520 525 570 595	18.7
		485 495 510 545 595	19.9
450:10:600	12	450 470 480 490 500 510 520 530 540 560 580 600	12.0
		460 470 480 490 510 530 540 550 560 570 580 600	12.1
		450 460 490 500 510 530 540 550 560 570 580 600	12.3
	8	460 490 510 520 540 550 580 600	12.4
		470 480 490 500 510 560 580 600	12.6
		480 500 510 530 550 560 570 600	13.3
	5	480 490 520 540 590	19.0
		480 490 520 550 600	19.9
		450 490 520 530 590	20.3

For the optimized solutions chosen from 450-600 nm in 1 nm increments, the average errors of extracted THb, βc, and μ_s' increases from 11.7% to 12.2% to 18.1% as the total number of wavelengths used decreases from 12 to 8 to 5. When selecting in 5 nm and 10 nm increments, the errors increase from 11.9%-18.5% and 12.0%-19.0% as the wavelengths decrease from 12 to 5, respectively. This trend is not unexpected because as the total number of wavelengths as well as available center wavelength choices decrease, the possibility of capturing the spectral features of the absorbers and scatterers in tissue also decreases, thus increasing the extracted errors.

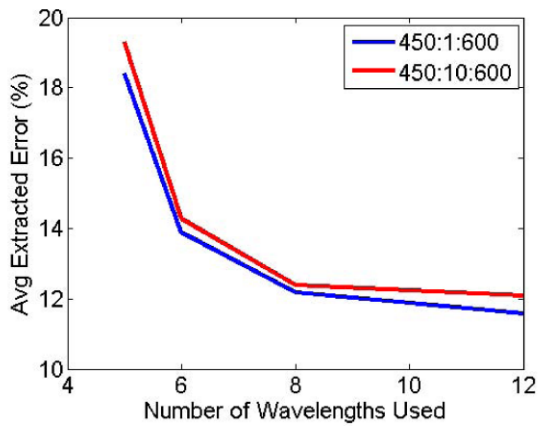

Figure 29: Average extracted % error of [THb], [βc], and <μ_s'> for 5, 6, 8, and 12 total wavelengths selected from 450-600 nm in 1 and 10 nm increments.

Figure 29 puts into perspective the optimal number of illumination wavelengths required for the design of a breast spectral imaging system. At 5 wavelengths, the average extracted percent error of [THb], [βc], and <μ_s'> from the 15 representative

breast tissue reflectance spectra was close to 20%. The increase to 6 and 8 wavelengths improved the extraction errors to 14% and 12%, respectively. There are diminishing returns in improving extraction errors by adding more wavelengths past 8. The graph shows that for our particular application for breast tumor margin assessment, the appropriate number of wavelengths to use is 8.

5.4.2 Spectral bandpass affects extraction accuracy

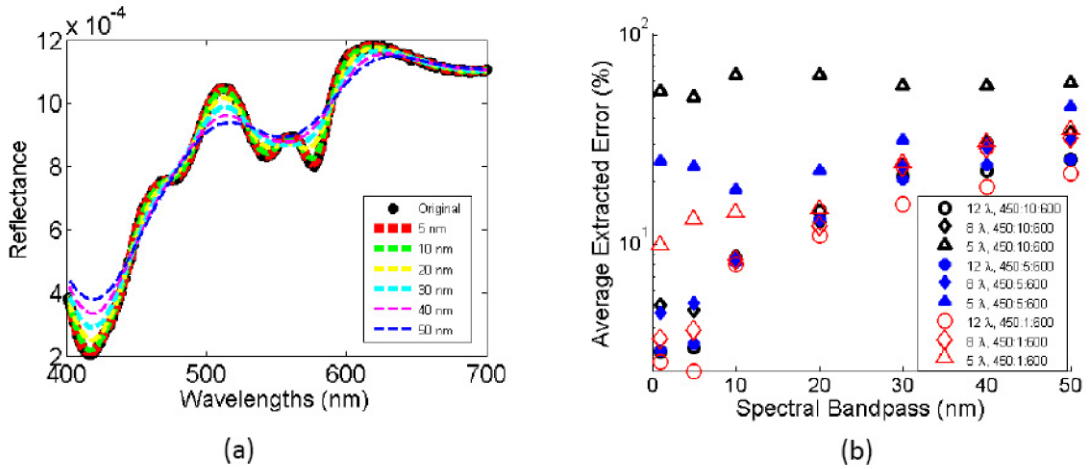

Figure 30: (a) Simulation of the effect increasing spectral bandpass on a diffuse reflectance spectrum representing 10 μM [THb], 5.5 μM [βc], and 3.11 avg <μs′>. (b) Average extracted errors of [THb], [βc], avg <μs′> with increasing spectral bandpass.

Because the system used to obtain the existing breast tumor margin data had a spectral bandpass of 3.9 nm, it is challenging to evaluate the effect of changes in bandpass and to optimize both the wavelengths and bandpass of a system. The forward

MC model was used to simulate the same 15 reflectance spectra used in the wavelength optimization. The original spectra were degraded to simulate increases in spectral bandpass of 5, 10, 20, 30, 40, and 50 nm. Representative reflectance spectra (10 μM [THb], 5.5 μM [βc], and 3.11 avg <μ_s'>) with these changes in spectral bandpass are shown in Figure 30(a). The extracted errors from each case are shown in Figure 30(b). The results in Figure 30(b) show that to extract the breast tissue properties with good accuracy, the wavelengths must have < 10 nm FWHM, and 8 or more wavelengths have to be implemented in the system design.

Parameter extraction accuracies are affected by not only the number of wavelengths and the center wavelengths used, but also by the spectral bandpass of the wavelengths. It has been shown through existing clinical data that using 5 wavelengths is likely inadequate for accurate extractions of breast properties. The simulations on the effect of widening spectral bandpass also show that the errors with 5 wavelengths are nearly double those of 8. Similar to previously measured data, the increase from 8 to 12 wavelengths did not seem to have a significant impact on improving the extraction accuracy.

5.4.3 Optical contrast in breast tissue is retained with optimized wavelength choices

The top 3 optimized solutions with 5, 8, and 12 total wavelengths selected from 450-600 nm in 1, 5, and 10 nm increments were tested in an independent partial mastectomy tissue data set. Although the initial 15 reflectance spectra selected in the

training set spanned the 10th to 90th percentiles of [THb], [βc], and <μ_s'>, in this large data set the histological diagnoses of the tissues corresponding to these spectra were not known. Therefore, a subset of reflectance measurements for which diagnosis was histopathologically confirmed was used to independently test the optimized wavelengths, and were split into 3 tissue types: adipose, fibroglandular, and malignant.

Table 15 and Table 16 provide a summary of all errors extracted for the top 3 optimized solutions for each tissue type and for 5, 8, and 12 wavelengths in 1, 5, and 10 nm increments. A positive percent error value indicates an over-extraction by the reduced-wavelength solutions; a negative value indicates an under-estimation of the extracted parameters. When the number of wavelengths is increased from 8 to 12, the extracted errors for all 3 parameters did not improve, which was expected based on the findings shown in Figure 29. When the total number of wavelengths used is decreased from 8 to 5, however, the extracted errors are increased. For solutions selected in 1 nm increments, the extracted [THb] from normal adipose, normal fibroglandular, and malignant tissues using 8 wavelengths differed by 8.5%, -2.6%, and 4.1% from the full 61-wavelength set, respectively. When the wavelengths were reduced to 5, the errors increased to 22.2%, 23.3%, and 21.0% for the 3 tissue types. Similarly, with 8 wavelengths, the extracted [βc] errors for the adipose, fibroglandular, and malignant tissues were -3.0%, -7.0%, and 4.4%. With just 5 wavelengths, the errors increased to -10.2%, -18.1%, and 11.8%. The extracted reduced scattering coefficient errors were also

more than doubled (7-9% to 17-24%) when total wavelengths decreased from 8 to 5. Because the motivation for this work is to provide a method of optimizing wavelength choices for a compact, cost-effective, and fast spectral imaging device that also has a simplistic design, the solutions with 12 total wavelengths were eliminated and only 8 total wavelengths are used for subsequent system design to be described in the next chapter.

Although the top optimized solution for each wavelength selection constraint had the lowest average errors of [THb], [βc], and $<\mu_s'>$ extracted from the 15 representative reflectance spectra in the training set, the best choice of wavelengths from the independent breast data set validation is not necessarily the same as the best solution from the training set. The shaded regions in Table 15 and Table 16 indicate the best wavelength sets for the extraction of [THb], [βc], $<\mu_s'>$, and the ratios of [THb]/$<\mu_s'>$ and [βc]/$<\mu_s'>$ given each constraint of total wavelengths and wavelength increments. The best wavelength set for extracting optical parameters with the lowest errors in the histopathology confirmed data set is solution #1: 474, 481, 498, 509, 555, 573, 593, 596 nm for the wavelengths selected in 1 nm increments. The best wavelength set selected from 5 nm increments is also solution #1: 470, 480, 495, 500, 510, 550, 580, 600 nm. However, the best wavelength set selected from 10 nm increments is solution #2: 470, 480, 490, 500, 510, 560, 580, 600 nm.

Table 15: Average extracted errors of [THb], [βc], and average <μ_s'> for adipose (A), fibroglandular (FG), and malignant (M) tissue sites for the top 3 solutions with 12, 8, and 5 total wavelengths and in 1 nm, 5 nm, and 10 nm selection increments over the 450-600 nm range. Positive values indicate an over-estimation of the extraction; negative values indicate an under-estimation.

# of λ, range & increment	Tissue Type	Hemoglobin			β-carotene			Scattering		
		Set1	Set2	Set3	Set1	Set2	Set3	Set1	Set2	Set3
12 λ from 450:1:600	A	3.1	2.4	4.5	-3.9	-5.5	-10.8	9.3	3.0	7.8
	FG	3.9	3.4	5.6	-13.9	-15.9	-15.7	4.2	3.9	11.8
	M	3.0	3.9	-4.8	2.1	-2.5	-11.9	8.9	2.1	5.3
12 λ from 450:5:600	A	3.8	2.0	5.6	-7.9	-4.6	-2.4	6.4	11.7	2.7
	FG	2.0	8.8	12.2	-7.6	-10.1	-11.4	11.2	4.9	10.0
	M	-2.8	6.0	5.9	-2.7	-5.2	-7.0	2.7	6.2	7.7
12 λ from 450:10:600	A	4.0	-2.2	6.0	-2.8	-8.7	-11.5	1.4	3.8	9.3
	FG	7.7	9.7	10.4	-9.6	-17.3	-14.9	3.2	10.8	15.7
	M	6.6	-6.5	4.7	-4.4	-8.5	-9.5	2.0	-4.0	7.7
8 λ from 450:1:600	A	8.5	5.5	11.0	-3.0	-1.4	-5.7	6.6	8.8	7.9
	FG	-2.6	10.4	8.7	-7.0	-18.9	-12.0	6.6	13.5	11.1
	M	4.1	-8.2	11.9	4.4	-3.0	3.2	8.5	5.0	7.7
8 λ from 450:5:600	A	7.1	7.0	8.2	-2.9	-4.7	-6.1	8.6	9.0	8.9
	FG	5.9	8.5	11.9	-6.8	-18.2	-10.0	13.3	14.6	15.5
	M	5.3	7.7	8.2	2.9	-7.7	2.1	7.1	8.7	8.7
8 λ from 450:10:600	A	11.7	6.7	13.9	-12.2	-4.8	-13.2	4.8	2.2	9.1
	FG	13.9	7.2	7.1	-15.4	-8.8	-10.0	9.0	4.5	14.8
	M	-11.8	7.5	12.9	-19.2	-2.9	-9.4	1.1	2.8	8.1
5 λ from 450:1:600	A	22.2	23.3	21.0	-20.8	-10.2	10.1	17.2	16.6	15.6
	FG	23.3	28.4	27.0	10.9	-18.1	12.5	22.8	23.5	23.2
	M	21.0	25.3	25.9	13.6	11.8	13.8	16.8	18.2	18.3
5 λ from 450:5:600	A	22.3	26.4	23.4	23.7	-23.2	24.0	18.4	18.7	18.2
	FG	27.1	29.3	20.9	28.1	-20.6	28.0	25.1	23.5	24.4
	M	23.4	26.6	22.8	18.8	-21.2	18.7	19.6	25.4	18.3
5 λ from 450:10:600	A	16.0	21.4	24.4	26.9	28.8	25.1	24.7	24.9	21.9
	FG	13.3	21.8	17.9	22.5	23.8	28.1	29.6	29.8	29.0
	M	19.7	15.6	-20.3	25.1	23.4	-21.5	20.9	22.0	-21.1
Evenly-spaced 8 λ from 400-600 nm	A	22.5			14.0			-15.5		
	FG	23.6			64.4			-18.3		
	M	17.3			15.7			-26.3		

Table 16: Average extracted errors of the ratio of [THb]/<μ_s'> and [βc]/<μ_s'> for adipose (A), fibroglandular (FG), and malignant (M) tissue sites for the top 3 solutions with 12, 8, and 5 total wavelengths and in 1 nm, 5 nm, and 10 nm selection increments over the 450-600 nm range. Positive values indicate an over-estimation of the extraction; negative values indicate an under-estimation.

# of λ, range & increment	Tissue Type	[THb] / <μ_s'>			[βc] / <μ_s'>		
		Set1	Set2	Set3	Set1	Set2	Set3
12 λ from 450:1:600	A	-2.9	-4.5	-8.4	-15.4	-6.6	-10.8
	FG	-7.0	-1.5	-13.3	-13.1	-10.9	-12.7
	M	-3.7	-4.2	-8.3	-7.9	-2.1	-8.7
12 λ from 450:5:600	A	-6.1	0.3	0.7	-5.6	-5.7	-9.8
	FG	-9.8	-7.7	-4.9	-12.8	-15.9	-13.1
	M	-6.4	-0.5	-2.2	-6.3	-11.7	-8.9
12 λ from 450:10:600	A	-3.0	-6.5	-4.1	-6.1	-8.8	-13.7
	FG	-6.0	-8.4	-6.9	-12.2	-12.8	-16.8
	M	-3.4	-3.9	-4.0	-5.6	-9.8	-9.2
8 λ from 450:1:600	A	-4.8	-6.0	-7.3	-11.3	-12.7	-15.1
	FG	-1.4	-1.5	-1.2	-10.1	-18.6	-16.4
	M	-2.5	-6.1	-6.9	-8.5	-9.6	-5.1
8 λ from 450:5:600	A	-1.8	-2.6	-5.9	-3.4	-16.9	-17.3
	FG	-5.3	-7.4	-4.7	-14.1	-12.0	-9.9
	M	-2.5	-1.7	-1.3	-5.2	-9.0	-7.6
8 λ from 450:10:600	A	-8.6	4.2	-6.0	8.3	7.6	15.0
	FG	-5.8	2.2	-9.4	19.0	14.4	19.9
	M	-8.5	4.4	-6.3	10.0	4.3	9.6
5 λ from 450:1:600	A	17.4	18.4	16.7	-21.6	-32.3	-18.4
	FG	13.1	16.3	12.7	-28.7	-30.4	-24.0
	M	15.3	21.0	19.8	-23.5	-19.8	-14.7
5 λ from 450:5:600	A	16.1	-20.4	17.3	-28.0	-21.9	-27.6
	FG	14.6	-18.3	14.4	-23.8	-32.8	-22.4
	M	15.9	-23.7	16.1	-23.3	-22.8	20.2
5 λ from 450:10:600	A	-17.6	-16.7	-17.7	23.1	28.8	-26.9
	FG	-17.4	-17.2	-16.7	-23.5	24.3	-20.8
	M	-22.0	25.8	-18.0	-21.2	24.8	-20.9
Evenly-spaced 8 λ from 400-600 nm	A	44.0			35.3		
	FG	26.6			102.1		
	M	70.1			75.5		

The wavelengths selected from 1 nm increments from 450-600 have striking similarities with those selected from both the 5 nm and 10 nm increments. From a practical system design standpoint, this is a good finding because of the abundant availability of sources in 10 nm increments, such as those of LEDs. On the other hand, the wavelengths selected from 1 nm increments (and some wavelengths in 5 nm increments) in the 450-600 nm range are not all commercially available to date. Since wavelength choices in both the 5 nm and 10 nm increments did not yield significantly different extracted errors, the 8 wavelengths selected in 10 nm increments (solution #2) were chosen for subsequent analyses in this study: 470, 480, 490, 500, 510, 560, 580, and 600 nm.

Table 17: Comparison of the percent difference between median adipose and malignant tissue and fibroglandular and malignant tissue to the percent change of extractions using the optimized wavelengths and evenly spaced wavelengths to the full 450-600 nm spectrum.

Medians	% Difference		Extraction % change from full 450-600 nm spectrum					
	Full spectrum: 450-600 nm		Optimized λs: 470, 480, 490, 500, 510, 560, 580, 600 nm			Evenly spaced λs: 400, 420, 440, 470, 500, 530, 570, 600 nm		
	A vs. M	FG vs. M	A	FG	M	A	FG	M
[THb]	-40.66	-25.16	8.90	10.48	2.63	-15.09	5.64	-1.28
[βc]	9.90	-9.54	-4.54	-8.74	-0.76	-2.74	-35.39	-6.79
$<\mu_s'>$	-36.89	22.83	1.15	11.72	2.21	18.05	26.88	27.89
$[THb]/<\mu_s'>$	-2.75	-62.18	1.84	-1.40	0.43	-40.43	-29.04	-40.45
$[\beta c]/<\mu_s'>$	13.07	-87.48	-5.75	-23.18	21.99	-25.36	-85.15	-12.12

The optimization helped identify wavelength sets that can be used to extract tissue parameters with errors < 20%; however, the acceptable extraction errors for [THb], [βc], and <μ_s'> has to be determined based on the contrast of these optical endpoints in various tissue types. In Table 17, the percent difference was calculated between the median adipose and malignant tissue samples, as well as the median fibroglandular and the malignant samples. A positive percent difference indicates that the benign (adipose or fibroglandular) tissue samples had greater extracted values than those of the malignant sample. The malignant sample showed decreased [THb] and <μ_s'> compared to the adipose samples and decreased [THb] and [βc] compared to the fibroglandular sample. Also in the table are the extraction percent changes from the full 450-600 nm spectrum compared to the 8 optimized wavelengths and the 8 evenly spaced wavelengths. A positive percent change indicates an over-estimation of the extracted values by the 8-wavelength reduced spectra compared to the full 450-600 nm spectrum. A negative percent change means that the extracted values are decreased using 8 wavelengths.

The percent change using the optimized wavelengths is smaller than the percent difference for all optical parameters so optical contrast should be preserved with these reduced wavelengths. On the flip side, the percent change using the evenly spaced wavelengths without any optimization is sometimes greater than the percent difference for the optical parameters, such as for [βc] and [βc]/<μ_s'>. This means that the optical

contrast to differentiate benign from malignant samples may be washed out if the un-optimized wavelengths are used. By examining the percent differences between optical parameters of benign and malignant samples and the mean extracted errors from Table 15 and Table 16, it was also further established that none of the top wavelength sets with only 5 wavelengths can be used for our clinical application because most of the extracted errors are greater than percent differences of the optical parameters for the various breast tissue types tested.

Figure 31 shows scatter plots of the parameter extraction comparison between the optimum 8-wavelength set, the evenly spaced 8-wavelength set, and the full 450-600 nm 61-wavelength set. Tissue types are shown in columns and extracted parameters are shown in rows. The average slopes of the linear fits are 0.99±0.04, 1.05±0.12, and 1.04±0.04 for adipose, fibroglandular, and malignant tissue types. The average intercepts are -0.03±0.62, -0.17±0.96, -0.49±0.64 for the 3 tissue types, respectively. The linear fit of the scatter plots for the optimum 8-wavelength set each have a slope close to 1 and intercept close to 0, which indicate that the reduced wavelength set is able to extract similar values of [THb], [βc], and $<\mu_s'>$ extracted with 61 wavelengths. However, using the evenly spaced 8-wavelength set, the slopes and intercepts deviate more away from 1 and 0. The 95% confidence intervals for the linear fits are also much wider as shown in the figure. The slopes for the un-optimized 8-wavelength set are 1.19±0.26, 1.27±0.29, and 0.80±0.42. The intercepts are 0.17±0.88, -0.60±3.38, and 3.40±2.78. Most

notably changed are the extracted [βc] and <μ_s'> for malignant and fibroglandular tissue types. Because our previous studies have shown that [βc] and <μ_s'> are significant parameters that provide optical contrast breast tumor margin assessment, these results further show the importance of optimizing wavelength choices.

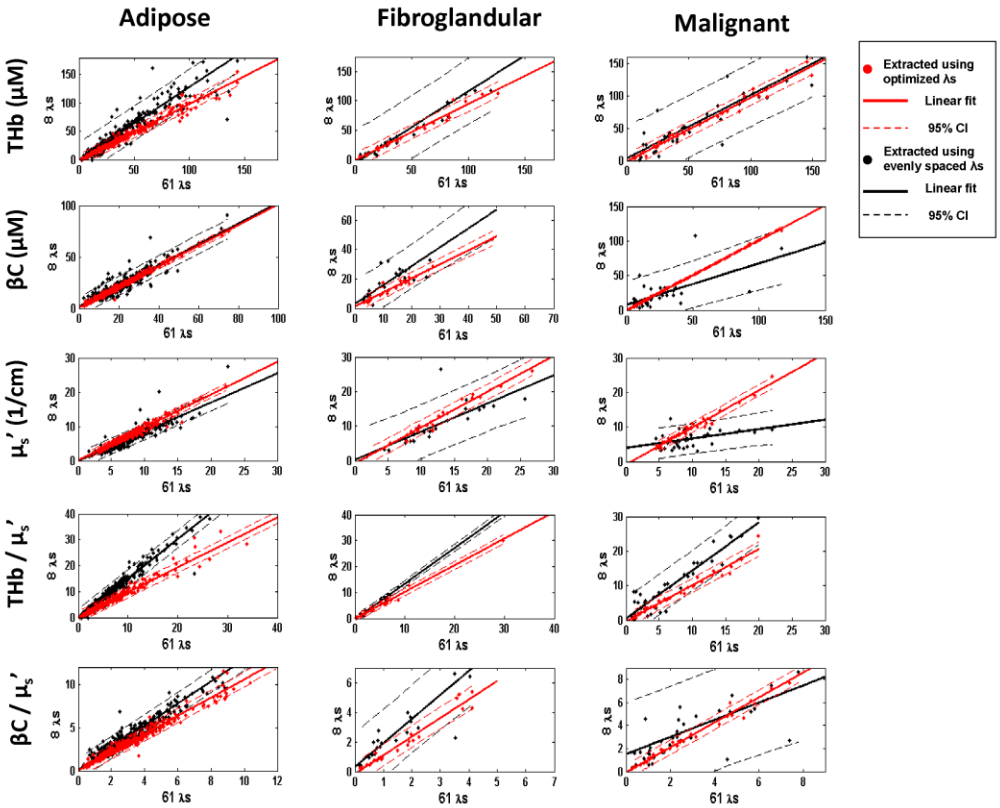

Figure 31: Comparison of the MC extractions of [THb], [βc], <μ_s'>, [THb]/<μ_s'>, and [βc]/<μ_s'> in adipose, fibroglandular, and malignant tissue types using the full spectrum versus the optimized reduced wavelength spectrum with 8 wavelengths (470, 480, 490, 500, 510, 560, 580, 600 nm) shown in red and the regularly spaced intervals (400, 420, 440, 470, 500, 530, 570, 600 nm) shown in black.

Figure 32 contains representative breast tumor margin images of extracted $[\beta c]/\langle\mu_s'\rangle$ for a negative (normal) and two positive breast resection margins: ductal carcinoma *in situ* (DCIS) and invasive ductal carcinoma (IDC). The margin images shown in (a), (e), and (i) were obtained using the full 450-600 nm spectrum. The images shown in (b), (f), and (j) were extracted using the optimized solution for 8 wavelengths: 470, 480, 490, 500, 510, 560, 580, and 600 nm. The images shown in (c), (g), and (k) were extracted using the evenly spaced 8 wavelengths used in a previous system: 400, 420, 440, 470, 500, 530, 570, and 600 nm. The correlation coefficients for the images extracted with optimized 8 wavelengths (as compared to the images extracted using the full 61-wavelength set) were 0.98, 0.96, and 0.95 for the normal, DCIS, and IDC margins, respectively. The correlation coefficients for the evenly spaced 8 wavelengths were 0.77, 0.81, and 0.53. Histograms are shown in (d), (h), and (l) to compare the extracted $[\beta c]/\langle\mu_s'\rangle$ using 61 wavelengths versus just 8 wavelengths with and without optimization. We have previously reported a threshold of 6 for the $[\beta c]/\langle\mu_s'\rangle$ ratio for classifying negative and positive margins [72]. If 98% of the pixels that make up the margins have a ratio < 6, the margin is then classified as positive. The histogram shows that with the optimized 8 wavelengths, the contrast in breast margins is preserved. Without the optimization, some contrast is lost.

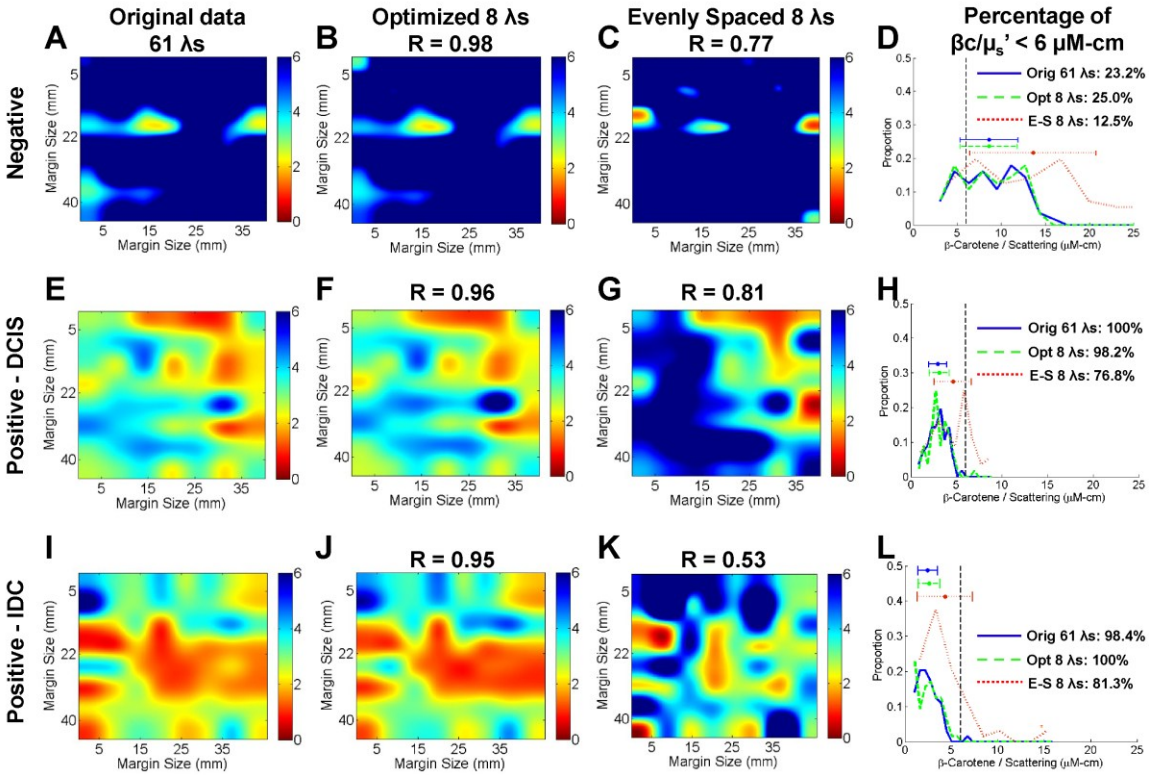

Figure 32: Representative margin maps of [βc]/<μs'> for normal (A-C), ductal carcinoma in situ (E-G), and invasive ductal carcinoma (I-K) using the full 450-600 nm spectrum, the optimized 8 wavelengths, and the un-optimized evenly spaced 8 wavelengths. Corresponding correlation coefficients for the 61-wavelength spectra and the reduced 8-wavelength spectra are shown. Distribution of the extracted βc/μs' are shown in (D), (H), and (L) for each case, along with the threshold values used in the predictive model to separate positive from negative margins.

Wilcoxon Rank Sum tests were performed to compare the Monte Carlo extracted optical properties using the full 61 and reduced wavelengths, both the optimized and evenly spaced 8. The boxplots of the comparisons are shown in Figure 33. The histologically normal samples were comprised of 320 adipose and 24 fibroglandular

samples (total N=344) compared to the 38 malignant samples. The extractions of [THb], [βc], and <μ_s'> using the optimized 8 and 61 wavelengths were not significantly different for all tissue types. The findings from an observational study on the effects of tissue heterogeneity reported by Kennedy et al. were also duplicated [47]. [THb] and <μ_s'> were both significantly increased in the malignant samples compared to the normal samples. Using the evenly spaced 8 wavelengths that were selected empirically for a previous system, the extracted <μ_s'> is most notably underestimated for malignant samples while the [THb] and the ratio [βc]/<μ_s'> are overestimated. These are consistent with the scattered plots shown in Figure 31. Without wavelength optimization, the contrast between benign and malignant samples for [THb] and <μ_s'> is not retained as wavelength numbers are reduced to 8.

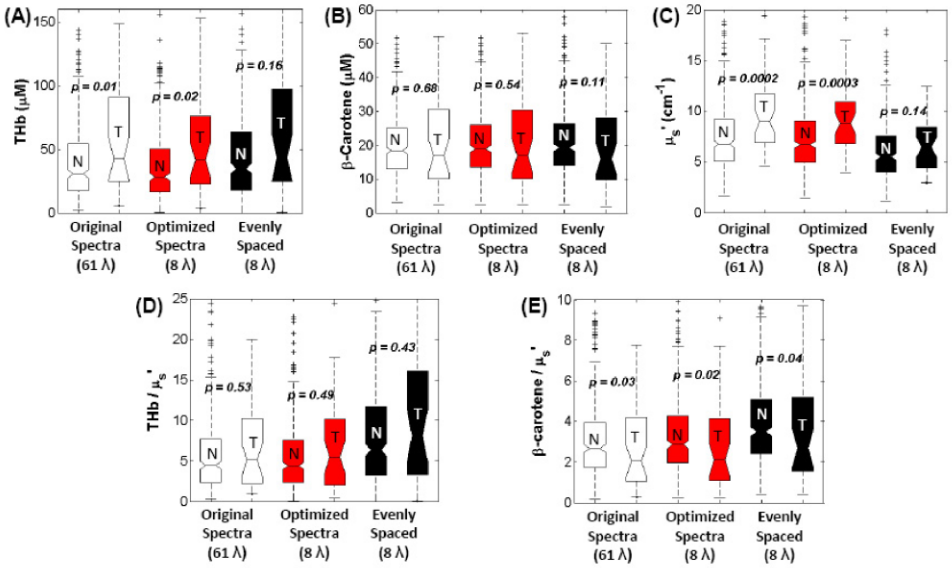

Figure 33: Comparison of the MC extractions of [THb], [βc], <μs'>, [THb]/<μs'>, and [βc]/<μs'> in normal (N) and malignant (M) tissue types using various wavelengths.

5.3.4 Wavelength optimization improves extraction accuracy in phantoms

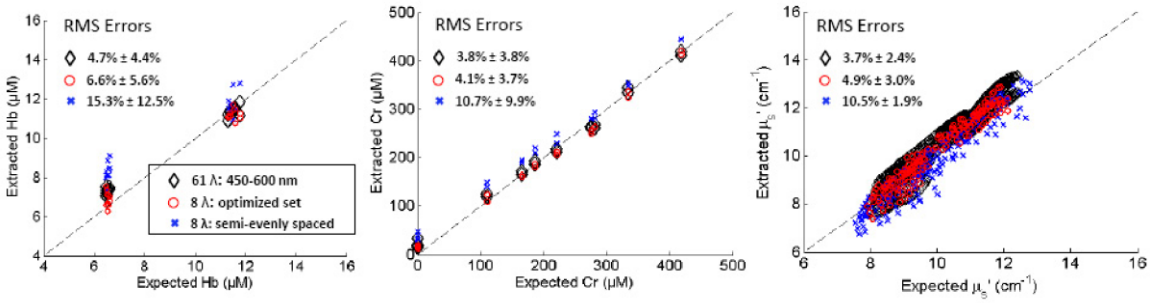

Figure 34: Comparison of extraction accuracy for [Hb], [Cr], and <μs'> using the full 450-600 nm spectrum, the optimized wavelength solution, and the evenly spaced wavelengths selected empirically for a previously reported system.

Figure 34 compares the extraction accuracy in the multi-absorber liquid phantom study using the full 450-600 nm range, the optimized wavelengths, and the evenly spaced wavelengths that were chosen empirically for a previously reported system [106]. The RMS errors for the extraction of [Hb], [Cr], and $<\mu_s'>$ using the 61 wavelengths in the 450-600 nm range were 4.7±4.4%, 3.8±3.8%, and 3.7±2.4%, respectively. However, using the 8 evenly spaced wavelengths with no optimization, the RMS errors are 15.3±12.5% for [Hb], 10.7±9.9% for [Cr], and 10.5±1.9% for $<\mu_s'>$. With the optimized 8 wavelengths, the RMS errors of extracted [Hb], [Cr], and $<\mu_s'>$ were decreased to 6.6±5.6%, 4.1±3.7%, and 4.9±3.0%, respectively. These errors are not significantly different from the errors from the full 450-600 nm spectrum. Referring back to Table 17 for an approximation of acceptable errors, these phantom results show the benefit of wavelength optimization for extracting hemoglobin and a β-carotene substitute while maintaining optical contrast, which is of utmost importance for our application.

5.4 Conclusions

Through an initial lumpectomy study discussed in Chapter 4, we found that our previously empirically selected wavelengths (400, 420, 440, 470, 500, 530, 570, 600 nm with 10 nm FWHM) were not appropriate for breast tissue spectroscopy, specifically for the accurate extraction of β-carotene content. In this chapter, a novel strategy is

presented for optimizing wavelength and bandpass choices in designing a spectral imaging system for the application of breast tumor margin assessment. In designing this more compact and cost-effective spectral imaging system for application of breast tumor margin imaging, it is important to have as few wavelengths as possible while maintaining a similarly high accuracy to the benchmark system in extracting the quantitative endpoints in breast tissue. To extract oxy- and deoxy-Hb, βc, and μ_s', the system needs at least 5 wavelengths. Any increased number of wavelengths should, in theory, improve the accuracy of the extractions as more spectral features of the reflectance measurements are captured. With simulations and previously measured *ex vivo* breast tissue data, a method of optimization that helped us systematically select appropriate wavelengths to implement was established and validated.

This method was tested in an independent breast tissue data set obtained from previous clinical studies. The appropriate number of wavelengths and the bandpass were determined systematically. Through the study, it was found that the minimum number of wavelengths to retain optical contrast obtained from a full 450-600 nm set is 8 wavelengths. Designing a system with additional wavelengths up to 12 provides minimal improvements in extraction errors at a potentially higher cost of increasing system footprint, data acquisition time, and system design complexity. Additionally, a two-absorber turbid phantom study showed the benefits of optimizing wavelength choices for the quantitation of optical properties and multiple tissue constituents.

Although this work was initially motivated by the system design for a compact, wide field spectral imaging system for margin assessment, this method has more potential in that it can provide a platform on which a variety of quantitative spectroscopic imaging instruments can use for a variety of system design processes in clinical applications beyond breast tumor margin assessment.

I would like to acknowledge the individuals who contributed to the work presented in this chapter. Quincy Brown provided guidance for the development of the wavelength selection method. The wavelength validation tissue data set was previously collected over several years by Torre Bydlon, Stephanie Kennedy, Jennifer Gallagher, and Marlee Junker.

6. A portable, wide field quantitative spectral imaging device for breast tumor margin assessment

In this chapter, we combine all of the fundamental concepts described in the previous chapters. We designed and tested a 16-channel portable spectral imaging system for breast tumor margin assessment. The system's performance metrics were compared with our previous fiber optics based clinical systems.

6.1 Introduction

In parallel to the clinical testing and validation of the 8CH system, our group has also developed a sophisticated 49-channel fiber optics based imaging system (49CH) to meet the stringent demands of intra-operative breast tumor margin assessment, specifically the coverage of approximately 20 cm^2 for several margins in under 20 minutes [115]. The basic components of this system are similar to the 1CH and 8CH clinical systems we have previously used for studies in breast cancer diagnostics and tumor margin assessment [70, 72]. A schematic of the 49CH system is shown in Figure 35. This wide field spectral imaging system consists of a 300W xenon lamp, a house-made optical switch, a custom built 49-channel imaging probe, an imaging spectrograph (Shamrock, Andor Technology), and a 512x512 CCD camera. At the common end, the 49 channels are arranged in a 7x7 array, covering an area of 4.2x4.2 cm^2. Each channel has a single 200-μm collection fiber surrounded by a ring of 8 illumation fibers with the same diameters.

We have innovatively doubled the number of channels that can be imaged by dividing these 49 channels into 2 sets: the odd (red) channels and the even (blue) channels illustrated in Figure 35. The odd and even channels are turned on and off sequentially using an optical switch. The collection fibers are arranged as a linear array, alternating odd and even channels, into the imaging spectrograph. This system is currently involved in a 200-patient breast tumor margin assessment study at the Duke Ambulatory Surgery Center.

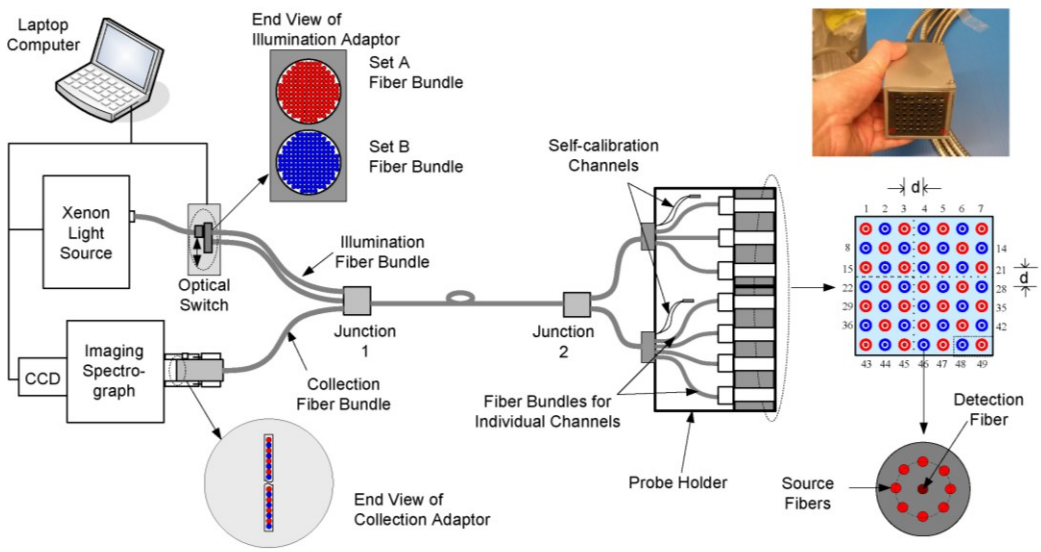

Figure 35: Schematic of the 49-channel clinical system built for intra-operative breast tumor margin assessment

Although the 49CH system is an improvement from the 8CH system, specifically with its capability of imaging 20 cm^2 at 5 mm spatial resolution in about 1 minute, this

fiber optics based system still has drawbacks in total footprint, cost, and may not be easily adaptable for everyday clinical use. First, the instrument is very heavy to move from storage to the operating room, and its footprint is about 1m x 1m x 2m. Since operating rooms are typically crowded with surgical staff and other existing instruments used for current standard of care, a more compact system is desirable. Secondly, there is an inherent problem with using fiber optic probes for wide field imaging, as discussed in the previous chapters. The total number channels in the imaging probe is limited by the size of the CCD, the magnification of the imaging spectrograph, and the fiber diameter. There is a finite number of collection fibers in the probe that can be imaged onto the CCD, which ultimately affects resolution and coverage. It was a challenging task to scale from 8-channels to 49-channels, and the end result was a very heavy and unwieldy imaging probe (>1 kg) for the operator to handle. The weight of the probe may or may not change reflectance measurements on the lumpectomy specimen and adversely affect the previously discovered optical contrast that exists between normal and malignant tissues. In addition, the optical components of the system may also become misaligned during transport within the hospital building, affecting the quality of acquired data. Lastly, the system, including the source, fiber optic probe, and detection equipment, is costly at over $55,000. While it has shown promise for margin assessment, there are pragmatic improvements to be made for wide field diffuse reflectance spectral imaging to be translatable for clinical use.

In this chapter, I discuss how we have combined the technical aspects from the system iterations described in the previous chapters and built a portable quantitative spectral imaging system (16PD) with great potential for breast tumor margin assessment. This system was tested in liquid phantoms, porcine tissues, and human breast tissues, and the system performance was compared to the 8CH and 49CH clinical systems.

6.2 Materials and methods

6.2.1 Instrumentation Description

The 16PD spectral imaging system consists of a 350W xenon arc lamp (MAX-302, Asahi Spectra), a built-in 8-slot filter wheel with wavelengths at 470, 480, 490, 500, 510, 560, 580, and 600 nm, each with a 10 nm FWHM, a 16 pixel imaging array comprised of customized annular photodiodes fabricated in-house, a 5.2 mm diameter hybrid light guide with 0.57 numerical aperture, a quartz light delivery tube, a custom 8-channel integrating transimpedance amplifier (ITIA) circuit with a switch box, a and data acquisition card. Dhar et al. have previously reported fabrication process, optimization, and testing of the annular photodiode array [107]. Each photodiode in the array had a 2.5 mm outer diameter with a 0.75 mm diameter central aperture, which was fabricated to achieve a sensing depth of 0.4-1.9 mm for margin assessment [114]. The center-to-center spacing of the pixels was 4.5 mm, which was designed to minimize optical

crosstalk while improving spatial resolution based on previous studies [105, 108]. The system schematic and photographs are shown in Figure 36.

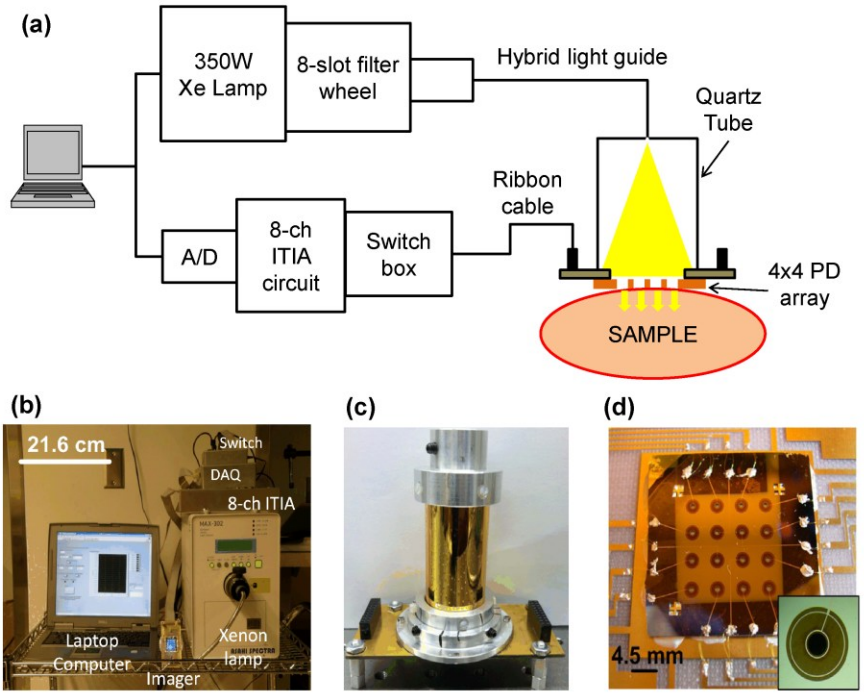

Figure 36: (a) Schematic and (b) photograph of the wide field spectral imaging system, along with photographs of the (c) quartz illumination tube and (d) the 4x4 custom annular photodiode array.

The 8 wavelengths of light were chosen based on the output of the optimization algorithm and selection validation discussed previously [116]. The discrete wavelengths from the light guide are delivered to each central aperture via free space in a quartz illumination tube optimized in length (70 mm) and diameter (27 mm I.D.; 30 mm O.D.) to ensure sufficient power throughput out of the photodiode apertures while

maintaining uniformity across corner and center pixels. The design of the tube was simulated with a ray tracing software (ZEMAX®, Radiant Zemax, LLC) and experimentally validated [117].

Although free space illumination is the simplest way of delivering light through the apertures, it is not the most efficient method. Thus, a critical improvement in this iteration of system development is the addition of 8 parallel ITIA circuits, which were built using commercial parts. A digitally controlled switch box was used to connect the 8 ITIA circuits to the 16 pixels. A microcontroller was used to control the ITIA operation and to interface with the data acquisition card and laptop computer. The ITIA circuits were programmed for various integration times: 10, 25, 50, 75, and 100 ms. The circuits achieve an SNR of greater than 55 dB for currents greater than 4 nA with 100 ms integration time. The amplifiers from our previous systems [105, 108] were only able to read down to as low as tens of nA. In addition the entire interface system, including the ITIA circuits, switch box, and data acquisition, is smaller than the light source, which helps with the portability of this system.

6.2.2 System validation in liquid phantoms

We created 12 tissue-mimicking liquid phantoms to validate the extraction accuracy of this system. The phantoms consisted of human methemoglobin (M7516, Sigma Co.) as the absorber and 1-micron polystyrene spheres (07310-15, Polysciences, Inc.) as the scatterer. Based on our previously acquired *ex vivo* breast tissue reflectance

data [118], these 12 phantoms were created to span the 25th – 75th percentiles of average absorption and reduced scattering coefficients observed in breast tissue (μ_a=2.0–5.8 cm^{-1}, μ_s'=2.9–7.1 cm^{-1}, averaged for the 8 wavelengths spanning 470-600 nm). The optical properties are listed in Table 18.

Table 18: Average optical properties for tissue phantoms.

Phantom	Avg μ_a (cm^{-1})	Avg μ_s' (cm^{-1})	Hb (μM)
1	2.0	7.1	33.0
2	2.4	6.7	38.9
3	2.7	6.3	44.1
4	3.0	6.0	48.9
5	3.5	5.4	56.9
6	3.9	5.0	63.6
7	4.3	4.6	69.3
8	4.7	4.1	76.3
9	5.0	3.7	81.9
10	5.4	3.4	86.6
11	5.6	3.1	90.5
12	5.8	2.9	93.8

For each phantom, 10 scans of diffuse reflectance measurements were recorded and averaged at each of the 8 wavelengths. A background measurement in which no light from the source exits the apertures was also taken and subtracted from the reflectance signal. For the first 6 phantoms, the integration time was 10 ms, and for phantoms 7-12, the integration time was 100 ms. The integration times were selected such that the reflectance signal is maximized but not saturated on the detector. A background measurement was also taken for each phantom in which the imaging The

diffuse reflectance spectra were corrected for the wavelength-dependent system response and the day-to-day variation of the instrument by normalizing to a Spectralon 20% reflectance standard (SRS-20-010, Labsphere, Inc.). The inverse Monte Carlo reflectance model was then used to extract the absorption and reduced scattering coefficients to compare the expected and the extracted values from these phantoms.

6.2.3 Spectral imaging of porcine tissue

To assess the feasibility of replacing the more complex and unwieldy fiber optics based 49CH system with the 16PD system, we performed spectral imaging using both instruments to target 2 samples of porcine tissue shown in Figure 37. One placement of the 49CH imaging probe was compared to four separate placements of the 16PD probe. First, the 49CH imaging probe was used to collect diffuse reflectance from one sample. Green ink was used to mark the porcine tissue at each corner of the 49CH imaging probe. Next, the 16PD probe was used to image one quadrant of the area sampled previously by the 49CH probe. Light exiting the apertures of the photodiode array was also used to help guide the probe placement in the quadrant. Reflectance measurements were taken at 25 ms, which was the longest integration time that did not result in a saturated signal for these samples. 10 reflectance measurements were taken at each of the 8 wavelengths. The procedure is repeated for all 4 quadrants until the initial area imaged by the 49CH system has been covered by the 16PD system. As done previously, the diffuse reflectance spectra were corrected for the wavelength-dependent system

response and the day-to-day variation of the instrument by normalizing to the same reflectance standard used in the liquid phantom experiment.

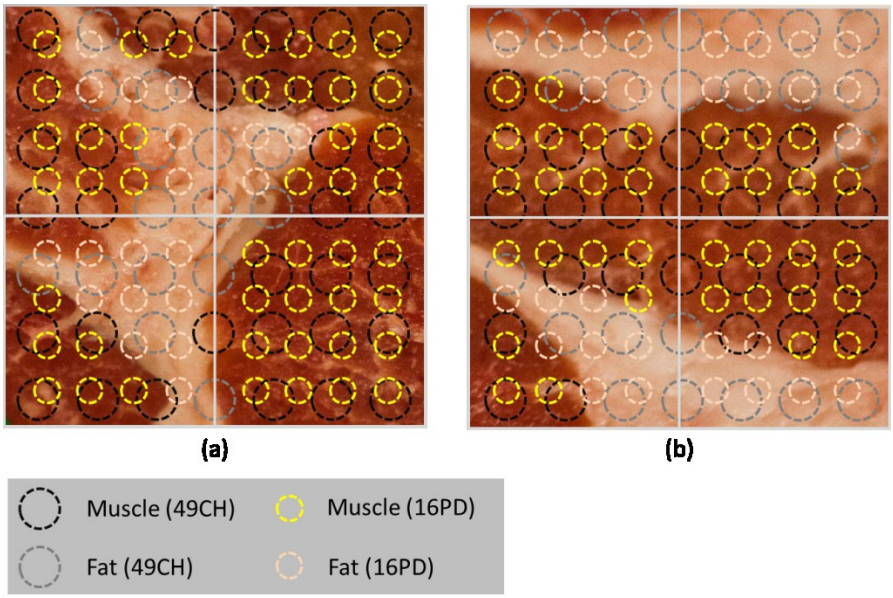

Figure 37: Photographs of (a) porcine tissue sample 1 and (b) sample 2 with the layout of the individual channel placements of the 49CH fiber based system and the 16PD system. Each channel is also classified as muscle or fat based on the legend provided.

Photographs were taken with a professional grade digital camera (5D Mark II, Canon) with a 90 mm macro lens directly above the porcine tissue samples to avoid chromatic aberrations and to ensure accuracy in coregistering reflectance measurements from both systems. As shown in Figure 37, the images were separated by 49CH and 16PD pixel location and tissue types: muscle and fat. The inverse Monte Carlo reflectance model was used to extract absorption and reduced scattering coefficients

from the tissue samples measured by both instruments. Wilcoxon Rank Sum tests were performed to compare the extracted optical properties of classified muscle and fat sites.

6.2.4 Spectral imaging of *ex vivo* breast tissue

A Duke Institutional Review Board approved clinical study (protocol ID: Pro00028284) for the development of a noval optical spectral imaging system for imaging breast tissue is currently underway. This dissertation reports on the pilot study involving breast reduction surgeries. The goal of the initial study was to determine the throughput-related performance metrics of the 16PD system compared to the 49CH system, as well as the imaging speed and the extraction of tissue parameters.

During bilateral breast reduction surgery, numerous pieces of excessive breast tissue of various sizes are removed from the patient. In this particular study, the 49CH imaging area was larger than all of the available specimens. Diffuse reflectance was measured with the 49CH system first. Next, the 16PD imaging probe was placed approximately at the center of the specimen as shown in Figure 38. 10 measurements of diffuse reflectance were taken at each of the 8 wavelengths. To investigate the effect of using various integration times, we repeated reflectance measurements at 25 ms, 50 ms, 75 ms, and 100 ms. Once the imaging probe was placed in contact with the tissue, it was never picked back up or moved throughout the course of the testing. Again, the diffuse reflectance spectra were corrected for system response and the daily variations of the instrument by normalizing to a 20% reflectance standard.

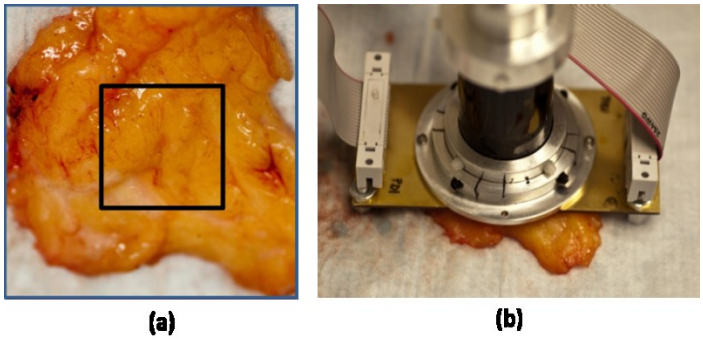

Figure 38: Photographs of (a) mammoplasty specimen with 49CH placement designated by outer blue box and approximated 16PD probe placement designed by inner black box, and (b) the 16PD imaging probe in contact with the specimen.

The inverse Monte Carlo reflectance model was used to extract absorption and reduced scattering coefficients, along with THb and β-carotene from the tissue samples measured by both instruments. In this study, there was no attempt at coregistering the 49CH and 16PD measurements so we were only able to do a qualitative analysis of the data. To analyze the differences between the extracted parameters using the various integration times of the 16PD system, Pearson's correlation coefficients were calculated.

6.3 Results

6.3.1 Extraction of phantom optical properties

Reflectance measurements were made in a series of tissue-mimicking liquid phantoms, and the inverse Monte Carlo reflectance model was used to extract the phantom optical properties. This study served two purposes: (1) to assess the optical

property extraction accuracy of the system, and (2) to identify a phantom that can be used as a reference for the inverse Monte Carlo model to calculate tissue optical properties from biological tissues [49]. We calculated the system SNR of each wavelength from each channel in the liquid phantom study. SNR_λ was defined as $20*\log(I_{avg,\lambda} / \sigma_\lambda)$, where I is the photocurrent generated by the collected reflectance signal and σ is the standard deviation of the intensity obtained for 10 repeated measurements.

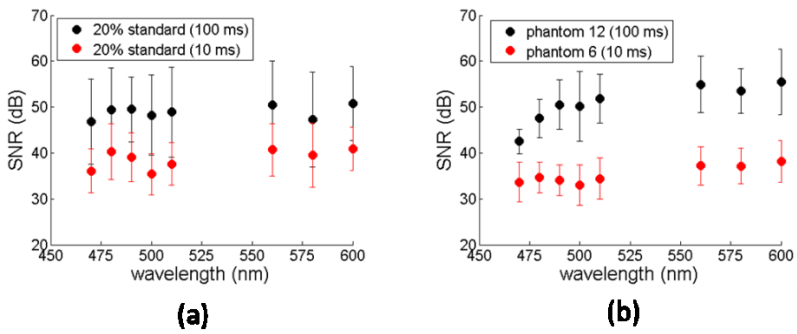

Figure 39: Calculated SNR for (a) reflectance measured from a 20% standard using 100 ms and 10 ms integration times and (b) reflectance measured for the most absorbing phantoms using 100 ms and 10 ms integration times for all 8 wavelengths. The error bars are the SNR standard deviation for all 16 pixels on the imaging probe.

Figure 39 shows the calculated SNR for the imaging system measuring (a) 20% reflectance standard using 100 and 10 ms integration times and (b) in the most absorbing phantoms (average μ_a = 3.8 cm^{-1} for 10 ms and 5.6 cm^{-1} for 100 ms), representing the worst case scenario for SNR in this particular set of phantoms. The averaged SNR for all wavelengths and all pixels is 48.9±1.4 dB and 38.7 ±2.1 dB for the

100 and 10 ms integration times, respectively. In the highly absorbing phantoms relative to the integration times, the average SNR was 50.8±4.3 dB for 100 ms and 35.3±1.9 dB for 10 ms.

Reflectance measurements were made in a series of tissue-mimicking liquid phantoms, and the inverse Monte Carlo reflectance model was used to extract the phantom optical properties. This study served two purposes: (1) to assess the optical property extraction accuracy of the system, and (2) to identify a tissue-mimicking phantom that can be used as a reference to calibrate the modeled reflectance spectra in the Monte Carlo model, accounting for the throughput and wavelength response of the system and correcting for differences in the magnitude between the MC simulations and the experimental measurements on biological tissue.

Table 19 lists the average extracted μ_a and μ_s' errors across all 16 pixels. The phantom number denotes the one was used as a reference to extract the optical properties from all other target phantoms. For instance, when phantom 1 was used as a reference phantom to extract phantoms 2-12, the averaged extracted absorption error was 11.0 ± 6.8%, and the averaged extracted scattering error was 7.7 ± 3.6%. At the time of this phantom experiment, the only available integration times programmed for the ITIA circuits were 10 ms and 100 ms. The 10 ms integration time was only used for the high scattering, low absorbing phantoms because the signals were saturated at 100 ms integration time. We discovered that the extraction accuracy is generally worse when a

10 ms phantom is used as a reference. This can be attributed to the lower SNR, especially at the highly absorbing phantoms (thus less diffuse reflectance signal), particularly phantoms 5 and 6, which have the highest extracted errors and widest range of standard deviations for all pixels.

Table 19: Extracted absorption and scattering errors averaged across all pixels. The shaded region indicates the phantoms measured with 10 ms integration time. The unshaded region include the phantoms measured with 100 ms integration time.

Phantom	Avg μ_a error	Avg μ_s' error
1	11.0 ± 6.8	7.7 ± 3.6
2	16.2 ± 11.6	9.7 ± 8.1
3	17.4 ± 14.8	9.2 ± 6.7
4	15.3 ± 9.7	5.5 ± 2.8
5	25.6 ± 10.1	10.4 ± 6.2
6	30.4 ± 23.4	5.2 ± 4.2
7	7.5 ± 5.7	8.4 ± 8.0
8	6.4 ± 4.5	8.2 ± 7.6
9	10.6 ± 6.8	8.5 ± 5.0
10	7.5 ± 6.1	3.3 ± 2.2
11	10.4 ± 8.7	3.5 ± 2.1
12	12.5 ± 10.6	4.6 ± 2.8

Table 20 breaks down the extraction errors by pixels. The extraction error percentages generally appear higher for phantoms measured with 10 ms integration. However, it is also important to note that while the percentages appear higher, the absolute extracted values are generally only fractions of a cm^{-1} away from the expected. The errors appear higher partly because the expected absorption values for the least absorbing phantoms are low. As shown in Figure 40, the system is capable of extracting

absorption and reduced scattering coefficients very well with some variations between pixels. The correlation coefficients are 0.98 and 0.99 for the mean extracted μ_a and μ_s', respectively. Phantom #10 was chosen as the reference phantom for the subsequent tissue studies because it has the lowest absorption and scattering extraction errors.

Table 20: Extracted absorption and scattering errors for each pixel averaged across all phantoms. The 10 ms columns lists the errors when using reference phantoms 1-6; the 100 ms columns shows the errors when using references 7-12.

Pixel	10 ms		100 ms	
	Avg μ_a error	Avg μ_s' error	Avg μ_a error	Avg μ_s' error
1	14.7 ± 11.4	2.8 ± 2.5	6.1 ± 6.3	1.9 ± 2.2
2	14.5 ± 15.1	4.9 ± 4.1	7.7 ± 5.4	1.6 ± 3.7
3	12.8 ± 9.7	5.0 ± 5.4	7.0 ± 4.9	0.9 ± 0.8
4	17.9 ± 13.1	9.3 ± 5.4	7.1 ± 7.1	0.9 ± 0.4
5	21.5 ± 20.1	3.3 ± 2.7	8.1 ± 6.6	3.0 ± 4.8
6	24.3 ± 20.1	5.8 ± 5.4	7.8 ± 6.3	3.5 ± 4.9
7	16.6 ± 14.6	8.1 ± 5.9	10.4 ± 8.4	1.2 ± 0.8
8	15.5 ± 13.0	5.8 ± 4.4	6.3 ± 5.5	1.1 ± 0.8
9	17.5 ± 18.7	3.9 ± 2.9	7.5 ± 5.4	2.5 ± 2.1
10	14.4 ± 11.9	4.4 ± 3.3	6.2 ± 5.4	2.0 ± 1.6
11	12.8 ± 10.6	8.4 ± 5.1	8.6 ± 6.8	1.2 ± 0.8
12	11.9 ± 12.3	2.6 ± 1.7	7.6 ± 7.7	1.9 ± 1.0
13	14.3 ± 12.7	3.0 ± 1.6	5.6 ± 4.5	2.1 ± 1.8
14	9.7 ± 7.8	9.1 ± 5.0	7.5 ± 6.9	2.7 ± 1.8
15	12.3 ± 11.1	6.1 ± 4.0	6.9 ± 6.8	3.1 ± 2.9
16	13.5 ± 15.1	2.8 ± 1.8	8.7 ± 8.9	3.8 ± 2.3

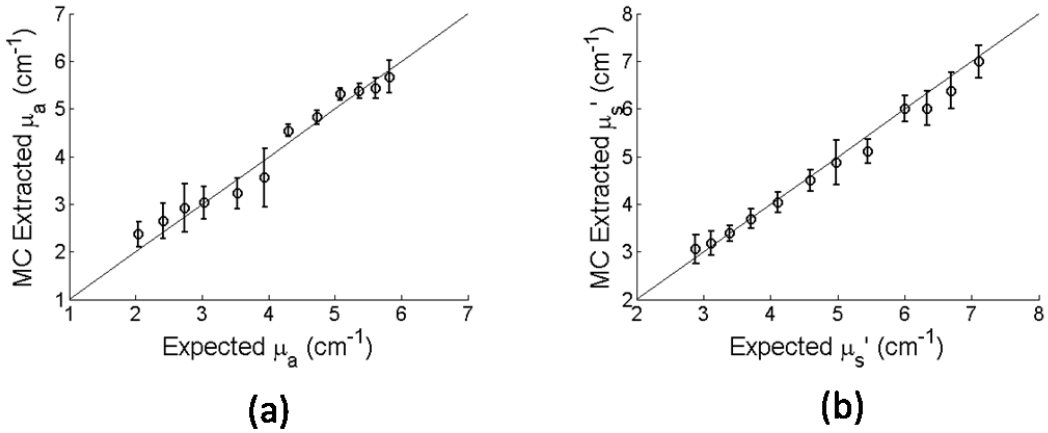

Figure 40: Monte Carlo extraction accuracy for the (a) absorption coefficients and (b) reduced scattering coefficients averaged over all wavelengths and all pixels.

6.3.2 Comparison of 49CH and 16PD spectral imaging systems on porcine tissue

A qualitative comparison of THb and μ_s' extraction between the 49CH and 16PD spectral imaging systems was conducted using 2 samples of porcine tissue. With 4 placements of the 16PD probe in the quadrants of the area equivalent to the 49CH probe face, tissue composition maps were reconstructed and are shown in Figure 41. Although the extracted numbers between the 49CH and 16PD systems are not coregistered because the channel-to-channel spacings are different for each system, the extracted hemoglobin and scattering values of both systems are very similar, with most pixels of THb ranging from 10-50 μM and average μ_s' ranging from 5-30 cm^{-1} for both systems. The distinct features of fat shown in the photographs match up with higher extracted

scattering values while the distinctly darker, red features of muscle correspond to higher THb extractions.

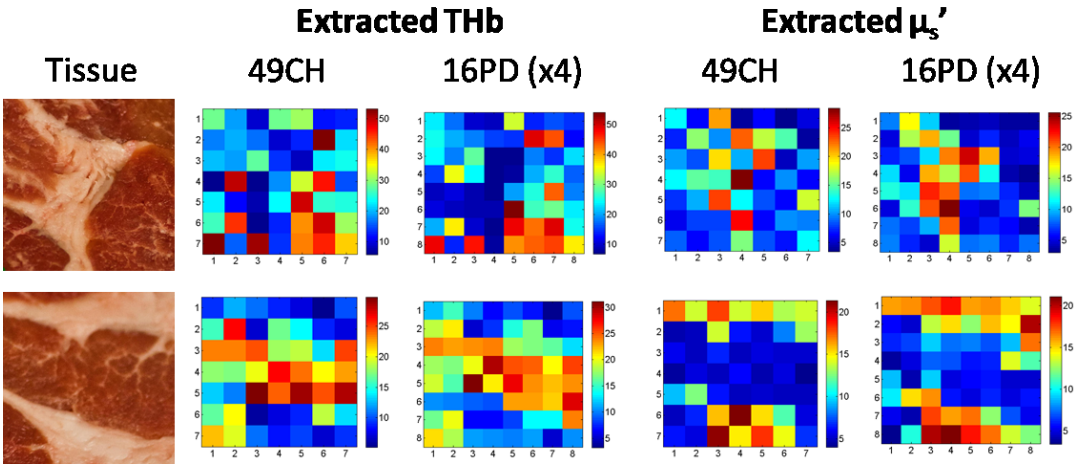

Figure 41: Comparison of 49CH and 16PD extractions of THb and average μs' on 2 different porcine tissue samples.

After manually classifying and separating the fat sites and the muscle sites as shown in Figure 37 and combining the data of both tissue samples, Wilcoxan Rank Sum tests were performed to compare the extracted optical properties of the classified sites. Boxplots separated by fat sites and muscle sites for the extracted total hemoglobin and average reduced scattering coefficients are shown in Figure 42. Both the extracted hemoglobin and reduced scattering values in fat are significantly different from those extracted in the muscle, with p-values much less than 0.0001. This was a trivial finding because even without optical spectroscopy and the inverse Monte Carlo model, we are able to clearly see the significant contrast between the fat and muscle sites. Nonetheless,

the porcine tissue experiment showed that the 16PD is able to extract similar optical properties as the 49CH system.

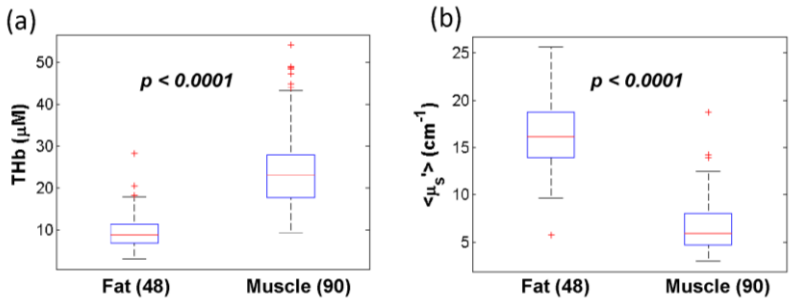

Figure 42: Boxplots separated by fat sites and muscle sites for the extracted (a) total hemoglobin and (b) average reduced scattering coefficients from the 16PD measured diffuse reflectance spectra.

6.3.3 Imaging of reduction mammoplasty specimen

Specimens from a breast reduction surgery were obtained and imaged with the 49CH system. Due to space and time constraints in the operating room, we were unable to have both instruments in the operating room simultaneously. The 49CH system was first brought into the operating room and used to image several reduction mammoplasty specimens. After the 49CH system was taken out of the operating room, the 16PD system was wheeled in approximately 5 minutes later. Reflectance measurements were made by placing the 16PD imaging probe at approximately the center of the 49CH probe area on the tissue. The tissue composition map extracted using the 49CH system is shown in Figure 43. The approximated probe placement of the 16PD

system is shown as a dotted square on the maps. We only use this to qualitatively determine whether the extracted values for the 16PD system are reasonable because there is no coregistration of the 2 systems.

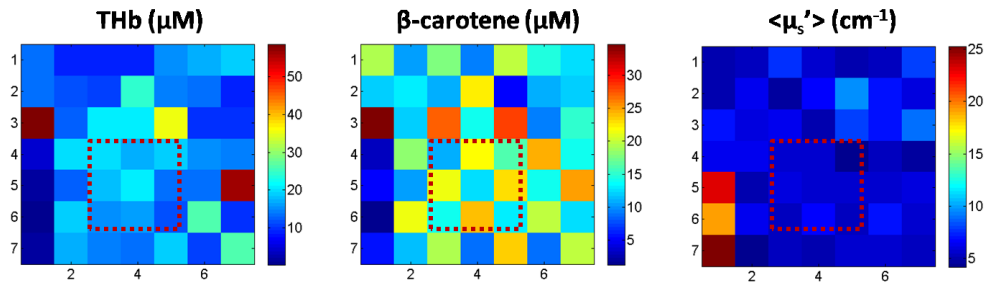

Figure 43: Extracted tissue composition maps of THb, β-carotene, and <μ_s'> obtained with the 49CH system. The approximated area of the 16PD probe is shown as a dotted square on the tissue composition maps.

The primary goal of this particular experiment was to determine whether using different integration times will have an effect on the extracted parameters. In addition, we tested the system for SNR and speed in a realistic, clinical environment with *ex vivo* breast tissue to assess the feasibility of using this design for margin assessment in the future. In this study, we were only able to use 3 integration times: 25, 50, and 75 ms. The reflectance signal was saturated at 100 ms. The inverse Monte Carlo model was used to extract tissue parameters, and the extractions were compared for the 3 integration times. The wavelength-averaged SNR for all pixels were 34±5, 38±8, and 40±5 dB for 25, 50, and 75 ms integration times, respectively. Because the system speed is currently limited by the mechanical rotation of the filter wheel, the increases in

integration times on the order of tens of milliseconds are negligible. However, in future design iterations that may not involve a filter wheel, the integration time and acquisition speed could play a larger role. For this system, it takes approximately 45 seconds to 1 minute to scan through the 8 wavelengths while taking 10 repeated measurements at each wavelength.

Shown in Figure 44, tissue composition maps of total hemoglobin, β-carotene content, and average reduced scattering coefficients are extracted for 25, 50, and 75 ms. Pearson's correlation coefficients are calculated to compare the extracted maps of 75 ms to 50 ms (R_1) and 75 ms to 25 ms (R_2) with the assumption that the most accurate extractions are performed when SNR is highest. The correlation coefficients R_1 and R_2 for extraction of THb were 0.96 and 0.81, respectively. For the extraction of β-carotene, R_1 and R_2 were 0.88 and 0.49, respectively. For the extraction of reduced scattering coefficients, R_1 was 0.94, and R_2 was 0.78. This shows that the 25 ms integration time is not likely a good setting to use for accurate tissue extractions. There is no significant difference between using 50 ms and 75 ms. This finding, along with the effect of various probe pressure on the tissues, will be the focus of a future comprehensive study. Finally, a qualitative comparison of the tissue composition maps obtained with the 16PD and 49CH systems (Figure 43 and Figure 44) show that all 3 of the extracted parameters are reasonably close. Furthermore, we discovered that the extracted β-carotene range is now very reasonable with the implementation of the optimized wavelengths as opposed

to the extractions done in a prior study described in Chapter 4, in which β-carotene was extracted outside of the expected range.

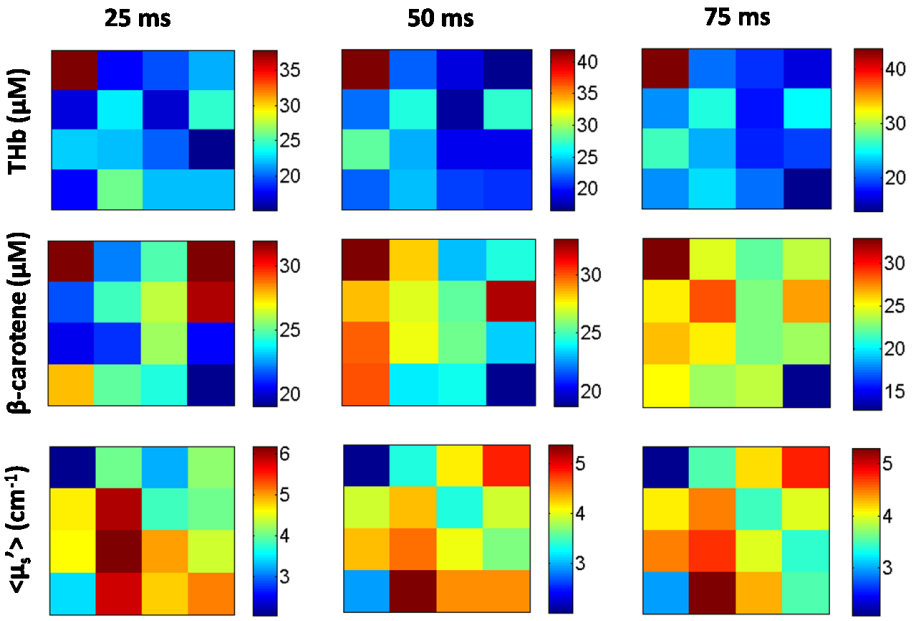

Figure 44: Extracted tissue composition maps of THb, β-carotene, and <μs'> obtained with 25, 50, and 75 ms integration times.

6.4 Conclusions

In summary, there are stringent requirements in the intra-operative setting for breast tumor margin assessment, such as time, space, and speed for the diagnosis, which is directly related to margin coverage. To meet these demands, we have developed a diffuse reflectance imaging system for the application of breast tumor margin assessment by redesigning our previously reported fiber based optical systems, 1CH, 8CH, and 49CH. Specifically, we have replaced the CCD and imaging spectrograph

with an array of annular photodiodes. Instead of using fibers or fiber bundles to illuminate each tissue site by contact imaging, our system collects diffuse reflectance with photodiodes at the tissue surface. As pixel resolution decreases and imaging area increases, imaging the tumor margins with optical fibers becomes extremely unwieldy as we have done with the 49CH system.

Table 21: Comparison of 8CH, 49CH, and 16PD system specifications related to the requirements of tumor margin assessment.

System	Coverage per scan	Spatial resolution	Time to image 20cm² @ 5mm resolution	Cross talk	Avg phantom errors		SNR (dB)
					μ_a	μ_s'	
8CH	3.8 cm²	10 mm	8 minutes	>10%	13.3%	3.3%	46
49CH	17 cm²	6 mm	1 minute	2.4%	5.3%	4.5%	45
16PD	2.6 cm²	4.5 mm	5 minutes	<10%	7.5%	3.3%	51

Table 21 summarizes some of the improvements of the 49CH system over the 8CH fiber based system for breast tumor margin assessment and provides a glimpse of the current state of the 16PD system with more developments to be made in the future. Specifically, the 49CH system covers a much larger area than the 8CH and 16PD systems at a faster time. The 16PD system has the best spatial resolution of the 3 systems and highest SNR. Although the photodiode based imaging system is not able to survey the entire margin of a typical size in just one probe placement, the photodiode array provides a proof of principle on the ease of scalability for future iterations of system development. In this chapter, we have shown that the 16PD system is comparable to the

much more complex and costly fiber optics based 8CH and 49CH systems, specifically for quantifying optical properties in phantoms and biological tissues.

Currently, the only limitations for the 16PD to be an effective tool for intra-operative margin assessment are its easily scalable coverage area and the time required for the filter wheel to sequentially scan through the 8 wavelengths. Our group is continuing to work on further miniaturizing an imaging device based on an LED-photodiode array design. This would obviate the slow mechanical movement of the filter wheel and decrease the data acquisition time tremendously. Furthermore, the device would be even more portable and inexpensive, with great potential for quick clinical translation and expansion for other biomedical applications.

I would like to acknowledge Sulochana Dhar for assisting with all of the phantom experiments and clinical studies presented in this chapter. In addition, Christine Mulvey and Marlee Junker performed the porcine tissue measurements and *ex vivo* lumpectomy tissue measurements with the 49CH.

7. Conclusions and future directions

This chapter summarizes the work completed throughout the course of this thesis and the conclusions drawn from these experiments. A brief report of ongoing work and suggestions of potential future studies to extend the work are also presented.

7.1 Conclusions

This dissertation presented the iterative design, engineering, and validation of a wide field spectral imaging system that utilizes the similar scientific principles as our previous 1CH, 8CH, and 49CH fiber optics based clinical instruments for the application of breast tumor margin assessment. Although these previous fiber based systems have shown great potential for identifying malignancies in breast tissues and can be expanded for use in margin assessment, they suffer from several limitations such as footprint, cost, and scalability in terms of coverage area, pixel density, and resolution. With a complete redesigning of the previous systems, we have worked towards developing an intra-operative margin assessment device that will be capable of surveying all 6 margins up to 20 cm^2 at mm resolution in under 20 minutes while providing accurate, diagnostic tissue composition maps for the surgeon.

To reduce the footprint of the system as well as provide a simpler and more cost-effective way to scale single-point probes to an imaging array, we implemented silicon photodiodes as the system detectors, replacing the sophisticated, expensive 2D CCD and

imaging spectrograph. In the initial system design iteration, we showed proof-of-principle by designing, building, and testing a hybrid optical device that consisted of an optical fiber for illumination and an annular photodiode for detection. This single-pixel system was comparable to the 1CH clinical system in optical properties extraction accuracy, in throughput-related parameters, and in tissue sensing depth, which are all essential for our goal of tumor margin assessment.

After showing that a hybrid system with optical fibers for illumination and photodiodes for detection can be used to quantify optical properties, we iterated on a subsequent system design with the goal of obviating the need for illumination fibers and developed a 16-channel imaging probe that used 8 discrete wavelengths (400, 420, 440, 470, 500, 530, 570, and 600 nm, each with a 10 nm FWHM) by free-space illumination through the central apertures of a customized photodiode array fabricated in-house. Although the fabrication process of the 4x4 photodiode array did not have 100% yield, the system was tested in tissue-simulating phantoms, and we extracted μ_a and μ_s' with 85-92% accuracy for the functional pixels. For the first time, our DRS imaging system was tested in a murine tumor model and in an initial *ex vivo* lumpectomy tissue sample from a BCS. patient In the murine study, a commercial spectrofluorometer and the PD-based imaging system were used to measure a tumor site and a normal site on the flanks of the animals. The extracted parameters (THb and μ_s') using both systems were within 10% of each other, which further provided evidence that a PD-based imaging system

with only 8 discrete wavelengths can indeed replace a more complex fiber based imaging system. In the human breast tissue study, however, we discovered that while the system SNR is sufficiently high compared to previous fiber-based systems (>40 dB), the total β-carotene content was significantly over-estimated compared to the range of values we have seen in previous studies. Because the *ex vivo* breast tissue contains additional absorbers, such as Lymphazurin™ (a contrast agent used for the delineation of lymphatic vessels during surgery) and β-carotene, not seen in our validation liquid phantoms, the 8 semi-evenly spaced wavelengths empirically chosen in the initial system development were not optimized for our specific application of breast tumor margin assessment. Since the ratio of β-carotene to scattering is an important diagnostic parameter for differentiating malignant from benign tissues, this motivated the subsequent work to optimize the selection of wavelengths.

We then developed a wavelength selection method that combines the inverse Monte Carlo reflectance model with a genetic algorithm for global optimization. The method is optimized for the very specific extraction of total hemoglobin content, β-carotene content, and tissue scattering properties, which have been reported to be significant parameters for determining tumor margin status. It was designed for a wide range of tissue optical properties obtained from previously measured reflectance spectra of *ex vivo* breast tissue specimens. Validation of the newly optimized wavelengths (470, 480, 490, 500, 510, 560, 580, and 600 nm) was performed on an independent set of breast

tissue spectra. With the 8 wavelengths, we are able to extract THb, β-carotene, and scattering with 12% error compared to the extractions of the full 450-600 nm spectrum of the 8CH clinical system. We also determined that each discrete wavelength must not exceed 10 nm FWHM to maintain a similar accuracy, which ultimately helps retain optical contrast in the malignant and benign breast tissues. The wavelength optimization method can also be useful for the DRS imaging system design in other clinical applications as long as known and well-defined absorption and scattering properties in the tissue of interest are available to the user.

The final iteration of system design presented in this dissertation is a 16-channel PD-based imaging system with better detector responsivity, lower dark current, 100% detector yield, improved current amplifiers, and utilized the optimized wavelengths. The illumination strategy was also slightly modified so that the photons exiting through the aperture into the tissues can be more accurately modeled with less optical crosstalk, thus making the inverse Monte Carlo model more robust. The system was tested in a series of liquid phantom experiments and had superior performance in the extraction of phantom optical properties compared to the 8CH clinical system (average extraction errors of 7.5% vs. 13.3% for μ_a and equivalent for μ_s' at 3.3%) and comparable performance to the 49CH clinical system (average extraction errors of 7.5% vs. 5.3% for μ_a and 3.3% vs. 4.5% error for μ_s').

A side-by-side comparison between the 49CH system and the new PD-based imaging system were made for SNR, speed, size, and extraction of composition maps in porcine tissues and human breast tissues. Although the systems have comparable SNR, the PD-based imaging system is much more portable compared to the 49CH system. The imaging probe is also only essentially the weight of a printed circuit board while the 49CH probe is approximately 1 kg. Currently, it takes 45 seconds to 1 minute (limited by the mechanical rotation of the filter wheel to scan 8 wavelengths) for the PD-based system to acquire the reflectance spectra in a sample. Furthermore, the 49CH system covers approximately 4 times more area at less than a quarter of the time. Because the channel-to-channel spacing between these two systems is not identical, it is difficult to co-register the reflectance measurements in tissues using both systems. Nonetheless, we were able to qualitatively show very similar tissue composition maps using both systems in porcine and human tissue samples. Although the 16-channel PD-based imaging system does not currently image tumor margins as quickly as the 49CH clinical system due to smaller size of the 16PD and the need of a mechanical filter wheel, we have provided a proof of concept design that has been validated and can be more easily scaled to larger arrays for wider coverage than the fiber optics based systems. Combined with the annular photodiode array principle and the wavelength optimization algorithm, the work presented in this dissertation has great potential for

expansion for use in other clinical applications in which rapid, wide field quantitative spectral imaging of tissue is needed.

Table 22: Comparison of parameters important to breast margin assessment for all fiber optics based clinical system and the various iterations of photodiode based systems. The shaded rows indicate the systems that have been used to obtain data from *ex vivo* human breast tissue specimens. Note that 9PD has only 8 working pixels. 16PDa has only 12 working pixels; thus, coverage per scan is only a theoretical value given that all PDs are functional.

System	Coverage per scan	Spatial resolution	Illumination	Detection	Wavelength range (nm)	Sensing depth (mm)	Avg phantom errors		SNR (dB)
							μ_a	μ_s'	
1CH	-	-	Fiber-guided	CCD/ spectrograph	400-600	0.6-1.4	9.8%	7.7%	45
8CH	3.8 cm^2	10 mm	Fiber-guided	CCD/ spectrograph	450-600	0.5-2.2	13.3%	3.3%	46
49CH	17 cm^2	6 mm	Fiber-guided	CCD/ spectrograph	450-600	0.8-2.5	5.3%	4.5%	45
1PD	-	-	Fiber-guided	Commercial Photodiode	400-600	0.4-1.7	9.8%	7.6%	60
9PD	4.6 cm^2	8 mm	Fiber-guided	Commercial Photodiodes	400-600	0.6-2.6	6.0%	11.4%	40
16PDa	2.6 cm^2	4.5 mm	Free-space	Fabricated Photodiodes	400-600	04-1.9	11.8%	11.5%	45
16PDb	2.6 cm^2	4.5 mm	Free-space	Fabricated Photodiodes	470-600	0.4-1.9	7.5%	3.3%	51

Table 22 summarizes the important metrics for the various iterations of systems developed by our group, including fiber based, photodiode based, and hybrid optical devices. The coverage and spatial resolution are important to achieve full surveillance of all tumor margins. The illumination evolved from optical fibers, which can become

unwieldy, to free-space illumination. The detection strategy changed from using expensive CCDs and imaging spectrographs to easily scalable photodiodes. The wavelength ranges are related to optical contrast in the breast (based on spectral features of hemoglobin and β-carotene), sensing depth, and also related to SNR due to the lower silicon detector responsivity at the shorter wavelengths between 400-450 nm. The average phantom errors are important in two ways. First, the numbers determine the accuracy of the respective systems in extracting optical properties in tissue-like media. Secondly, these reflectance spectra measured from the phantoms serve as a reference for the clinical measurements with unknown optical properties. Using a reference phantom that starts out with 15% error is clearly not as ideal as using a reference phantom closer to 0%. Because extraction errors propagate through clinical measurements, we strive to always use a reference phantom with low extraction errors to help preserve any potential optical contrast in the breast.

7.2 Ongoing work

There are ongoing developmental work and clinical validation studies done in parallel that are outside the scope of this dissertation. Through the NIH Bioengineering Research Partnership grant, which funded the work presented in this dissertation, we have received valuable feedback from an external advisory board consisting of experts in biophotonics, optical systems, semiconductors, and breast surgery, and we are

continuing to make progress towards the development of a fast, wide field spectral imaging system for breast tumor margin assessment.

7.2.1 Fabrication of larger photodiode arrays and new light distribution design

The 4x4 PD array presented in this dissertation provided proof of concept for an easily scalable detection strategy compared to the previous fiber optics based 1CH, 8CH, and 49CH clinical systems. The array is large enough to demonstrate coarse spectral imaging, yet small enough for simple device validation studies described in the previous chapters. With only 16 channels for collecting reflectance spectra, the data is much easier to manage, and we are better able to identify any potential problems with system during development. After we have shown the 4x4 PD imaging array has comparable performance to the fiber optics based clinical systems, our group is currently working towards fabricating an 8x8 PD array, which quadruples the imaging area to approximately 12 cm^2.

Aside from the challenges fabricating a 64-pixel array with 100% yield in house, there are additional technical issues we investigating, such as the data acquisition and the light delivery method. First, we currently utilize an 8-channel integrating transimpedance amplifier (ITIA) with a mechanical switch to read all 16 channels. It is feasible to simply build extra 8-channel amplifiers to acquire the data; however, the extra amplifier boxes are not desirable because a secondary goal is to make a smaller, more portable device. Perhaps the most challenging part of the ongoing work is the

distribution of light to the apertures of all 64 photodiodes in the array. The simple strategy of free space illumination through the back of the photodiodes will not work in a larger array as the pixels on the corners and edges would not have sufficient throughput. In collaboration with researchers at the University of Wisconsin, we are developing a planar dimpled waveguide to distribute the light evenly through all pixels in an 8x8 imaging array. We are also investigating new sources such as LEDs coupled with bandpass filters (10 nm FWHM) and laser diodes to replace the current broadband source and 8-slot filter wheel. With diodes as new sources, the speed at which reflectance measurements are acquired will undoubtedly be improved as well.

7.2.2 Automated, pressure-sensitive imaging platform

After developing several iterations of fiber optics based and photodiode based DRS systems that are capable of extracting tissue optical properties with high accuracy, we learned that one very important clinical aspect of breast tumor margin assessment is making sure that there is good data quality control in the operating room. The 8CH clinical system utilized a plexi-glass box with holes customized to the diameter of the probes for holding them in place and for co-registering reflectance measurements with site level inking and histopathological examination. It was moderately tedious but tolerable to manually position and fit 8 probes into these holes of the plexi-glass box and to keep track of the measured data. However, the progression to the 49CH system made it obvious that an automated imaging platform is required for margin assessment

studies with the 49CH fiber optics based system and any future iterations of the expanded 8x8 PD based spectral imaging system.

Compared to laboratory testing, measurements made in a clinical setting are much less controlled. First, tissue specimens are often irregularly shaped, which makes it difficult for all channels from a planar imaging probe to have good contact with the tissue. Secondly, diffuse reflectance signals will change from measurement to measurement on the same imaging sites even if the operator only slightly shakes the imaging probe. In addition, there is evidence that tissue optical properties can change depending on the pressure from the imaging probe applied to the tissue [119, 120]. For instance, the probe can compress the specimen so much that the top tissue layers are flattened several millimeters. This can be problematic especially for intra-operative margin assessment because of the requirement for a 2 mm surrounding rim of normal tissue around the tumor. If the top layer is compressed too far down, the imaging probe's effective sensing depth becomes much deeper, and the number of false positive diagnoses may increase dramatically.

We are developing an automated, pressure-sensitive imaging platform to address the issues above. The lumpectomy specimen can be placed on a plate with digital pressure sensors. A computer controlled stepper motor helps lower the imaging probe down to the specimen until a desired pressure is met. The probe is locked in place and cannot move during the measurement. We are evaluating the extraction of optical

properties for a range of probe pressures on tissue. We hypothesize that extracted optical properties will remain similar for a given range of pressures. As the outermost ~2 mm of normal tissue is compressed too much, the extracted optical properties will change. We will then be able to recommend an appropriate range of probe pressures during intra-operative margin assessment and be able to obtain better quality spectral data.

7.3 Future directions

The results of this dissertation lay the ground work for a number of future studies that can be completed to further understand the biology of breast tissue at the microscopic and macroscopic scales, and for improvements that can be made to optical imaging platforms for the purposes of breast tumor margin assessment. Because photodiode arrays can potentially be mass-produced rapidly and inexpensively, they are attractive for other important clinical applications.

7.3.1 Technical improvements

Light delivery options

We have proposed to expand the probe to an 8x8 array of photodiodes. Although we are exploring the use of a dimpled planar waveguide to direct the light through all apertures, the structure requires fine machining of the conical-deflectors that may not provide for sufficiently high throughput and SNR compared to the current free-

space illumination scheme with a smaller array. There are other more elegant light delivery options to explore. For instance, a variety of microlens arrays can be customized to distribute light evenly through all apertures. A single microlens in the array generally have a diameter of less than 1 mm and often as small as 10 microns. This is existing technology that can be incorporated to any annular photodiode array geometry at a reasonably higher cost of ~$1000 for an 8x8 microlens array. Another simpler and much less costly method is the use of LEDs in free space. For example, several modules of 8 discrete LEDs can be positioned above their respective quadrants of annular PD arrays. Because LEDs are very inexpensive, the LED modules can be multiplexed as many times as the size of the PD array requires.

Detector options

There are also improvements that can be made as we continue to develop and optimize the annular photodiode arrays. During the numerous iterations of system development, we utilized thick (2.2 mm) commercial photodiodes by drilling an aperture in the detectors to show proof of principle. When we attempted to multiplex the thick commercial photodiodes for imaging, however, free-space illumination did not provide sufficient throughput in the pixels on the edges. The fabricated arrays used in the 16PD system is only 610 microns thick, allowing for much higher throughput with less detector edge area to absorb the diverging photons through the apertures. As larger

arrays are fabricated, making the detectors even thinner would provide a similar advantage in throughput and thus SNR.

Modeling of heterogeneous turbid media

Further improvements in the light modeling and data analysis can be pursued. We determined that the wavelength-dependent reflectance in the visible spectrum can generally be detected up to approximately 2 mm from the source, depending on tissue type and probe geometry. We have designed the 8CH, 49CH, 9PD, and 16PD systems to have minimal optical crosstalk by performing forward Monte Carlo simulations of light propagation in tissue. For each of our spectral imaging systems, some optical crosstalk exists especially for adipose tissue, which is generally less absorbing than malignant tissue. Because our current inverse Monte Carlo model assumes a homogeneous medium under each individual detector channel, the contribution of optical crosstalk from any adjacent sources may ultimately lead to the inaccurate extraction of optical properties. Although Jacques and Wang's Monte Carlo model of light transport (MCML) has been the gold standard for simulations of light transport in multi-layered tissue in our field [121], it is not completely effective in the presence of 3D heterogeneity. The problem is very complex because it is difficult to determine the original source of the detected photons. Li et al. have developed a Monte Carlo model in voxelized media and applied the model to a 2-layered spherical structure with multiple inclusions of

differing optical properties [122]. For our application, there is potential to adapt a more scalable model similar to this, but the computation time will likely be exponentially higher.

In addition to continuing to model light transport with Monte Carlo, other methods can be explored, such as the diffusion equation and the radiative transfer equations central to reconstructing heterogeneities optical tomography. Andreas Hielscher has developed a finite volume algorithm for modeling light transport, which can rapidly approximate solutions to the radiative transfer equation in hetereogeneous media. Because the application for the model is optical tomography and the wavelengths used are typically in the 700-1000 nm range, more studies and modifications may be necessary for the tumor margin assessment application which requires shorter wavelengths of light in the visible range, as well as different source-detector separations.

7.3.2 Optimization of sensing depth and spatial resolution

Another improvement that can be made is to adjust the detector geometry of each channel to achieve a more appropriate sensing depth for the imaging probe. Using Monte Carlo reflectance simulations for various tissue types, we have nominally determined that the current sensing depth (defined by the depth of tissue where 90% of the detected photons have traveled) is 0.4-1.9 mm for 470-600 nm. Although 90% of the detected photons have traveled as deep as 1.9 mm into adipose tissue, the majority of

these are actually those photons that have only traveled very shallow depths into the tissue and detected by the areas of the photodiode closes to the edges of the aperture. In other words, the sensing depth defined by our previous work involving fiber optics based systems with a lower effective numerical aperture (NA=0.22) may need to be modified to account for the percentage contribution of the photons at different depths, which is much more significant in a photodiode, which has a much wider collection angle. After determining a more accurate sensing depth of the 16PD system, we will likely need to modify the probe geometry by adding a ring of inactive dead space between the aperture and an outer detection ring to help achieve a deeper sensing depth. In addition, longer wavelengths into the 600-700 nm spectral range may also be used to achieve slightly deeper depths into breast tissue.

Assuming that the optical crosstalk can be modeled in the future, the detector spacing can be decreased to achieve better spatial resolution. Currently, the 16PD system has photodiodes with 2.5 mm diameter and center-to-center separation of 4.5 mm between the pixels. From edge to edge, there is 2 mm of inactive area between pixels in which cancer cells may exist. It would be desirable to improve spatial resolution and be able to quantify the tissue morphology under these dead spaces as well. Because deeper sensing depths are achieved by increasing source-detector separation, the spatial resolution can only be improved up to a certain point until the sensing depth becomes too shallow to be useful for tumor margin assessment. Thus, an

optimization between sensing depth and resolution can be explored. If the light delivery strategy in future iterations of system develop is such that different detector apertures are not illuminated simultaneously and crosstalk can be avoided, multiple source-detector separations at varying distances can be used. A system that has a combination of fine spatial resolution at shallow depths and coarse spatial resolution at deeper depths may be useful.

7.3.3 Addition of fluorescence imaging capabilities

As mentioned previously in the introductory chapter, certain structures and molecules, such as NADH, FAD, and collagen, will fluoresce when illuminated with specific wavelengths of light. Several groups have reported on the use of fluorescence spectroscopy to obtain contrast between benign and malignant breast tissues [44, 46, 48, 50, 70]. The fluorescence signal from collagen can provide additional structural information, and the signal from NADH and FAD can offer insight about the metabolic activity of the tissue. Because the contribution of collagen scattering to the Monte Carlo extracted $<\mu_s'>$ is not currently modeled and not well known [124], the study of collagen fluorescence can provide more information that can improve the margin classification algorithm. In addition to endogenous fluorophores in tissue, contrast agents may also be applied on *ex vivo* tissue for breast margin assessment. For instance, our group studied metabolism in breast cancer cell lines using the fluorescent contrast agent, 2-[N-(7-nitrobenz-2-oxa-1,3-diazol-4-yl)amino]-2-deoxy-D-glucose (2-NBDG) [125]. An *ex*

vivo breast tissue study has also shown an increase in fluorescence signal in malignancies after applying 2-NBDG [126]. Recent advances within nanobiotechnology and sensing also opens up a realm of new possibilities of contrast agents that can target malignancies for breast tumor margin assessment.

To add fluorescence spectroscopy capability to the photodiode-based systems, fluorescence filters can be added to the individual photodiodes. Because the excitation and emission peak wavelengths for collagen and NADH are approximately 350/410 nm and 350/450 nm, respectively, these fluorophores likely will not be useful due to the shallow sensing depths at these wavelengths. For 2-NBDG with excitation at 490 nm and emission at 540 nm, however, an addition layer of narrow band filter centered at 540 nm can be added to the photodiodes to reject all other wavelengths of light from being detected. An array with interleaving reflectance and fluorescence photodiodes can be fabricated so that the system will have both capabilities and potentially provide additional contrast in breast tissue imaging.

7.3.4 Non-contact quantitative imaging

Because we have had the luxury of collaborating with outstanding Duke surgeons and pathologists who are dedicated to clinical research and the development of intra-operative tools, we have had more freedom to handle the lumpectomy specimens and experiment with the tissue-device interface than other research groups in the field. Not all clinicians will adopt an intra-operative tool that comes in contact with

the lumpectomy specimen between excision and histopathology examination because specimen orientation is very important if re-excision is necessary—so important that some surgeons will personally carry the specimen to the pathology lab so that no mistakes can be made for orientation. A non-contact quantitative imaging device would be extremely desirable in this application and could speed up clinical translation.

The 49CH and 16PD systems are all based on contact imaging as sensing depth is easily defined by using existing Monte Carlo light propagation models. Without the probe contacting the tissue surface, a new modified model must be used to not only define the sensing depths but also to ultimately extract quantitative information from the tissue. Multi-layers of tissue have been previously modeled using Monte Carlo for applications in cervical, esophageal, and skin cancer diagnostics. Similarly, the space between the probe and the tissue surface can be modeled as a "layer" of zero absorption and zero scattering medium. The most challenging aspect of modeling non-contact spectral imaging using our current system is the specular reflection from the tissue surface. The number of specular reflectance photons collected by the photodiodes will dominate the number of diffuse reflectance photons that have traveled into the tissue. A couple of solutions can be explored to reject the specular reflection. First, polarizers can be used for the source and the detector so that only the diffusely reflected photons are detected. Secondly, a structured illumination method can be explored to achieve non-contact imaging with the photodiode arrays. By projecting patterns of light with

varying spatial frequencies on a sample, quantitative images of the tissue can be reconstructed. The detectors would likely need to be coupled with the development of new lock in amplifier circuits to differentiate between the signals with varying frequencies. If quantitative non-contact imaging can be realized, it also has potential to achieve higher resolution than standard diffuse reflectance measurements.

References

1. D. M. Parkin, F. Bray, J. Ferlay, and P. Pisani, "Global Cancer Statistics, 2002," CA: A Cancer Journal for Clinicians **55**, 74-108 (2005).

2. "SUROS News Release. New Method for Breast Cancer Diagnosis," (2003).

3. M. C. Lee, K. Rogers, K. Griffith, K. A. Diehl, T. M. Breslin, V. M. Cimmino, A. E. Chang, L. A. Newman, and M. S. Sabel, "Determinants of breast conservation rates: reasons for mastectomy at a comprehensive cancer center," Breast J **15**, 34-40 (2009).

4. M. Morrow, R. Jagsi, A. K. Alderman, J. J. Griggs, S. T. Hawley, A. S. Hamilton, J. J. Graff, and S. J. Katz, "Surgeon recommendations and receipt of mastectomy for treatment of breast cancer," JAMA **302**, 1551-1556 (2009).

5. C. Kunos, L. Latson, B. Overmoyer, P. Silverman, R. Shenk, T. Kinsella, and J. Lyons, "Breast conservation surgery achieving>or=2 mm tumor-free margins results in decreased local-regional recurrence rates," The breast journal **12**, 28-36 (2006).

6. P. H. Elkhuizen, M. J. van de Vijver, J. Hermans, H. M. Zonderland, C. J. van de Velde, and J. W. Leer, "Local recurrence after breast-conserving therapy for invasive breast cancer: high incidence in young patients and association with poor survival," Int J Radiat Oncol Biol Phys **40**, 859-867 (1998).

7. M. Clarke, R. Collins, S. Darby, C. Davies, P. Elphinstone, E. Evans, J. Godwin, R. Gray, C. Hicks, S. James, E. MacKinnon, P. McGale, T. McHugh, R. Peto, C. Taylor, and Y. Wang, "Effects of radiotherapy and of differences in the extent of surgery for early breast cancer on local recurrence and 15-year survival: an overview of the randomised trials," Lancet **366**, 2087-2106 (2005).

8. P. I. Tartter, J. Kaplan, I. Bleiweiss, C. Gajdos, A. Kong, S. Ahmed, and D. Zapetti, "Lumpectomy margins, reexcision, and local recurrence of breast cancer," Am J Surg **179**, 81-85 (2000).

9. G. C. Balch, S. K. Mithani, J. F. Simpson, and M. C. Kelley, "Accuracy of intraoperative gross examination of surgical margin status in women undergoing partial mastectomy for breast malignancy," Am Surg **71**, 22-27; discussion 27-28 (2005).

10. M. F. Dillon, E. W. Mc Dermott, A. O'Doherty, C. M. Quinn, A. D. Hill, and N. O'Higgins, "Factors affecting successful breast conservation for ductal carcinoma in situ," Ann Surg Oncol **14**, 1618-1628 (2007).

11. F. J. Fleming, A. D. Hill, E. W. Mc Dermott, A. O'Doherty, N. J. O'Higgins, and C. M. Quinn, "Intraoperative margin assessment and re-excision rate in breast conserving surgery," Eur J Surg Oncol **30**, 233-237 (2004).

12. T. L. Huston, R. Pigalarga, M. P. Osborne, and E. Tousimis, "The influence of additional surgical margins on the total specimen volume excised and the reoperative rate after breast-conserving surgery," Am J Surg **192**, 509-512 (2006).

13. L. Jacobs, "Positive margins: the challenge continues for breast surgeons," Ann Surg Oncol **15**, 1271-1272 (2008).

14. C. Kotwall, M. Ranson, A. Stiles, and M. S. Hamann, "Relationship between initial margin status for invasive breast cancer and residual carcinoma after re-excision," The American surgeon **73**, 337-343 (2007).

15. J. E. Mendez, W. W. Lamorte, A. de Las Morenas, S. Cerda, R. Pistey, T. King, M. Kavanah, E. Hirsch, and M. D. Stone, "Influence of breast cancer margin assessment method on the rates of positive margins and residual carcinoma," Am J Surg **192**, 538-540 (2006).

16. T. S. Menes, P. I. Tartter, H. Mizrachi, S. R. Smith, and A. Estabrook, "Touch preparation or frozen section for intraoperative detection of sentinel lymph node metastases from breast cancer," Ann Surg Oncol **10**, 1166-1170 (2003).

17. M. C. Smitt, K. W. Nowels, M. J. Zdeblick, S. Jeffrey, R. W. Carlson, F. E. Stockdale, and D. R. Goffinet, "The importance of the lumpectomy surgical margin status in long-term results of breast conservation," Cancer **76**, 259-267 (1995).

18. J. F. Waljee, E. S. Hu, L. A. Newman, and A. K. Alderman, "Predictors of re-excision among women undergoing breast-conserving surgery for cancer," Ann Surg Oncol **15**, 1297-1303 (2008).

19. A. J. Creager, J. A. Shaw, P. R. Young, and K. R. Geisinger, "Intraoperative evaluation of lumpectomy margins by imprint cytology with histologic

correlation: a community hospital experience," Arch Pathol Lab Med **126**, 846-848 (2002).

20. A. Chagpar, T. Yen, A. Sahin, K. K. Hunt, G. J. Whitman, F. C. Ames, M. I. Ross, F. Meric-Bernstam, G. V. Babiera, S. E. Singletary, and H. M. Kuerer, "Intraoperative margin assessment reduces reexcision rates in patients with ductal carcinoma in situ treated with breast-conserving surgery," Am J Surg **186**, 371-377 (2003).

21. C. E. Cox, N. N. Ku, D. S. Reintgen, H. M. Greenberg, S. V. Nicosia, and S. Wangensteen, "Touch Preparation Cytology of Breast Lumpectomy Margins with Histologic Correlation," Archives of Surgery **126**, 490-493 (1991).

22. S. E. Singletary, "Surgical margins in patients with early-stage breast cancer treated with breast conservation therapy," American Journal of Surgery **184**, 383-393 (2002).

23. A. O. Saarela, T. K. Paloneva, T. J. Rissanen, and H. O. Kiviniemi, "Determinants of positive histologic margins and residual tumor after lumpectomy for early breast cancer: a prospective study with special reference to touch preparation cytology," J Surg Oncol **66**, 248-253 (1997).

24. E. K. Valdes, S. K. Boolbol, J. M. Cohen, and S. M. Feldman, "Intra-operative touch preparation cytology; does it have a role in re-excision lumpectomy?," Ann Surg Oncol **14**, 1045-1050 (2007).

25. V. S. Klimberg, K. C. Westbrook, and S. Korourian, "Use of touch preps for diagnosis and evaluation of surgical margins in breast cancer," Ann Surg Oncol **5**, 220-226 (1998).

26. A. T. Johnson, R. Henry-Tillman, and V. S. Klimberg, "Breast conserving surgery: optimizing local control in the breast with the assessment of margins," Breast Dis **12**, 35-41 (2001).

27. J. C. Cendan, D. Coco, and E. M. Copeland, 3rd, "Accuracy of intraoperative frozen-section analysis of breast cancer lumpectomy-bed margins," J Am Coll Surg **201**, 194-198 (2005).

28. T. P. Olson, J. Harter, A. Munoz, D. M. Mahvi, and T. Breslin, "Frozen section analysis for intraoperative margin assessment during breast-conserving surgery

results in low rates of re-excision and local recurrence," Ann Surg Oncol **14**, 2953-2960 (2007).

29. E. R. Sauter, J. P. Hoffman, F. D. Ottery, M. J. Kowalyshyn, S. Litwin, and B. L. Eisenberg, "Is frozen section analysis of reexcision lumpectomy margins worthwhile? Margin analysis in breast reexcisions," Cancer **73**, 2607-2612 (1994).

30. S. Weber, F. K. Storm, J. Stitt, and D. M. Mahvi, "The role of frozen section analysis of margins during breast conservation surgery," Cancer J Sci Am **3**, 273-277 (1997).

31. M. Noguchi, M. Minami, M. Earashi, T. Taniya, I. I. Miyazaki, Y. Mizukami, A. Nonomura, H. Nishijima, T. Takanaka, H. Kawashima, Y. Saito, C. Takashima, S. Nakamura, T. Michigishi, and K. Yokoyama, "Pathologic Assessment of Surgical Margins on Frozen and Permanent Sections in Breast Conserving Surgery," Breast Cancer **2**, 27-33 (1995).

32. R. G. Pleijhuis, M. Graafland, J. de Vries, J. Bart, J. S. de Jong, and G. M. van Dam, "Obtaining adequate surgical margins in breast-conserving therapy for patients with early-stage breast cancer: current modalities and future directions," Ann Surg Oncol **16**, 2717-2730 (2009).

33. N. Cabioglu, K. K. Hunt, A. A. Sahin, H. M. Kuerer, G. V. Babiera, S. E. Singletary, G. J. Whitman, M. I. Ross, F. C. Ames, B. W. Feig, T. A. Buchholz, and F. Meric-Bernstam, "Role for intraoperative margin assessment in patients undergoing breast-conserving surgery," Ann Surg Oncol **14**, 1458-1471 (2007).

34. I. K. Komenaka, R. Torabi, G. Nair, L. Jayaram, C. H. Hsu, M. E. Bouton, H. Dave, and D. Hobohm, "Intraoperative touch imprint and frozen section analysis of sentinel lymph nodes after neoadjuvant chemotherapy for breast cancer," Ann Surg **251**, 319-322 (2010).

35. K. Fukamachi, T. Ishida, S. Usami, M. Takeda, M. Watanabe, H. Sasano, and N. Ohuchi, "Total-circumference intraoperative frozen section analysis reduces margin-positive rate in breast-conservation surgery," Jpn J Clin Oncol **40**, 513-520 (2010).

36. C. E. Cox, N. N. Ku, D. S. Reintgen, H. M. Greenberg, S. V. Nicosia, and S. Wangensteen, "Touch preparation cytology of breast lumpectomy margins with histologic correlation," Arch Surg **126**, 490-493 (1991).

37. T. L. Huston, R. Pigalarga, M. P. Osborne, and E. Tousimis, "The influence of additional surgical margins on the total specimen volume excised and the reoperative rate after breast-conserving surgery," American Journal of Surgery **192**, 509-512 (2006).

38. J. E. Mendez, W. W. Lamorte, A. de las Morenas, S. Cerda, R. Pistey, T. King, M. Kavanah, E. Hirsch, and M. D. Stone, "Influence of breast cancer margin assessment method on the rates of positive margins and residual carcinoma," American Journal of Surgery **192**, 538-540 (2006).

39. M. F. Dillon, E. W. Mc Dermott, A. O'Doherty, C. M. Quinn, A. D. Hill, and N. O'Higgins, "Factors affecting successful breast conservation for ductal carcinoma in situ," Annals of Surgical Oncology **14**, 1618-1628 (2007).

40. T. P. Menes TS, Bleiweiss P, et al. , "Consequences of Multiple Re-excisions to Obtain Clear Lumpectomy Margins in Breast Cancer Patients," Annual Surgical Oncology **12**, 864-865 (2005).

41. E. D. Kurniawan, M. H. Wong, I. Windle, A. Rose, A. Mou, M. Buchanan, J. P. Collins, J. A. Miller, R. L. Gruen, and G. B. Mann, "Predictors of surgical margin status in breast-conserving surgery within a breast screening program," Ann Surg Oncol **15**, 2542-2549 (2008).

42. T. M. Allweis, Z. Kaufman, S. Lelcuk, I. Pappo, T. Karni, S. Schneebaum, R. Spector, A. Schindel, D. Hershko, M. Zilberman, J. Sayfan, Y. Berlin, A. Hadary, O. Olsha, H. Paran, M. Gutman, and M. Carmon, "A prospective, randomized, controlled, multicenter study of a real-time, intraoperative probe for positive margin detection in breast-conserving surgery," Am J Surg **196**, 483-489 (2008).

43. T. Karni, I. Pappo, J. Sandbank, O. Lavon, V. Kent, R. Spector, S. Morgenstern, and S. Lelcuk, "A device for real-time, intraoperative margin assessment in breast-conservation surgery," Am J Surg **194**, 467-473 (2007).

44. T. M. Breslin, F. Xu, G. M. Palmer, C. Zhu, K. W. Gilchrist, and N. Ramanujam, "Autofluorescence and diffuse reflectance properties of malignant and benign breast tissues," Ann Surg Oncol **11**, 65-70 (2004).

45. J. Brown, L. G. Wilke, J. Geradts, S. A. Kennedy, G. M. Palmer, and N. Ramanujam, "Quantitative optical spectroscopy: a robust tool for direct

measurement of breast cancer vascular oxygenation and total hemoglobin content in vivo," Cancer research **69**, 2919 (2009).

46. M. D. Keller, S. K. Majumder, M. C. Kelley, I. M. Meszoely, F. I. Boulos, G. M. Olivares, and A. Mahadevan-Jansen, "Autofluorescence and diffuse reflectance spectroscopy and spectral imaging for breast surgical margin analysis," Lasers in Surgery and Medicine **42**, 15-23 (2010).

47. S. Kennedy, J. Geradts, T. Bydlon, J. Q. Brown, J. Gallagher, M. Junker, W. Barry, N. Ramanujam, and L. Wilke, "Optical breast cancer margin assessment: an observational study of the effects of tissue heterogeneity on optical contrast," Breast Cancer Research **12**, R91 (2010).

48. G. M. Palmer, C. Zhu, T. M. Breslin, F. Xu, K. W. Gilchrist, and N. Ramanujam, "Comparison of multiexcitation fluorescence and diffuse reflectance spectroscopy for the diagnosis of breast cancer (March 2003)," IEEE Trans Biomed Eng **50**, 1233-1242 (2003).

49. G. M. Palmer, C. Zhu, T. M. Breslin, F. Xu, K. W. Gilchrist, and N. Ramanujam, "Monte Carlo-based inverse model for calculating tissue optical properties. Part II: Application to breast cancer diagnosis," Applied optics **45**, 1072-1078 (2006).

50. Z. Volynskaya, A. S. Haka, K. L. Bechtel, M. Fitzmaurice, R. Shenk, N. Wang, J. Nazemi, R. R. Dasari, and M. S. Feld, "Diagnosing breast cancer using diffuse reflectance spectroscopy and intrinsic fluorescence spectroscopy," Journal of Biomedical Optics **13** (2008).

51. C. Zhu, G. M. Palmer, T. M. Breslin, J. Harter, and N. Ramanujam, "Diagnosis of breast cancer using diffuse reflectance spectroscopy: Comparison of a Monte Carlo versus partial least squares analysis based feature extraction technique," Lasers Surg Med **38**, 714-724 (2006).

52. C. Zhu, G. M. Palmer, T. M. Breslin, F. Xu, and N. Ramanujam, "Use of a multiseparation fiber optic probe for the optical diagnosis of breast cancer," J Biomed Opt **10**, 024032 (2005).

53. B. Brooksby, B. W. Pogue, S. D. Jiang, H. Dehghani, S. Srinivasan, C. Kogel, T. D. Tosteson, J. Weaver, S. P. Poplack, and K. D. Paulsen, "Imaging breast adipose and fibroglandular tissue molecular signatures by using hybrid MRI-guided near-infrared spectral tomography," P Natl Acad Sci USA **103**, 8828-8833 (2006).

54. B. W. Pogue, S. P. Poplack, T. O. McBride, W. A. Wells, K. S. Osterman, U. L. Osterberg, and K. D. Paulsen, "Quantitative hemoglobin tomography with diffuse near-infrared spectroscopy: pilot results in the breast," Radiology **218**, 261-266 (2001).

55. S. Srinivasan, B. W. Pogue, S. D. Jiang, H. Dehghani, C. Kogel, S. Soho, J. J. Gibson, T. D. Tosteson, S. P. Poplack, and K. D. Paulsen, "Interpreting hemoglobin and water concentration, oxygen saturation, and scattering measured in vivo by near-infrared breast tomography," P Natl Acad Sci USA **100**, 12349-12354 (2003).

56. B. J. Tromberg, A. Cerussi, N. Shah, M. Compton, A. Durkin, D. Hsiang, J. Butler, and R. Mehta, "Imaging in breast cancer: diffuse optics in breast cancer: detecting tumors in pre-menopausal women and monitoring neoadjuvant chemotherapy," Breast Cancer Res **7**, 279-285 (2005).

57. B. J. Tromberg, N. Shah, R. Lanning, A. Cerussi, J. Espinoza, T. Pham, L. Svaasand, and J. Butler, "Non-invasive in vivo characterization of breast tumors using photon migration spectroscopy," Neoplasia (New York, N.Y **2**, 26-40 (2000).

58. M. D. Keller, S. K. Majumder, M. C. Kelley, I. M. Meszoely, F. I. Boulos, G. M. Olivares, and A. Mahadevan-Jansen, "Autofluorescence and diffuse reflectance spectroscopy and spectral imaging for breast surgical margin analysis," Lasers Surg Med **42**, 15-23 (2010).

59. C. Zhu, T. M. Breslin, J. Harter, and N. Ramanujam, "Model based and empirical spectral analysis for the diagnosis of breast cancer," Opt Express **16**, 14961-14978 (2008).

60. S. G. Demos, A. J. Vogel, and A. H. Gandjbakhche, "Advances in optical spectroscopy and imaging of breast lesions," J Mammary Gland Biol Neoplasia **11**, 165-181 (2006).

61. A. S. Haka, Z. Volynskaya, J. A. Gardecki, J. Nazemi, R. Shenk, N. Wang, R. R. Dasari, M. Fitzmaurice, and M. S. Feld, "Diagnosing breast cancer using Raman spectroscopy: prospective analysis," J Biomed Opt **14**, 054023 (2009).

62. A. S. Haka, Z. Volynskaya, J. A. Gardecki, J. Nazemi, J. Lyons, D. Hicks, M. Fitzmaurice, R. R. Dasari, J. P. Crowe, and M. S. Feld, "In vivo margin assessment during partial mastectomy breast surgery using raman spectroscopy," Cancer Res **66**, 3317-3322 (2006).

63. A. S. Haka, K. E. Shafer-Peltier, M. Fitzmaurice, J. Crowe, R. R. Dasari, and M. S. Feld, "Diagnosing breast cancer by using Raman spectroscopy," Proceedings of the National Academy of Sciences of the United States of America **102**, 12371-12376 (2005).

64. F. T. Nguyen, A. M. Zysk, E. J. Chaney, J. G. Kotynek, U. J. Oliphant, F. J. Bellafiore, K. M. Rowland, P. A. Johnson, and S. A. Boppart, "Intraoperative evaluation of breast tumor margins with optical coherence tomography," Cancer Res **69**, 8790-8796 (2009).

65. P. L. Hsiung, D. R. Phatak, Y. Chen, A. D. Aguirre, J. G. Fujimoto, and J. L. Connolly, "Benign and malignant lesions in the human breast depicted with ultrahigh resolution and three-dimensional optical coherence tomography," Radiology **244**, 865-874 (2007).

66. I. J. Bigio, S. G. Bown, G. Briggs, C. Kelley, S. Lakhani, D. Pickard, P. M. Ripley, I. G. Rose, and C. Saunders, "Diagnosis of breast cancer using elastic-scattering spectroscopy: preliminary clinical results," Journal of Biomedical Optics **5**, 221-228 (2000).

67. M. Noguchi, M. Minami, M. Earashi, T. Taniya, I. Miyazaki, Y. Mizukami, A. Nonomura, H. Nishijima, T. Takanaka, H. Kawashima, Y. Saito, C. Takashima, S. Nakamura, T. Michigishi, and K. Yokoyama, "Pathologic assessment of surgical margins on frozen and permanent sections in breast conserving surgery," Breast Cancer **2**, 27-33 (1995).

68. R. Nachabe, D. J. Evers, B. H. Hendriks, G. W. Lucassen, M. van der Voort, E. J. Rutgers, M. J. Peeters, J. A. Van der Hage, H. S. Oldenburg, J. Wesseling, and T. J. Ruers, "Diagnosis of breast cancer using diffuse optical spectroscopy from 500 to 1600 nm: comparison of classification methods," J Biomed Opt **16**, 087010 (2011).

69. F. T. Nguyen, A. M. Zysk, E. J. Chaney, J. G. Kotynek, U. J. Oliphant, F. J. Bellafiore, K. M. Rowland, P. A. Johnson, and S. A. Boppart, "Intraoperative evaluation of breast tumor margins with optical coherence tomography," Cancer Research **69**, 8790-8796 (2009).

70. C. Zhu, Palmer GM, Breslin TM, Harter JM, Ramanujam N, "Diagnosis of Breast Cancer using Fluorescence and Diffuse Reflectance Spectroscopy: a Monte Carle Based Approach," J Biomed Opt (2007).

71. T. M. Bydlon, S. A. Kennedy, L. M. Richards, J. Brown, B. Yu, M. K. Junker, J. Gallagher, J. Geradts, L. G. Wilke, and N. Ramanujam, "Performance metrics of an optical spectral imaging system for intra-operative assessment of breast tumor margins," Optics Express **18**, 8058-8076 (2010).

72. L. G. Wilke, J. Q. Brown, T. M. Bydlon, S. A. Kennedy, L. M. Richards, M. K. Junker, J. Gallagher, W. T. Barry, J. Geradts, and N. Ramanujam, "Rapid noninvasive optical imaging of tissue composition in breast tumor margins," The American Journal of Surgery **198**, 566-574 (2009).

73. G. M. Palmer and N. Ramanujam, "Monte Carlo-based inverse model for calculating tissue optical properties. Part I: Theory and validation on synthetic phantoms," Applied optics **45**, 1062-1071 (2006).

74. I. J. Bigio, S. G. Bown, G. Briggs, C. Kelley, S. Lakhani, D. Pickard, P. M. Ripley, I. G. Rose, and C. Saunders, "Diagnosis of breast cancer using elastic-scattering spectroscopy: preliminary clinical results," J Biomed Opt **5**, 221-228 (2000).

75. A. M. Zysk and S. A. Boppart, "Computational methods for analysis of human breast tumor tissue in optical coherence tomography images," J Biomed Opt **11**, 054015 (2006).

76. I. J. Bigio and S. G. Bown, "Spectroscopic sensing of cancer and cancer therapy: current status of translational research," Cancer Biol Ther **3**, 259-267 (2004).

77. J. Lee, A. E. Cerussi, D. Saltzman, T. Waddington, B. J. Tromberg, and M. Brenner, "Hemoglobin measurement patterns during noninvasive diffuse optical spectroscopy monitoring of hypovolemic shock and fluid replacement," J Biomed Opt **12**, 024001 (2007).

78. Y. N. Mirabal, S. K. Chang, E. N. Atkinson, A. Malpica, M. Follen, and R. Richards-Kortum, "Reflectance spectroscopy for in vivo detection of cervical precancer," J Biomed Opt **7**, 587-594 (2002).

79. G. Zonios, L. T. Perelman, V. Backman, R. Manoharan, M. Fitzmaurice, J. Van Dam, and M. S. Feld, "Diffuse Reflectance Spectroscopy of Human Adenomatous Colon Polyps In Vivo," Appl. Opt. **38**, 6628-6637 (1999).

80. M. C. Skala, G. M. Palmer, K. M. Vrotsos, A. Gendron-Fitzpatrick, and N. Ramanujam, "Comparison of a physical model and principal component analysis for the diagnosis of epithelial neoplasias in vivo using diffuse reflectance spectroscopy," Opt Express **15**, 7863-7875 (2007).

81. R. Graaff, M. H. Koelink, F. F. M. de Mul, W. G. Zijlstra, A. C. M. Dassel, and J. G. Aarnoudse, "Condensed Monte Carlo simulations for the description of light transport [biological tissue]," Appl Opt **32**, 426-434 (1993).

82. J. W. Feather, D. J. Ellis, and G. Leslie, "A portable reflectometer for the rapid quantification of cutaneous haemoglobin and melanin," Phys Med Biol **33**, 711-722 (1988).

83. A. Cerussi, N. Shah, D. Hsiang, A. Durkin, J. Butler, and B. J. Tromberg, "In vivo absorption, scattering, and physiologic properties of 58 malignant breast tumors determined by broadband diffuse optical spectroscopy," Journal of Biomedical Optics **11**, 044005 (2006).

84. J. E. Bender, K. Vishwanath, L. K. Moore, J. Q. Brown, V. Chang, G. M. Palmer, and N. Ramanujam, "A robust Monte Carlo model for the extraction of biological absorption and scattering in vivo," Biomedical Engineering, IEEE Transactions on **56**, 960-968 (2009).

85. V. T. Chang, P. S. Cartwright, S. M. Bean, G. M. Palmer, R. C. Bentley, and N. Ramanujam, "Quantitative physiology of the precancerous cervix in vivo through optical spectroscopy," Neoplasia (New York, N.Y.) **11**, 325-332 (2009).

86. D. L. Farkas and D. Becker, "Applications of spectral imaging: detection and analysis of human melanoma and its precursors," Pigment Cell Res **14**, 2-8 (2001).

87. S. C. Gebhart, R. C. Thompson, and A. Mahadevan-Jansen, "Liquid-crystal tunable filter spectral imaging for brain tumor demarcation," Appl Opt **46**, 1896-1910 (2007).

88. B. J. Moeller, R. A. Richardson, and M. W. Dewhirst, "Hypoxia and radiotherapy: opportunities for improved outcomes in cancer treatment," Cancer Metastasis Rev **26**, 241-248 (2007).

89. E. J. Moon, D. M. Brizel, J. T. Chi, and M. W. Dewhirst, "The potential role of intrinsic hypoxia markers as prognostic variables in cancer," Antioxid Redox Signal **9**, 1237-1294 (2007).

90. A. A. Stratonnikov and V. B. Loschenov, "Evaluation of blood oxygen saturation in vivo from diffuse reflectance spectra," J Biomed Opt **6**, 457-467 (2001).

91. S. K. Chang, Y. N. Mirabal, E. N. Atkinson, D. Cox, A. Malpica, M. Follen, and R. Richards-Kortum, "Combined reflectance and fluorescence spectroscopy for in vivo detection of cervical pre-cancer," J Biomed Opt **10**, 024031 (2005).

92. R. Reif, O. A'Amar, and I. J. Bigio, "Analytical model of light reflectance for extraction of the optical properties in small volumes of turbid media," Appl Opt **46**, 7317-7328 (2007).

93. R. Reif, M. S. Amorosino, K. W. Calabro, O. A'Amar, S. K. Singh, and I. J. Bigio, "Analysis of changes in reflectance measurements on biological tissues subjected to different probe pressures," J Biomed Opt **13**, 010502 (2008).

94. W. C. Lin, S. A. Toms, M. Johnson, E. D. Jansen, and A. Mahadevan-Jansen, "In vivo brain tumor demarcation using optical spectroscopy," Photochem Photobiol **73**, 396-402 (2001).

95. A. Cerussi, D. Hsiang, N. Shah, R. Mehta, A. Durkin, J. Butler, and B. J. Tromberg, "Predicting response to breast cancer neoadjuvant chemotherapy using diffuse optical spectroscopy," Proc Natl Acad Sci U S A **104**, 4014-4019 (2007).

96. D. B. Jakubowski, A. E. Cerussi, F. Bevilacqua, N. Shah, D. Hsiang, J. Butler, and B. J. Tromberg, "Monitoring neoadjuvant chemotherapy in breast cancer using quantitative diffuse optical spectroscopy: a case study," J Biomed Opt **9**, 230-238 (2004).

97. N. Shah, J. Gibbs, D. Wolverton, A. Cerussi, N. Hylton, and B. J. Tromberg, "Combined diffuse optical spectroscopy and contrast-enhanced magnetic

resonance imaging for monitoring breast cancer neoadjuvant chemotherapy: a case study," J Biomed Opt **10**, 051503 (2005).

98. T. J. Pfefer, L. S. Matchette, C. L. Bennett, J. A. Gall, J. N. Wilke, A. J. Durkin, and M. N. Ediger, "Reflectance-based determination of optical properties in highly attenuating tissue," J Biomed Opt **8**, 206-215 (2003).

99. V. T. Chang, P. S. Cartwright, S. M. Bean, G. M. Palmer, R. Bentley, and N. Ramanujam, "Quantitative physiology of the precancerous cervix *in vivo* via optical spectroscopy," (to be submitted).

100. W. F. Cheong, "Appendix to chapter 8: Summary of optical properties," Optical-Thermal Response of Laser-Irradiated Tissue, 275-303 (1995).

101. S. Prahl, "Mie scattering program," Oregon Medical Laser Center (2005).

102. Q. Liu and N. Ramanujam, "Scaling method for fast Monte Carlo simulation of diffuse reflectance spectra from multilayered turbid media," J. Opt. Soc. Am. A **24**, 1011-1025 (2007).

103. J. B. Fishkin, O. Coquoz, E. R. Anderson, M. Brenner, and B. J. Tromberg "Frequency-domain photon migration measurements of normal and malignant tissue optical properties in a human subject," Appl Opt **36**, 10-20 (1997).

104. T. M. Bydlon, S. A. Kennedy, L. M. Richards, J. Q. Brown, B. Yu, M. K. Junker, J. Gallagher, J. Geradts, L. G. Wilke, and N. Ramanujam, "Performance metrics of an optical spectral imaging system for intra-operative assessment of breast tumor margins," Opt. Express **18**, 8058-8076 (2010).

105. H. L. Fu, B. Yu, J. Y. Lo, G. M. Palmer, T. F. Kuech, and N. Ramanujam, "A low-cost, portable, and quantitative spectral imaging system for application to biological tissues," Optics Express **18**, 12630-12645 (2010).

106. J. Y. Lo, B. Yu, T. F. Kuech, and N. Ramanujam, "A compact, cost-effective diffuse reflectance spectroscopic imaging system for quantitative tissue absorption and scattering," Proceedings of SPIE **7890**, 78900B (2011).

107. S. Dhar, J. Y. Lo, B. Yu, M. A. Brooke, N. Ramanujam, and N. M. Jokerst, "Custom annular photodetector arrays for breast cancer margin assessment using diffuse reflectance spectroscopy," in (IEEE, 2011), 440-443.

108. J. Y. Lo, B. Yu, H. L. Fu, J. E. Bender, G. M. Palmer, T. F. Kuech, and N. Ramanujam, "A strategy for quantitative spectral imaging of tissue absorption and scattering using light emitting diodes and photodiodes," Optics Express **17**, 1372-1384 (2009).

109. B. Yu, J. Y. Lo, T. F. Kuech, G. M. Palmer, J. E. Bender, and N. Ramanujam, "Cost-effective diffuse reflectance spectroscopy device for quantifying tissue absorption and scattering in vivo," Journal of Biomedical Optics **13**, 060505 (2008).

110. A. Mazhar, S. Dell, D. J. Cuccia, S. Gioux, A. J. Durkin, J. V. Frangioni, and B. J. Tromberg, "Wavelength optimization for rapid chromophore mapping using spatial frequency domain imaging," Journal of Biomedical Optics **15**, 061716-061719 (2010).

111. S. Umeyama and T. Yamada, "New cross-talk measure of near-infrared spectroscopy and its application to wavelength combination optimization," Journal of Biomedical Optics **14**, 034017-034018 (2009).

112. D. S. Ferreira, J. Mirkovic, R. F. Wolffenbuttel, J. H. Correia, M. S. Feld, and G. Minas, "Narrow-band pass filter array for integrated opto-electronic spectroscopy detectors to assess esophageal tissue," Biomed. Opt. Express **2**, 1703-1716 (2011).

113. J. E. Phelps, K. Vishwanath, V. T. C. Chang, and N. Ramanujam, "Rapid ratiometric determination of hemoglobin concentration using UV-VIS diffuse reflectance at isosbestic wavelengths," Opt. Express **18**, 18779-18792 (2010).

114. J. Y. Lo, S. Dhar, B. Yu, M. A. Brooke, T. F. Kuech, N. M. Jokerst, and N. Ramanujam, "Diffuse reflectance spectral imaging for breast tumor margin assessment," Proceedings of SPIE **8214**, 821407 (2012).

115. B. Yu, J. Q. Brown, M. Junker, J. Gallagher, J. Geradts, and N. Ramanujam, "A 49-channel Diffuse Reflectance Imaging System for Intraoperative Detection of Breast Tumor Margins," In preparation (2012).

116. J. Y. Lo, J. Q. Brown, S. Dhar, B. Yu, G. M. Palmer, N. M. Jokerst, and N. Ramanujam, "Wavelength optimization for quantitative spectral imaging of breast tumor margins," PLoS One (submitted 2012).

117. S. Dhar, J. Y. Lo, G. M. Palmer, M. A. Brooke, B. S. Nichols, B. Yu, N. Ramanujam, and N. M. Jokerst, "A diffuse reflectance spectral imaging system for tumor margin assessment using custom annular photodiode arrays," Biomed. Opt. Express (submitted 2012).

118. T. M. Bydlon, W. T. Barry, S. A. Kennedy, J. Q. Brown, J. E. Gallagher, L. G. Wilke, J. Geradts, and N. Ramanujam, "Advancing optical imaging for breast margin assessment: an analysis of excisional time, cautery, and Lymphazurin™ on underlying sources of contrast," PLoS One (Accepted 2012).

119. V. T.-C. Chang, D. Merisier, B. Yu, D. K. Walmer, and N. Ramanujam, "Towards a field-compatible optical Spectroscopic device for cervical cancer screening in resource-limited settings: effects of calibration and pressure," Opt. Express **19**, 17908-17924 (2011).

120. A. Nath, K. Rivoire, S. Chang, D. Cox, E. N. Atkinson, M. Follen, and R. Richards-Kortum, "Effect of probe pressure on cervical fluorescence spectroscopy measurements," Journal of Biomedical Optics **9**, 523-533 (2004).

121. L. Wang, S. L. Jacques, and L. Zheng, "MCML—Monte Carlo modeling of light transport in multi-layered tissues," Computer Methods and Programs in Biomedicine **47**, 131-146 (1995).

122. T. Li, H. Gong, and Q. Luo, "MCVM: Monte Carlo modeling of photon migration in voxelized media," Journal of Innovative Optical Health Sciences **03**, 91-102 (2010).

123. F. Hu, K. Vishwanath, J. E. Phelps, J. Lo, W. T. Lee, and N. Ramanujam, "Rapid Determination of Tissue Hemoglobin Concentration and Oxygen Saturation of Head and Neck Cancers for Global Health Applications," in OSA Technical Digest (Optical Society of America, 2012), BW3B.4.

124. J. Q. Brown, T. M. Bydlon, S. A. Kennedy, M. L. Caldwell, J. E. Gallagher, M. S. Junker, L. G. Wilke, W. T. Barry, J. Geradts, and N. Ramanujam, "Spectral Surveillance of Histologic “Landscapes” to detect Residual Disease in Breast Tumor Margins," Cancer Research (submitted 2012).

125. S. Millon, J. Ostrander, J. Brown, A. Raheja, V. Seewaldt, and N. Ramanujam, "Uptake of 2-NBDG as a method to monitor therapy response in breast cancer cell lines," Breast Cancer Research and Treatment **126**, 55-62 (2011).

126. R. J. Langsner, L. P. Middleton, J. Sun, F. Meric-Bernstam, K. K. Hunt, R. A. Drezek, and T. K. Yu, "Wide-field imaging of fluorescent deoxy-glucose in ex vivo malignant and normal breast tissue," Biomed. Opt. Express **2**, 1514-1523 (2011).

Biography

Justin Lo was born in Kaohsiung, Taiwan on February 18, 1983 and was raised in Port Lavaca, Texas. He received his B.A. with honors in Liberal Arts in the Plan II Honors Program and a B.S. with honors in Biomedical Engineering from the University of Texas at Austin in May 2006. For his graduate studies, he attended Duke University and received a Ph.D. in Biomedical Engineering in December 2012. His wife, Jessica, is also a graduate of the University of Texas, and they have two sons, Jordan and Jackson.

Publications

Peer-reviewed

1) **JY Lo**, JQ Brown, S Dhar, B Yu, GM Palmer, NM Jokerst, and N Ramanujam. "Wavelength optimization for quantitative spectroscopic imaging of breast tumor margins," PLoS One, submitted (2012).
2) S Dhar, **JY Lo**, GM Palmer, MA Brooke, BS Nichols, B Yu, N Ramanujam, NM Jokerst. "A diffuse reflectance spectral imaging system for tumor margin assessment using custom annular photodiode arrays," Biomedical Optics Express, submitted (2012)
3) F Hu, K Vishwanath, **JY Lo**, WT Lee, and N Ramanujam. "Rapid determination of oxygen saturation and vascularity for oncological applications," Manuscript under preparation.
4) HL Fu, B Yu, **JY Lo**, GM Palmer, TF Kuech, and N Ramanujam. "A low-cost, portable, and quantitative spectral imaging system for application to biological tissues," Optics Express, Vol. 18, 12630-12645 (2010).
5) **JY Lo**, B Yu, HL Fu, JE Bender, GM Palmer, TF Kuech, and N Ramanujam. "A strategy for quantitative spectral imaging of tissue absorption and scattering using light emitting diodes and photodiodes," Optics Express, Vol. 13, 1372-1384 (2009).
6) B Yu, **JY Lo**, TF Kuech, GM Palmer, JE Bender, and N Ramanujam. "A cost-effective diffuse reflectance spectroscopy device for quantifying tissue absorption and scattering *in vivo*," Journal of Biomedical Optics, Vol. 13, 060505 (2008).
7) L Zhang, AS Garden, **JY Lo**, KK Ang, A Ahamad, WH Morrison, DI Rosenthal, MS Chambers, XR Zhu, R Mohan, and L Dong. "Multiple regions-of-interest analysis of setup uncertainties for head-and-neck cancer radiotherapy," International Journal of Radiation Oncology, Biology, and Physics, Vol. 64, 1559-1569 (2006).
8) L Zhang, L Dong, KK Ang, **JY Lo**, S Tung, B Mason, P Wong, A Ahamad, WH Morrison, DI Rosenthal, MS Chambers, AS Garden. "A region-of-interest

analysis of setup uncertainties in head and neck radiotherapy, "International Journal of Radiation Oncology, Biology, and Physics, Vol. 63, S88-S89 (2005).

Patents

1) B Yu, N Ramanujam, and **JY Lo**. "A diffuse reflectance spectroscopy device for quantifying tissue absorption and scattering," International Application No. PCT/US2009/041732

Conference Proceedings

1) **JY Lo**, S Dhar, B Yu, MA Brooke, TF Kuech, NM Jokerst, and N Ramanujam. "Diffuse reflectance spectral imaging for breast tumor margin assessment," Proceedings of SPIE, Vol. 8214,821407 (2012).
2) F Hu, K Vishwanath, JE Phelps, **JY Lo**, WT Lee, and N Ramanujam. "Rapid determination of tissue hemoglobin concentration and oxygen saturation of head and neck cancers for global health applications," Biomedical Optics, OSA Technical Digest (2012)
3) **JY Lo**, B Yu, TF Kuech, and N Ramanujam. "A compact, cost-effective diffuse reflectance spectroscopic imaging system for quantitative tissue absorption and scattering," Proceedings of SPIE, Vol. 7890, 78900B (2011).
4) S Dhar, **JY Lo**, B Yu, TF Kuech, N Ramanujam, and NM Jokerst. "A custom wide-field spectral imager for breast cancer margin assessment," Proceedings of IEEE Photonics Society Annual Meeting, 798-799 (2011).
5) S Dhar, **JY Lo**, B Yu, MA Brooke, N Ramanujam, and NM Jokerst. "Custom annular photodetector arrays for breast cancer margin assessment using diffuse reflectance spectroscopy," Proceedings of IEEE Biomedical Circuits and Systems, 440-443 (2011).
6) HL Fu, B Yu, **JY Lo**, TF Kuech, and N Ramanujam. "A low cost system for quantitative spectral imaging of tissue absorption and scattering," Engineering Conference International on Advances in Optics for Biotechnology, Medicine, and Surgery XI (2009).
7) **JY Lo**, B Yu, GM Palmer, TF Kuech, and N Ramanujam. "A miniature optical device for noninvasive, fast characterization of tumor pathology," Biomedical Optics, OSA Technical Digest (CD), BTuF55 (2008).

Conference Presentations

1) "Design, validation, and implementation of a diffuse reflectance spectroscopic imaging system for tissue absorption and scattering," oral presentation at SPIE

Photonics West BiOS, Conference 8214: Advanced Biomedical and Clinical Diagnostic Systems X, January 2012, San Francisco, CA.

2) "A compact spectroscopic imaging system for quantitative tissue absorption and scattering," oral presentation at SPIE Photonics West BiOS, Conference 7890: Advanced Biomedical and Clinical Diagnostics Systems XI, January 2011, San Francisco, CA.
3) "A Miniature Optical Device for Noninvasive, Fast Characterization of Tumor Pathology," poster presentation at Optical Society of America: Biomedical Optics Topical Meeting, March 2008, St. Petersburg, FL.

Memberships and Honors

- Optical Society of America (OSA)
- International Society of Optical Engineering (SPIE)
- Phi Beta Kappa
- Tau Beta Pi
- Golden Key International Honour Society
- Newport Student Travel Grant, SPIE, 2012